REPORT DOCUMENTATION PAGE

Form Approved
OMB No. 0704-0188

PLEASE DO NOT RETURN YOUR FORM TO THE ABOVE ORGANIZATION.

1. REPORT DATE *(DD-MM-YYYY)*	2. REPORT TYPE	3. DATES COVERED *(From - To)*
30-06-2019	Final Technical Report	01-04-2017 - 31-03-2019

4. TITLE AND SUBTITLE
Enhancement of Laser Multi-Beam Differential Interferometric Sensor and Seismic Vibration Response of Targets

5a. CONTRACT NUMBER
N00014-17-1-2332

5b. GRANT NUMBER

5c. PROGRAM ELEMENT NUMBER

6. AUTHOR(S)
Vyacheslav Aranchuk

5d. PROJECT NUMBER

5e. TASK NUMBER

5f. WORK UNIT NUMBER

7. PERFORMING ORGANIZATION NAME(S) AND ADDRESS(ES)
The University of Mississippi
100 Barr Hall
P. O. Box 1848
University, MS 38677-1848

8. PERFORMING ORGANIZATION REPORT NUMBER

9. SPONSORING/MONITORING AGENCY NAME(S) AND ADDRESS(ES)
Office of Naval Research
875 N. Randolph Street Suite 1425
Arlington VA 22203-1995

10. SPONSOR/MONITOR'S ACRONYM(S)

11. SPONSOR/MONITOR'S REPORT NUMBER(S)

12. DISTRIBUTION/AVAILABILITY STATEMENT
Approved for public release; distribution is unlimited.

13. SUPPLEMENTARY NOTES

14. ABSTRACT National Center for Physical Acoustics (NCPA) at the University of Mississippi developed a Laser Multi-Beam Differential Interferometric Sensor (LMBDIS) for stand-off measurement of vibration fields. The LMBDIS has low sensitivity to the platform motion, while maintaining high interferometric sensitivity to the object vibration. The LMBDIS can be used for sensing vibration of ground from a moving vehicle for acoustic detection of buried objects. The report describes the principle of operation, optical schematics of the LMBDIS, signal processing for vibration imaging, and experiments on acoustic detection of buried objects using the LMBDIS. Field experiments on acoustic detection of buried targets using the LMBDIS mounted on a small electric vehicle have been performed at a military test site. A loudspeaker and a wheeled shaker were used for ground vibration excitation. The detection of buried objects was conducted from a moving, as well from a stationary vehicle. Additional studies of the vibration response of various buried objects and acoustic/seismic properties of three different types of grounds have also been conducted using a loudspeaker and a mechanical shaker. The coupling of energy from the different sources into ground vibrations as a function of range has been studied. The vibrational field above and adjacent to various buried objects were measured as a function of burial depth and range. The measurement results are presented and discussed in the report.

15. SUBJECT TERMS
laser vibrometer, vibration sensor, acoustic detection, shaker, seismic, buried object

16. SECURITY CLASSIFICATION OF:			17. LIMITATION OF ABSTRACT	18. NUMBER OF PAGES	19a. NAME OF RESPONSIBLE PERSON
a. REPORT	b. ABSTRACT	c. THIS PAGE			Vyacheslav Aranchuk
U				104	19b. TELEPHONE NUMBER *(Include area code)* (662) 915-5610

ENHANCEMENT OF LASER MULTI-BEAM DIFFERENTIAL INTERFEROMETRIC SENSOR AND SEISMIC VIBRATION RESPONSE OF TARGETS

FINAL REPORT

June 30, 2019

SUBMITTED TO:

OFFICE OF NAVAL RESEARCH
JOONG KIM, PhD
Program Officer, CODE 32
OCEAN BATTLESPACE AND EXPEDITIONARY ACCESS

BY:

VYACHESLAV ARANCHUK AND CRAIG HICKEY
UNIVERSITY OF MISSISSIPPI
JAMIE L. WHITTEN NATIONAL CENTER FOR PHYSICAL ACOUSTICS
UNIVERSITY OF MISSISSIPPI
P. O. BOX 1848
145 HILL DR.
UNIVERSITY, MISSISSIPPI 38677

PERIOD: 1 APRIL 2017 THROUGH 31 MARCH 2019
GRANT NUMBER: N00014-17-1-2332
TITLE OF PROJECT: ENHANCEMENT OF LASER MULTI-BEAM DIFFERENTIAL INTERFEROMETRIC SENSOR AND SEISMIC VIBRATION RESPONSE OF TARGETS
PRINCIPAL INVESTIGATORS: V. ARANCHUK AND C. HICKEY
SECURITY CLASSIFICATION: UNCLASSIFIED

Table of Contents

List of figures

1 Introduction

Acoustic detection of buried objects, such as mines, has proven itself as a technique that provides high, better than 95% probability of detection and very low, on the order of 0.03 m^{-2} false alarm rate. The method consists of exciting ground vibrations and measuring the vibration characteristics of the ground at many points with a non-contact vibration sensor, for example a laser Doppler vibrometer (LDV). The presence of a buried object can be determined by its vibration signatures, which are different from the vibration signatures of the ground[1-4].

Airborne sound created by a loudspeaker or seismic waves created by a mechanical shaker excite vibrations of the ground in the frequency range from about 50 Hz to 400 Hz. The interaction of a buried object with the elastic waves in the ground causes the object to vibrate. Mines are complex mechanical structures with moving parts, such as a pressure plate, a trigger

assembly, etc., and exhibit significantly greater resonance characteristics than natural clutter objects. Due to the mechanical resonances and the higher mechanical compliance of the mine compared to the neighboring soil, the vibration amplitude of the ground surface above a mine is higher than the vibration amplitude of the surrounding area. A non-contact vibration sensor, such as a LDV, measures the vibration of the ground at many points to create a vibration image of the ground surface. A buried mine can be detected by higher vibration amplitude of the surface area above the mine. The described technique was successfully used for detection of antitank and antipersonnel mines in field tests[1-11].

LDVs traditionally used for acoustic detection provide vibration measurements at many points of the ground with sub-nanometer sensitivity[4-11]. However, the LDVs also respond to the LDV vibration itself, which is combined with the vibration of the object. This is because the measurement is based on interference of light reflected from the object with an internal reference beam. As a result, motion of the LDV due to environmental vibration and acoustic noise can cause LDV signals to be higher than, and indistinguishable from, signals caused by object vibration. As a result, application of LDVs for acoustic detection of buried objects requires operation from a mechanically stable and acoustically isolated platform. This limits the practical application of acoustic methods for detection of buried objects.

A vibration image of the ground surface can also be obtained using whole-field non-contact vibration sensors, such as Electronic Speckle Pattern Interferometers (ESPI)[13]. Pulsed ESPI provides vibration measurement at many (more than a million, depending on the number of pixels of the CCD or CMOS array photodetector) points on the surface simultaneously. The spatial displacement distribution of a vibrating object can be obtained for a time on the order of a half of a period of vibration. However, ESPI has a limited dynamic range of about 40 nm to 12 μm, and displacement resolution of about 10-20 nm[14], which is considerably lower than the resolution of a LDV. As well as LDVs, the ESPI is sensitive to ambient vibration and acoustic noise, since it also employs a reference beam, and requires operation from a mechanically stable platform.

Digital shearography is another interferometric whole-field non-contact technique that can be used as a vibration sensor for acoustic detection of buried objects[15]. Because of the lack of the reference beam, it has low sensitivity to platform motion along the direction of the laser beam[16-18]. The shearography sensor provides a single snap shot of an object deformation between two moments of time, normally synchronized with peaks and valleys of the object vibration. Shearography also provides high spatial resolution of better than a millimeter for a one square meter surface area measurements. However, alongside the advantages of high spatial resolution and low sensitivity to platform motion, shearography has some issues that could limit its application for acoustic detection. First, only single frequency vibrations can be measured at a time. To analyze a frequency response of a buried object, additional shearograms must be obtained at each selected frequency, increasing the detection time. Another major issue of shearography is sensitivity. Shearography employing phase shifting interferometry has resolution of approximately 10-20nm, which is more than two orders of magnitude lower than the resolution of LDVs. Visual estimation of a fringe pattern shearogram gives even lower resolution on the order of 100 nm. These two downsides of shearography could limit its application for acoustic detection.

Summarizing the performance of current laser vibration sensors for acoustic detection, one can conclude that the high performance of acoustic methods for detection of buried objects is limited by: high sensitivity of LDVs and ESPI to ambient vibration, and low sensitivity of

shearography and ESPI to object vibration and long measurement time required to obtain a frequency response of the object.

In order to overcome drawbacks of LDV, ESPI and shearography, The University of Mississippi, National Center for Physical Acoustics (NCPA) under grant #N000141310868 from Office of Naval Research (ONR) has developed a novel interferometric sensor, the Laser Multi-Beam Differential Interferometric Sensor (LMBDIS)[19]. The sensor provides measurement of vibration fields of objects with high sensitivity, while having low sensitivity to the whole body motion of the object, or sensor itself. A brassboard of the sensor, that can be mounted on a vehicle and used in the field, has been developed and built by NCPA under contract with NSWC PCD #N00178-04-D-4143-HR20 (TI008). The brassboard LMBDIS mounted on a small electric vehicle has been used in field experiments for acoustic detection of buried objects in conjunction with a wheeled shaker under grant # N0001401512660[20].

This report presents results on recent improvements of the LMBDIS, laboratory and field investigations of LMBDIS performance for acoustic detection of buried objects, studies of the vibration response of various buried objects, and acoustic/seismic properties of different types of grounds using a loudspeaker and a mechanical shaker.

2 Principle of operation of LMBDIS

The principle of operation of the LMBDIS is based on the interference of light reflected from neighboring points on the object surface illuminated with a linear array of laser beams, as illustrated by Figure 1. A linear array of 30 laser beams (only 6 beams are shown for clarity), in which adjacent beams have different optical frequencies, is created by a transmitter and illuminates an object. Specifically, each beam of frequency F_1 is positioned on the object surface exactly between two beams of frequency F_2. So, the optical frequency of even number beams is different from the optical frequency of odd number beams. A receiver lens and an interferometer create two images of the laser spots on the object on a photodetector array (PDA) sheared relative to one another in the direction of the array of points. The two images are sheared relative to each other by the odd number of intervals between neighboring laser spots in the image plane. For example, two images could be sheared relative to each other on the PDA by one or three intervals between neighboring laser spots in the image plane. As a result, the light from each pair of corresponding laser spots on the object surface, which have different frequencies (i.e., differing by F_2 - F_1), are mixed together to interfere on the PDA, producing heterodyne frequency modulated (FM) signals with the carrier frequency $F_H = F_2 - F_1$ on the photodetector array outputs. Referring to Figure 1, for the case of one interval shear between the two images, image 1 1-6 of laser spots on the object surface is overlapped on photosensitive elements of the PDA with the sheared image 2 1'-6'. In more detail, image 1 of spot 1 is overlapped with image 2' of spot 2 on element 1, image 2 of spot 2 is overlapped with image 3' of spot 3 on element 2, and so on. Overlapped images of laser spots interfere, producing heterodyne FM signals with F_H carrier frequency on PDA outputs. Each point of a vibrating object vibrates with a different velocity (except for the case of a rigid body motion which is of little interest). Velocities of the object surface V_i and V_j at points of incidence of corresponding laser beams i and j (for example beams 1 and 2) cause shifts F_{Di} and F_{Dj} of the optical frequency of the light reflected backward from the object due to the Doppler effect, by:

$$F_{Di} = \frac{2V_i}{\lambda}\cos\alpha_i \; ; \tag{1}$$

$$F_{Dj} = \frac{2V_j}{\lambda}\cos\alpha_j \tag{2}$$

where λ is the optical wavelength, and $\alpha_{i,j}$ is the intersection angle between the laser beam and object velocity direction. Interference of lights from two spots i and j on a photodetector produces a heterodyne signal $i_{ij}(t)$ on the photodetector output

$$i_{ij}(t) = J\cos\left[2\pi\left(F_H + \Delta F_{Dij}(t)\right) + \Delta\varphi\right] \tag{3}$$

where $J = 2kP_i^{\frac{1}{2}}P_j^{\frac{1}{2}}$ is the amplitude of the heterodyne signal, k is the sensitivity of the photodetector, $P_i$and P_j are the optical powers of the light on the photodetector reflected from two spots i and j on the object respectively, $F_H = F_2 - F_1$ is the carrier frequency, $\Delta F_{Dij}(t) = F_{Di}(t) - F_{Dj}(t) = \frac{2}{\lambda}\left(V_i\cos\alpha_i - V_j\cos\alpha_j\right)$ is the difference in Doppler shifts of light reflected from spots i and j , and $\Delta\varphi$ is the phase difference of light on the photodetector reflected from two spots i and j. Equation (3) shows that the detected signal is a FM signal with carrier frequency F_H. Using an FM-demodulation technique, the relative vibration velocity $V_i - V_j$ between spots i and j can be extracted, provided that angles α_i and α_j are known from the geometry of the sensor. Motion of the sensor with the speed V_0 results in the following Doppler shift between lights reflected from two spots i and j

$$\Delta F_{Dij}(t) = \frac{2}{\lambda}V_0\left(\cos\alpha_i - \cos\alpha_j\right) \tag{4}$$

For small angles (less than 1°) between neighboring beams the Doppler shift $\Delta F_{Dij}(t)$ caused by the sensor motion will be significantly lower than the Doppler shift in a LDV for the same speed of motion. For example, the maximum Doppler shift between neighboring beams occurs for edge beams, such as beams 1 and 2. For beams 1 and 2 angles in the LMBDIS design, as described below, α_1= 2.85° and α_2 = 2.65°, $\Delta F_{D12}(t) = -1.67\cdot 10^{-4}\,\frac{2}{\lambda}V_0$, which is $1.67\cdot10^{-4}$ of the Doppler shift in a LDV signal. At the same time the sensor has high interferometric sensitivity to relative vibration between corresponding points on the object. So, the LMBDIS configuration provides high sensitivity to the relative vibration between illuminated points on the object surface and low sensitivity to the motion of the sensor itself. Low Doppler shift caused by the sensor motion allows the sensor operation from a moving vehicle without employing Doppler tracking and increasing the processing bandwidth. Frequency demodulation of the PDA signals reveals the relative velocity and displacement of the object surface between corresponding laser spots. LMBDIS signals can be digitally FM-demodulated by using a multichannel analog-to-digital converter (ADC) and a processor, as shown in Figure 1. The demodulated signals can be used to generate a vibration velocity or displacement image or profile of the object. Relative velocities and displacements between corresponding illuminated points on the object surface will provide the deformation gradient of the surface along the line of the beams, if the interval between laser spots on the object is considerably smaller than the size

of the deformation profile. The beams can be scanned in the transverse direction to provide the 2D deformation gradient of the surface across the scanned area.

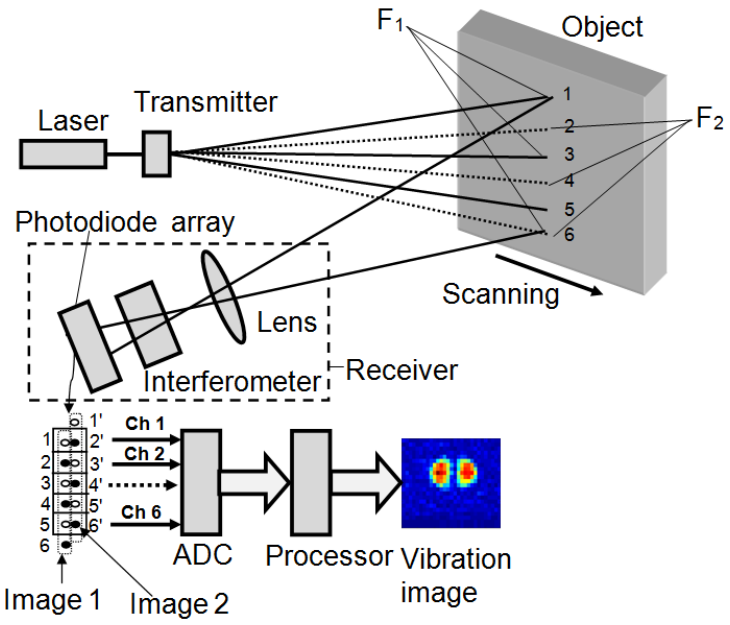

Figure 1. Principle of operation of LMBDIS.

The path length difference of the interference beams is close to zero. Because of this, the LMBDIS has lower sensitivity to laser phase noise than traditional LDVs, and less stringent requirements on the coherence length of the laser.

3 Optical layout

The optical schematic of the LMBDIS[21] is shown in Figure 2. The sensor uses a CW laser Verdi G5 SLM (Coherent, Inc.) which delivers up to 5 watts of optical power at 532 nm wavelength. A laser beam reflected by folding mirror M1 is divided by a non-polarizing beam splitting cube NPBS1into two beams which are incident onto acousto-optic modulators AOM1 and AOM2. The frequency of each beam is then shifted by a different amount of F1 = 110 MHz and F2 = 110.01 MHz respectively by using acousto-optical modulators AOM1 and AOM2. The laser beam incident on the AOMs is *s*-polarized. The AOMs flip the polarization by 90 degrees, making the output frequency shifted beams *p*-polarized. Frequency shifted beams are then combined together on the focusable beam expander BE at an angle β to one another, using mirrors M3 and M4. Frequency shifted beams pass through the beam expander, and are incident onto a diffractive optical element beam splitter DOE. The beam expander increases the diameter of the beams by M times and reduces the angle between the beams by M times, where M is the expansion ratio/magnification of the beam expander. The angle β between the beams incident on

BE is related to the inter-beam angle Θ (the angle between neighboring beams at the DOE output) of the DOE and the magnification M of the beam expander through the following expression: $\beta = \Theta \cdot M/2$. Prisms P1 - P3 positioned after the AOMs are used for accurate angular adjustment of the beams. The DOE splits frequency shifted beams into two identical arrays of beams. The DOE used in the design splits each incident beam into a line of 15 beams with inter-beam angle $\Theta = 0.407°$, and full pattern angle 5.7°. The angle β between the two frequency shifted beams incident on the BE is adjusted such that the two arrays of beams are sheared on the object surface relative to each other by a half of an inter-beam spacing of the array, producing a combined 30 beam linear array, in which adjacent beams have different optical frequencies. Specifically, the frequency of the neighboring beams in the combined beam array are 110 MHz and 110.01 MHz respectively, so each of the 110.0 MHz beams is positioned on the object exactly between two 110.01 MHz beams. Accordingly, in the linear array, there exists a 10 kHz frequency shift between neighboring beams. The inter-beam angle of the combined 30 beam array is 0.2035°, and full pattern angle is 5.9°. The diameter of the beams on the object could be adjusted by adjusting focus of the beam expander BE. A polarizing beam splitter PBS positioned after DOE transmits *p*-polarized light towards the object. A quarter-wave plate QWP converts the *p*-polarized light into circularly polarized light incident upon the object surface. The mirror M5 and the scanning mirror direct the laser beams to the object surface. The scanning mirror is used to scan the array of beams across the object in order to create a vibration image of object surface, and also for positioning the array of beams on the particular place on the object. The light reflected back by the object surface passes through the scanning mirror, mirror M5, and the quarter-wave plate QWP, changing the light polarization from circular to *s*-polarized light. The *s*-polarized light is reflected by the polarizing beam splitter PBS and enters a Michelson interferometer formed by non-polarizing beam splitting cube NPBS2, mirrors M6 and M7, and wedge prisms P4, P5. Prisms P4 and P5 positioned in the interferometer arms are used for accurate angular adjustment of the interferometer. Lens L1 creates an image of laser spots on the object surface on a photodetector array PDA. The Michelson interferometer produces 10 kHz frequency heterodyne signals at the interferometer output by laterally shearing two arrays of spots in the image plane by using angular adjustments of mirrors M6 and M7, and prisms P4 and P5. As a result, the light from each pair of corresponding laser spots on the object, which have different frequencies (i.e., differing by 10 kHz), are mixed together to interfere on the PDA, producing heterodyne signals with 10 kHz carrier on the PDA outputs. A 35 element Si pin photodiode array has been used in the design. The photodiode outputs were amplified by 35 transimpedance amplifiers. The amplified photodetector signals are digitized using a multichannel A/D converter DAQ, and recorded into computer memory. A National Instruments multichannel dynamic signal acquisition device based on two high-channel-count dynamic signal analyzers NI PXIe-4497, and a controller NI PXIe-8115 was used for data acquisition. The device is capable of recording 32 analog signals simultaneously, with the maximum sampling rate 204kS/s per channel and with resolution of 24 bits. Heterodyne 10 kHz carrier signals were recorded using customized National Instruments LabVIEW code.

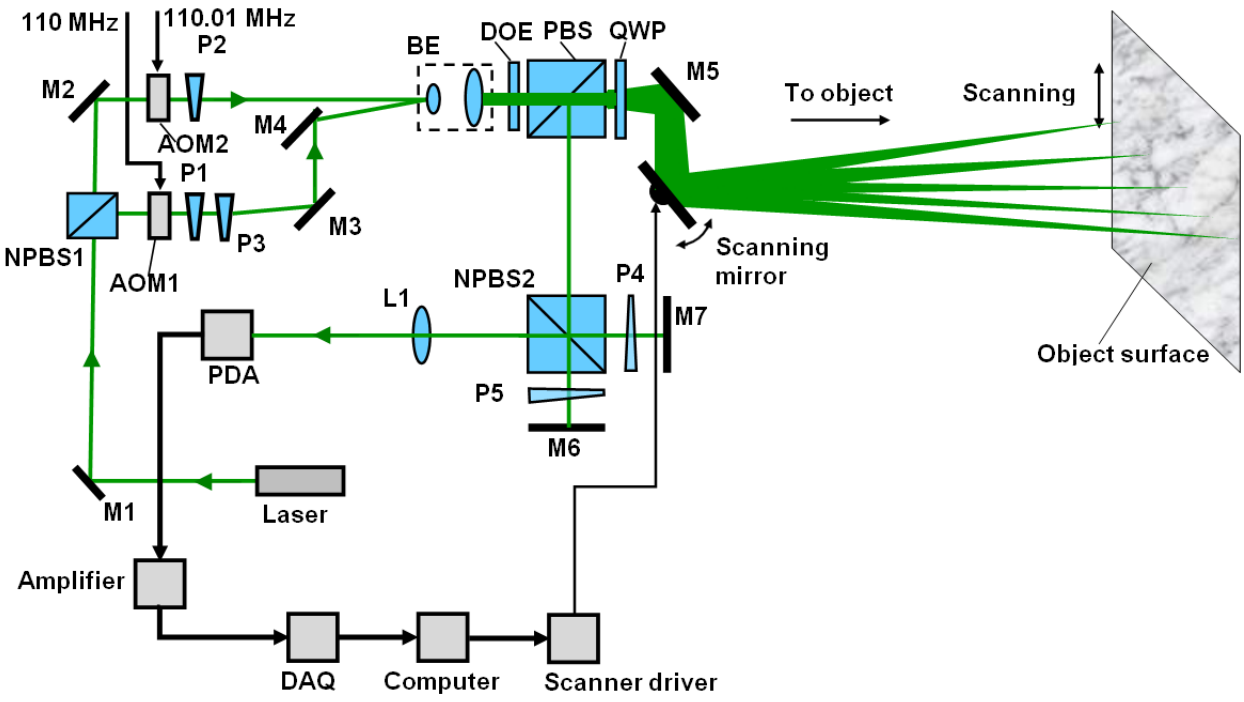

Figure 2. Optical schematic of LMBDIS. M1-M7- mirror, NPBS1, 2 - non-polarizing beam splitter, AOM1, 2- acousto-optic modulator, PBS - polarizing beam splitter, QWP- quarter wave plate, P1-P5 - wedge prism, BE- beam expander, DOE- diffraction optical element, L1 - lens , PDA - photodiode array, DAQ - multi-channel data acquisition system.

4 Method of precise angular alignment of an optical beam using an optical wedge

Optical schematic of the LMBDIS employs optical wedges for precise angular alignment. Wedges P1-P3 are used to precisely align beams of different frequency in the linear array of beams. Wedges P4 and P5 are used for alignment of the Michelson interferometer. Traditionally, angular adjustment of an optical beam is implemented by tilting a mirror that reflects the beam. As shown in Figure 3, rotation of the mirror by the angle Θ from position 1 to position 2 changes the direction of the reflected beam by angle 2Θ. Accurate angular adjustment of the beam requires high precision mirror mounts. For example, adjustment of the direction of the beam by 4 arc-seconds (typical number for alignment of a laser interferometer) requires the angular motion of the mirror by 2 arc-second. High precision mechanical devices for angular adjustment of a mirror could be expensive and bulky. Achievement of temporal stability of the angular position of a mirror results in even more sophisticated and expensive devices. We proposed angular alignment of an optical beam by tilting an optical wedge (prism) around the axis parallel to the optical surfaces of the prism, (by changing the angle of incidence of the beam on the prism). The principle of using an optical wedge for angular alignment of an optical beam is

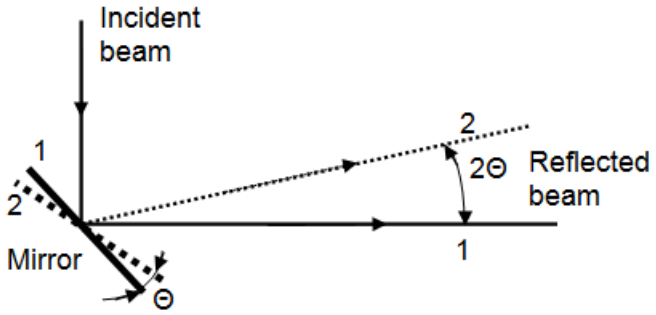

Figure 3. Angular adjustment of an optical beam by tilting a mirror

shown in Figure 4. An optical wedge deviates the incident beam by the angle D. Large tilt Θ_I of the wedge results in small angular translation Θ_O of the deviated beam.

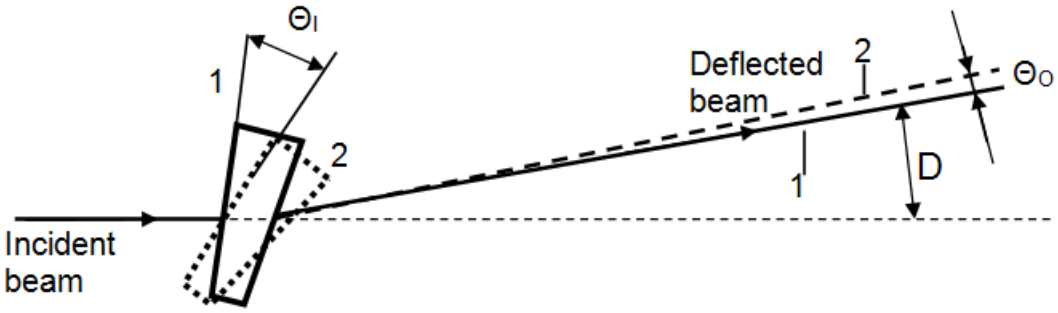

Figure 4. Principle of angular adjustment of an optical beam by tilting an optical wedge(prism) around the axis parallel to the optical surfaces of the prism.

The principle is based on the well-known fact that for the "thin" prism (small vertex angle), the deviation angle depends slightly on the angle of incidence. In more detail, the beam deviation angle by a refractive prism, shown in Figure 5, is expressed as follows[22]

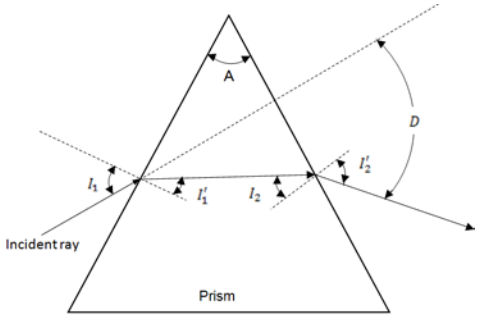

Figure 5. The deviation of a ray by a refracting prism.

$$D = I_1 - A + arcsin\left[(n^2 - sin^2 I_1)^{1/2}\, sinA - cosA\, sinI_1\right] \qquad (5)$$

where I_1 is the angle of incidence, n is the index of refraction of the prism, and A is the vertex angle of the prism.

An example of the dependence of the deviation angle on the angle of incidence for a prism with vertex angle A = 2° is shown in Figure 6.

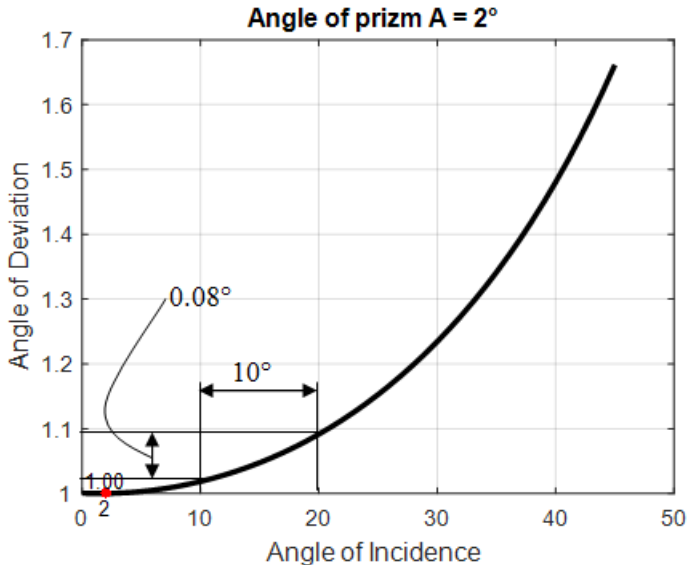

Figure 6. Dependence of the deviation angle on the angle of incidence of the beam for the optical wedge with the 2° vertex angle.

Shown in Figure 6, the change of the angle of incidence by 10°, from 10° to 20° causes a small 0.08° change of the deviation angle. So, small angular adjustments of the beam can be achieved with a large rotation angle of the prism. For example, for that particular prism, the angular adjustment of the beam by 4 arc seconds can be achieved by rotating the prism by 0.14°. The sensitivity of the angular adjustment can be selected by selecting the vertex angle of the prism and the initial angle of incidence. The proposed method doesn't require a high precision mechanical device, and it is also considerably less critical to mechanical instabilities, as compared to the adjustment using a mirror. Figure 7 shows a schematic of a laser Michelson interferometer that uses two optical wedges for precise alignment. Two wedges provide angular adjustments of beams in orthogonal directions.

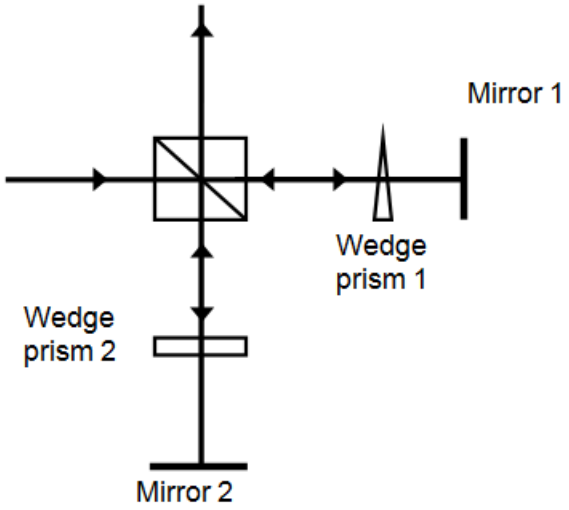

Figure 7. Layout of Michelson interferometer with two optical wedges for angular alignment.

5 Signal demodulation

Heterodyne 10 kHz carrier signals recorded into computer memory are processed digitally. Frequency demodulation of heterodyne signals has been implemented digitally using an I&Q demodulation technique. The frequency demodulation of the signals provides relative velocities and displacements between corresponding points on the object. Figure 8 shows a basic functional layout of a digital I&Q demodulator for a single channel.

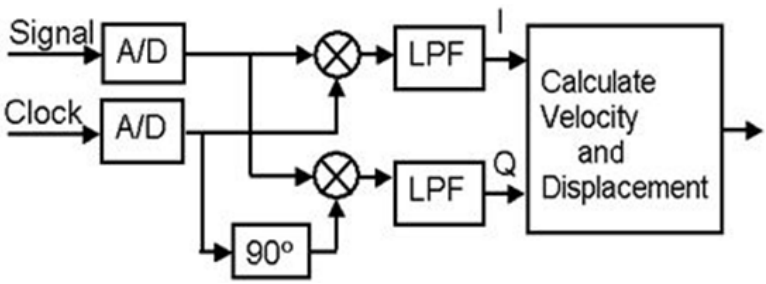

Figure 8. Functional layout of the digital I&Q demodulator for a single channel.

Heterodyne FM signals from amplified PDA outputs and the 10 kHz reference clock are simultaneously sampled with a multichannel dynamic signal acquisition device. The reference clock signal is generated by the AOMs driver. The reference clock is phase shifted by 90 degrees in software. Then the reference clock and the phase shifted reference clock are each multiplied with each of the FM signals, producing I&Q signals after low pass filtering (LPF). From the obtained I&Q waveforms, the relative vibration velocity $V(t)$ and displacement $X(t)$ between each pair of corresponding points on the object is calculated in the software by using expressions:

$$V(t) = \frac{\lambda}{4\pi}\left[\frac{I(t)\cdot Q\prime(t) - Q(t)\cdot I\prime(t)}{I^2(t)+Q^2(t)}\right] \quad (6)$$

$$X(t) = \frac{\lambda}{4\pi} tan^{-1}\left[\frac{Q(t)}{I(t)}\right] \quad (7)$$

where λ=532 nm is the wavelength of the laser light, and $I'(t)$ and $Q'(t)$ are the time derivatives of the $I(t)$ and $Q(t)$ components of the signal, respectively. A Matlab code for I&Q demodulation has been developed and used for extraction of relative vibration velocity and displacement signals from LMBDIS heterodyne signals. The velocity signals from LMBDIS channels are used to form a vibration velocity image of the scanned area in a selected frequency band.

6 Creating vibration image using a spectrogram approach

A vibration image shows the spatial distribution of the vibration amplitude over the scanned area of the object. The vibration image can be obtained by calculating a spectrogram of all LMBDIS channels. The spectrogram is a graphical display of magnitude of the discrete short-time Fourier transform (STFT). Figures 9 - 11 show an example of creating a vibration image of the ground surface area over a buried object scanned with the LMBDIS beams. The beams were scanning the ground for approximately two seconds. Figure 9 shows a velocity signal of one of the LMBDIS channels.

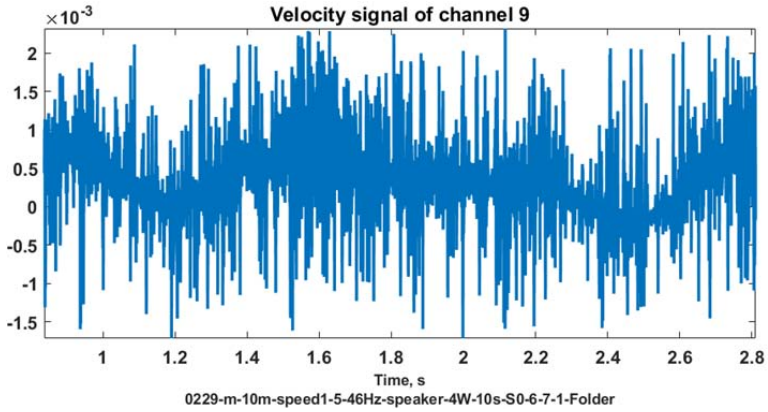

Figure 9. Velocity signal of one of the LMBDIS channels scanning ground.

Figure 10 shows the FFT of velocity signal of all LMBDIS channels calculated over two seconds. Shown in Figure 10, the object has a strong response at the frequency range from 40 Hz to 50 Hz. But a location of the object could not be obtained from the FFT of the signals.

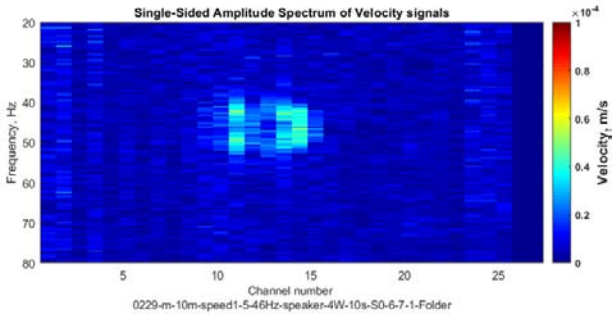

Figure 10. FFT of LMBDIS velocity signals calculated over the time of scanning.

Figure 11 shows an example of STFT of the velocity signals of two channels, channels 10 and 12.

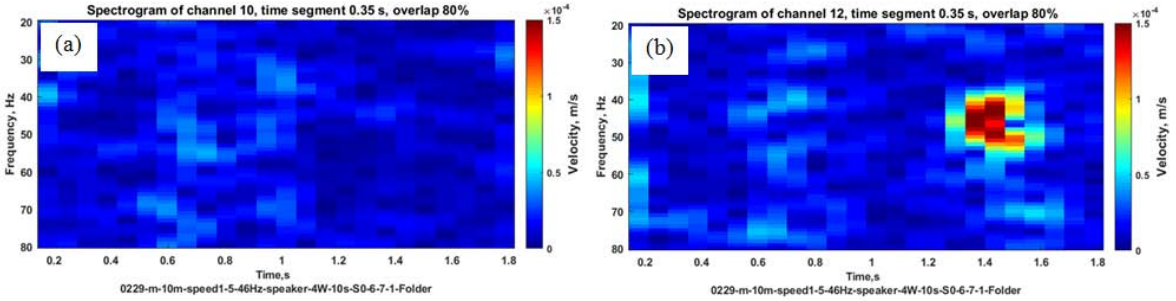

Figure 11. STFT of the velocity signals of two channels, number 10 (a) and 12 (b).

Spectrograms for all channels are calculated, and magnitudes for a selected frequency band are assembled into a matrix, where columns represent channel numbers, thereby creating a vibration image for a selected frequency band. Figure 12 shows a vibration image of the scanned area for three frequencies: 40 Hz, 46 Hz, and 51 Hz and indicates that the buried object has a maximum response at 46 Hz.

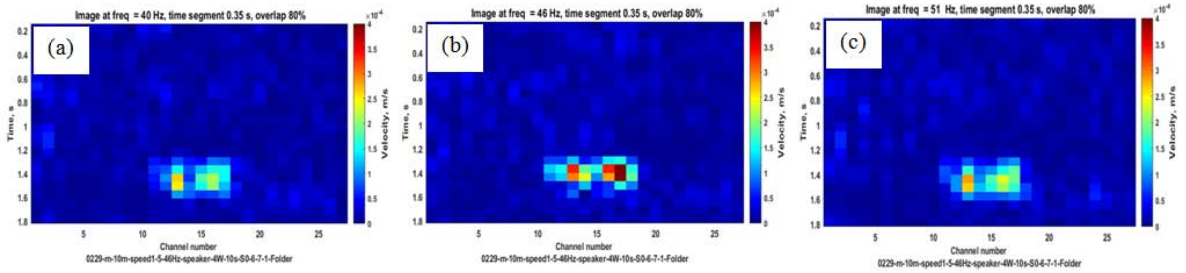

Figure 12. Vibration image of the scanned area for three frequencies: 40 Hz (a), 46 Hz (b), and 51 Hz (c).

7 Creating vibration image based on Hilbert transform of LMBDIS signals

Vibration imaging based on discrete short-time Fourier transform can result in poor frequency resolution for fast scanning of the object due to short measurement time. We developed an approach of using a Hilbert transform of LMBDIS signals to create a vibration image in order to overcome the limitation on the speed of beams caused by discrete Fourier transform. This approach allows creating a vibration image using time domain LMBDIS signals.

The Hilbert transform is used to calculate a new time signal hvj(t) from the original time signal vj(t) and is defined by the following expression:

$$hv_j(t) = \frac{1}{\pi}\int_{-\infty}^{\infty} \frac{v_j(\tau)}{t-\tau} d\tau, j = 1..N \quad (8)$$

The magnitude $a_j(t)$ of the analytic signal can be calculated from hvj(t) and vj(t) by using the following expression[23]:

$$a_j(t) = \sqrt{v_j^2(t) + ihv_j^2(t)},\ j = 1..N \quad (9)$$

The magnitude of the analytic signal is the envelope of the original signal, which shows how the vibration amplitude changes with time. So, a vibration image of a scanned area in a selected narrow frequency band could be created by using values of the magnitude of the analytic signal.

Figure 13 shows a block-diagram of the developed algorithm for creating a vibration image by using Hilbert transform of LMBDIS signals.

The algorithm works as follows. First, a time segment of LMBDIS signals that corresponds to a scanned area is selected. Then, the selected signals are frequency demodulated using digital I&Q demodulation. The demodulation reveals the relative velocity signals of all LMBDIS channels. The relative velocity signals are then band-pass filtered around the frequency of interest. Then, the Hilbert transform is applied to the obtained narrow-band velocity signals, and the magnitude $a_j(t)$ of analytical signal is calculated for each channel. The magnitude of analytical signal is used to create a relative vibration image. Operation of the algorithm is illustrated by Figures 14 - 21.

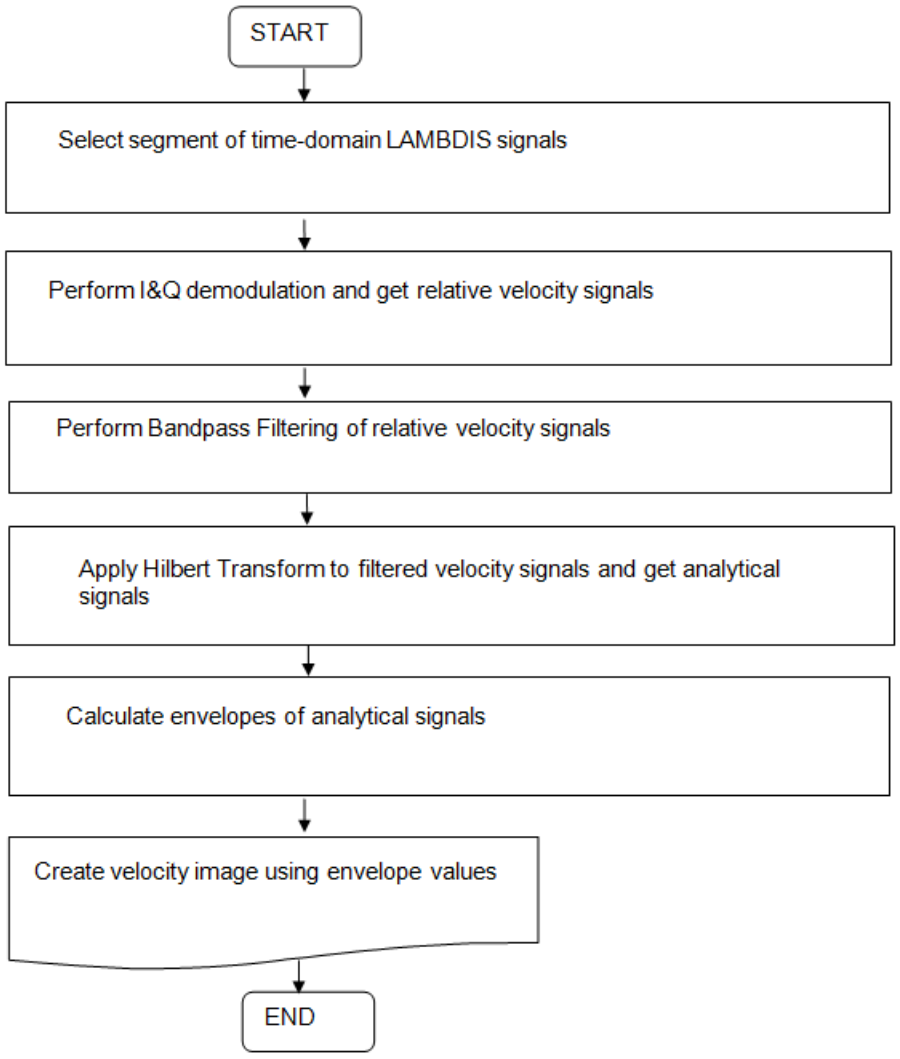

Figure 13. Block-diagram of the algorithm for creating a vibration image by using Hilbert transform of LMBDIS signals

Figure 14 shows a time segment of one of the LMBDIS signals with a duration corresponding to a two-meter path length on the ground surface scanned by the laser beams due to motion of the vehicle. The object, buried in the scanned area, was excited with a loudspeaker. Figure 15 shows a pass-band filtered demodulated velocity signal, obtained by digital demodulation of the signal shown in Figure 14. One can see that the signal amplitude above the buried object is significantly higher than the rest of the signal. A two-dimensional map that shows the vibration velocity spatial distribution over the scanned area, which was created by combining time domain pass-band filtered demodulated velocity signals of all channels, is shown in Figure 16.

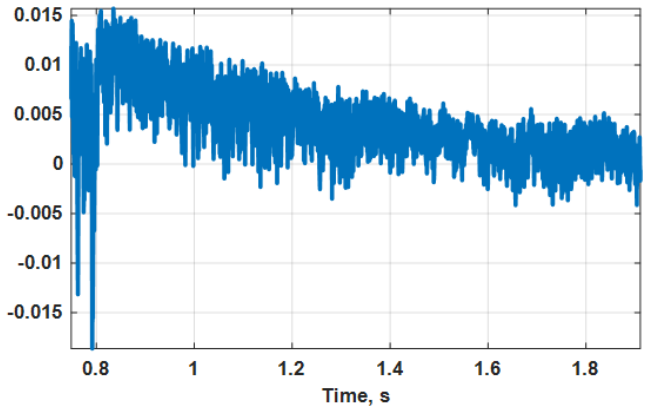

Figure 14. Time segment of one of LMBDIS signals that corresponds to two meters path length on the ground surface scanned by the laser beams due to motion of the vehicle.

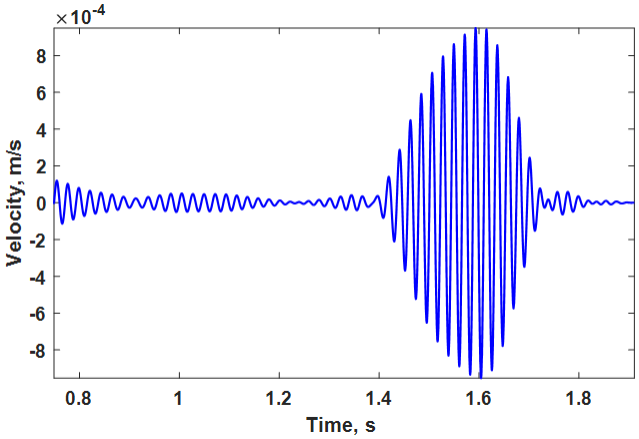

Figure 15. Band-pass filtered demodulated velocity signal on one of the LMBDIS channels that corresponds to two meters path length on the ground surface scanned by the laser beams due to motion of the vehicle.

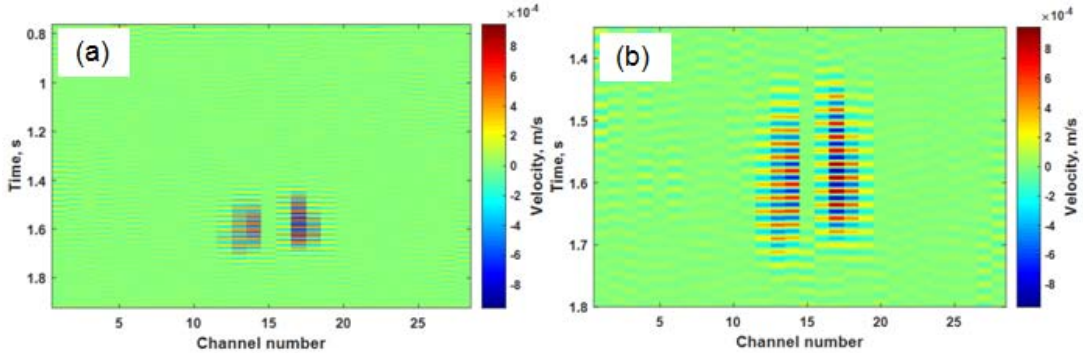

Figure 16. A two-dimensional map (a) that shows the vibration velocity spatial distribution over the scanned area created by combining time domain pass-band filtered demodulated velocity signals of all channels and a blown up image (b) of the area above a buried object.

The original velocity signal displays oscillations and includes positive and negative values. The area above the buried object is clearly seen in Figure 16, as the area with higher vibration amplitude. The envelope of the signal is a positive function and could better display a buried object. Figure 17 shows an example of the original pass-band filtered demodulated

velocity signal, the same as shown in Figure 15, its Hilbert transform, and the envelope calculated by using the expression (9).

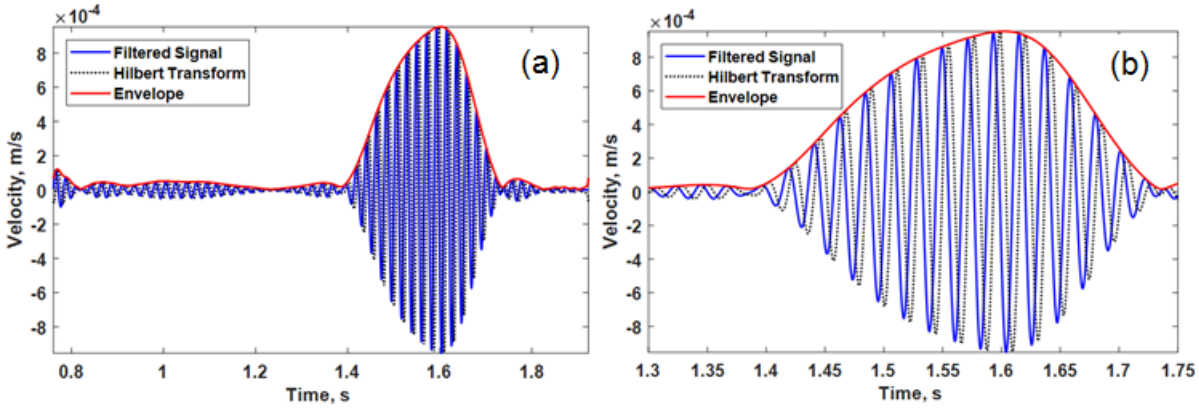

Figure 17. Band pass filtered demodulated velocity signal on one of the LMBDIS channels, its Hilbert transform, and the envelope (a), and the blown up part of the graph (b).

Figure 18 shows a two-dimensional vibration velocity image, which was created by combining envelopes of LMBDIS velocity signals of all channels.

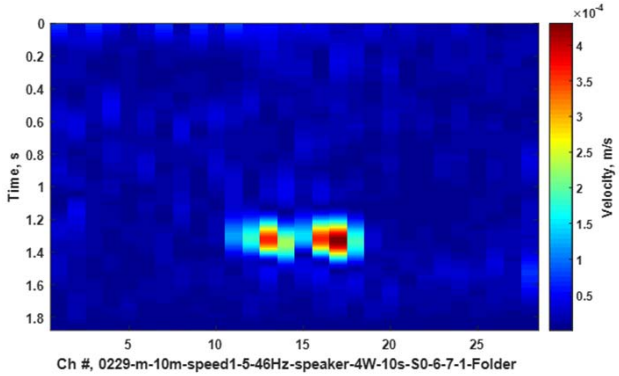

Figure 18. Vibration velocity image based on Hilbert transform, created by combining envelopes of LMBDIS velocity signals of all channels.

A vibration image of the same object created by using a short-time Fourier transform is shown in Figure 19. Each column of data matrix corresponds to the LMBDIS channel and contains an estimate of the short-terms, time-localized frequency contents. For the selected frequency 46 Hz, the length of time segment was specified to be 0.35 sec with a 80% overlap.

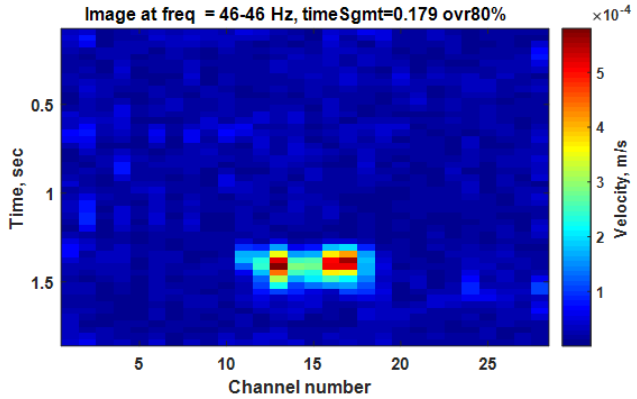

Figure 19. Vibration image of the same object created by calculating a spectrogram for each channel and combining together the mean values of the signal.

In Figures 18 and 19, the vibration image based on envelopes of the time domain signals looks very similar to the vibration image based on spectrogram approach.
The algorithm of image processing using the Hilbert transform shows some advantage in comparison to the algorithm using the short-time Fourier transform in producing smoother profiles above the vibration object, as shown in Figure 20.

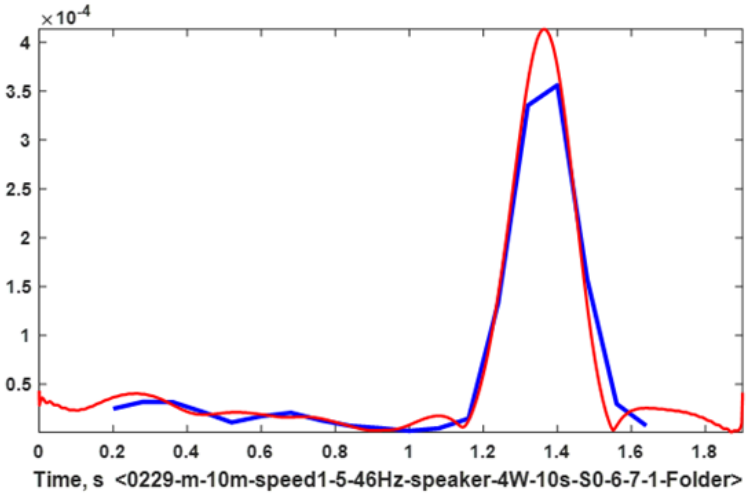

Figure 20. Velocity profiles for channel 17 obtained from envelope of analytic signal (red) and from short-terms, time-localized frequency contents(blue)

8 Algorithm for creating magnitude and phase vibration image

The LMBDIS provides a relative vibration velocity magnitude and phase profile along the line of beams, since signals for all channels are measured simultaneously and the vibration phase relation between channels is preserved. However, when the beams move in the transverse direction to obtain a vibration image of the interrogated area, the phase information between contiguous parts of each channel is lost. As a result, a vibration image created by combining FFTs of contiguous time segments of each channel shows only vibration magnitude in the

direction of scanning. An example of a vibration image of a circumferentially clamped circular plate excited at its (0,1) spatial mode is shown in Figure 21. The image shows two lobes, which represent a gradient of bell shape deformation of the vibrating plate. One can see that phase vectors are arranged regularly for each time segment of the image; vectors are oriented in the same direction for one lobe, and in the opposite direction for the other lobe. However, direction of vectors is changed between the contiguous segments while all segments of each lobe have the same vibration phase.

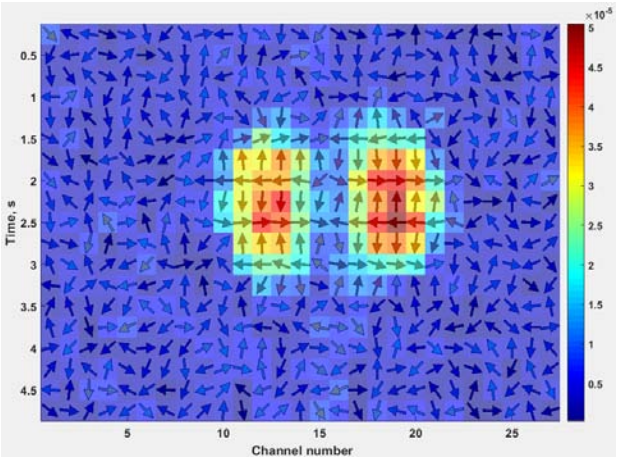

Figure 21. Vibration image of a circumferentially clamped circular plate created by combining FFTs of contiguous time segments of each channel.

In order to correctly show the phase in the vibration image, the phase of LMBDIS signals should be related to an excitation signal. Correct representation of phase in a vibration image can be accomplished by calculating the frequency response function (FRF) of the object using the excitation signal as a reference. The FRF can be approximated through the estimator $H1_j[f]$ [24], and be calculated using the following expression:

$$FRF_j = \frac{R[f]^* V_j[f]}{R[f]^* R[f]} \tag{10}$$

where $V_j[f]$, and $R[f]$ are Fourier transforms of vibration velocity signal $v_j(t), j = 1..N$, and the reference channel $r(t)$ respectively, N is the number of LMBDIS channels, $R[f]^*$ is the conjugated complex of $R[f]$, $R[f]^* R[f]$ is the auto spectrum of the reference signal, and $R[f]^* V_j[f]$ is the cross spectrum of the reference signal and j-th vibration velocity signal.
Complex numbers $R[f]$, $R[f]^*$, $V_j[f]$ can be described in polar form with a magnitude and a phase using Euler's formula

$$R[f] = |R[f]| e^{i(2\pi f t + \varphi_0)} \tag{11}$$

$$R[f]^* = |R[f]| e^{i(-2\pi f t - \varphi_0)}) \tag{12}$$

$$V_j[f] = \left|V_j[f]\right| e^{i(2\pi f t + \theta_{0j})} \tag{13}$$

where φ_0, θ_{0j} are zero phase angles of the reference signal and velocity signals v_j. Substituting the expressions (2) - (3) into (1) and using a reference signal with normalized magnitude $|R[f]| = 1$, one gets

$$FRF_j = \frac{R[f]^* V_j[f]}{R[f]^* R[f]} = \frac{e^{i(-2\pi ft-\varphi_0)}|V_j[f]|e^{i(2\pi ft+\theta_{0j})}}{e^{i(2\pi ft+\varphi_0)}e^{i(-2\pi ft-\varphi_0)}} = |V_j[f]|e^{(\theta_{0j}-\varphi_0)}, j = 1..N \quad (14)$$

From equation (14) the FRF shows the magnitude and the phase of the velocity signal.

The algorithm to calculate the magnitude and phase of the vibration velocity signals is shown in Figure 22.

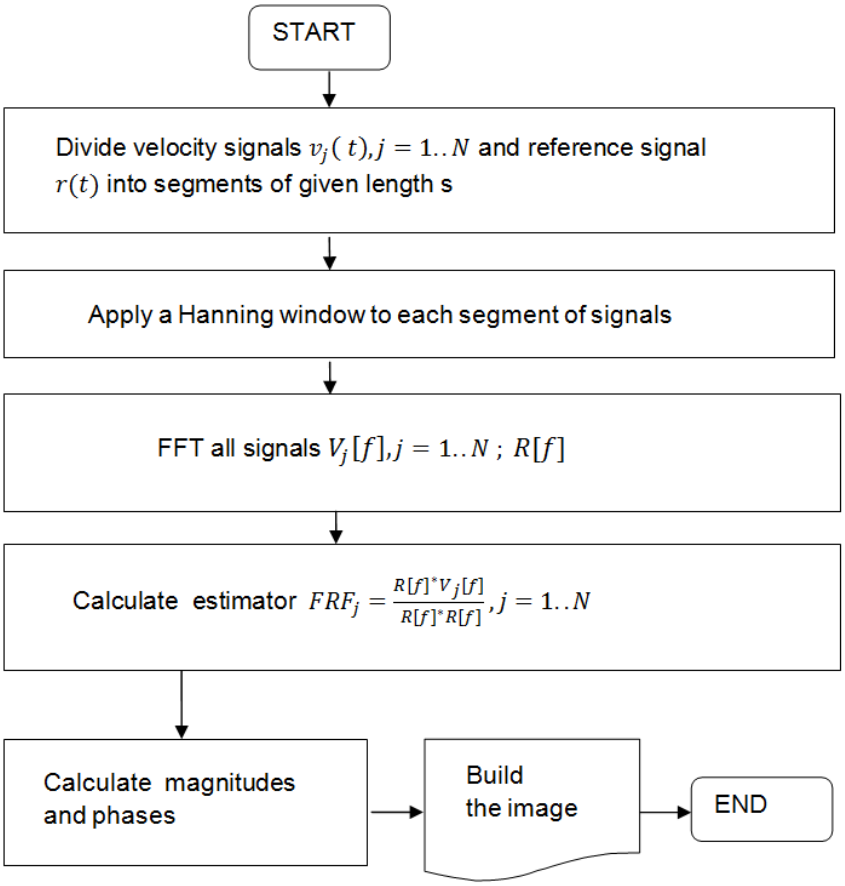

Figure 22. The algorithm to calculate the magnitude and phase of the vibration velocity signals using an excitation signal as a reference.

Figure 23 shows a vibration image created by using the described algorithm of the same circumferentially clamped circular plate. Contrary to the image in Figure 21, the image in Figure 23 shows the same phase for each lobe. That allows for the sign of the relative velocity and the deformation gradient. Figure 24 shows a 3D relative vibration image of the circumferentially clamped circular plate that uses the magnitude and phase information.

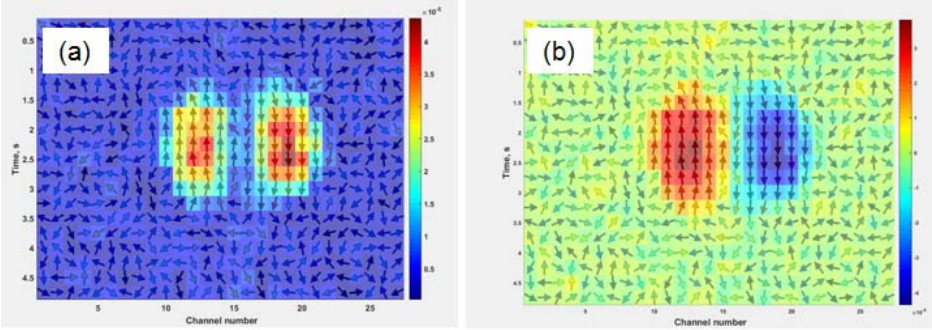

Figure 23. Vibration image of a circumferentially clamped circular plate created by calculating the FRF of each channel using the excitation signal as a reference. (a) - magnitude and phase image, (b) - magnitude and phase image, with magnitudes multiplied by the sign of phase.

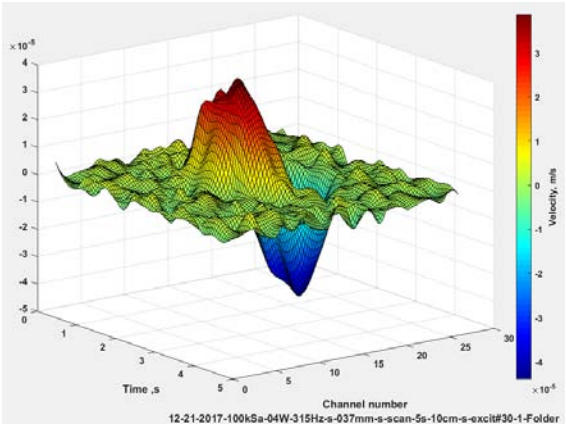

Figure 24. 3D vibration image of a circumferentially clamped circular plate created by calculating the FRF of each channel using the excitation signal as a reference.

9 Vibration image obtained by LMBDIS in comparison with scanning LDV

A vibration image obtained with the LMBDIS is different from a vibration image obtained with a scanning LDV. Vibration images obtained with the LMBDIS show relative vibration velocity between corresponding points on the object, while a LDV measures vibration velocity of the object relative to the LDV itself. The difference between the LMBDIS and LDV measurement is illustrated in Figure 26. Figure 26 shows an example of a vibration measurement of a circumferentially clamped 250 mm diameter circular plywood plate, glued to a rectangular frame, whose photograph is shown in Figure 25. The 250 mm diameter of the plate is in the range of the sizes of a pressure plate of plastic anti-tank (AT) mines. The plate was excited at its natural frequency of 314 Hz using a loudspeaker located behind the plate to obtain an axial symmetric vibration mode shape. Vibration at this mode produces dynamic deformation of the surface, similar in shape to the deformation of the surface above a buried anti-tank AT mine. The object, a function generator, and an amplifier to provide the excitation signal were mounted on a wheeled rack.

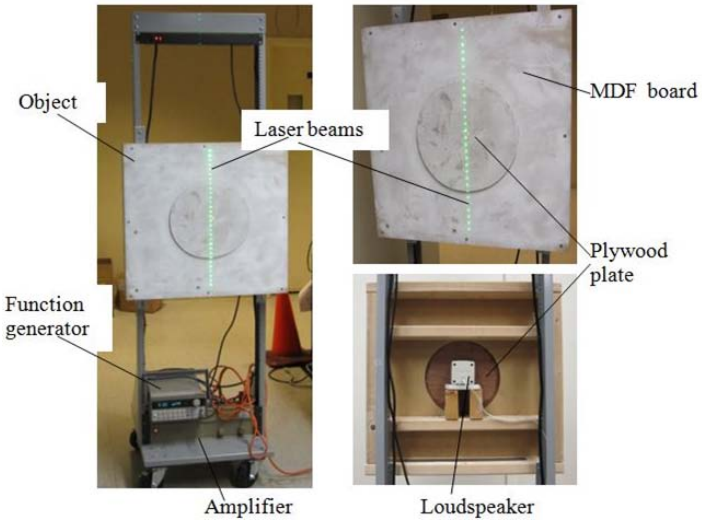

Figure 25. Photograph of the test object setup: a circumferentially clamped 250 mm (~10 inch) diameter circular plywood plate excited with a loudspeaker

Vibration of the object was measured by scanning the LMBDIS beams across the object at a speed of beams of 20 cm/s and also with a scanning LDV Polytec PSV 300. Figure 26 (a) - (c) shows the 2D and 3D vibration velocity image of the object, and the spatial vibration velocity profile across the center of the object obtained with the scanning LDV. Figure 26 (d) - (f) shows the 2D and 3D relative vibration velocity image of the object, and the spatial relative vibration velocity profile obtained with the LMBDIS.

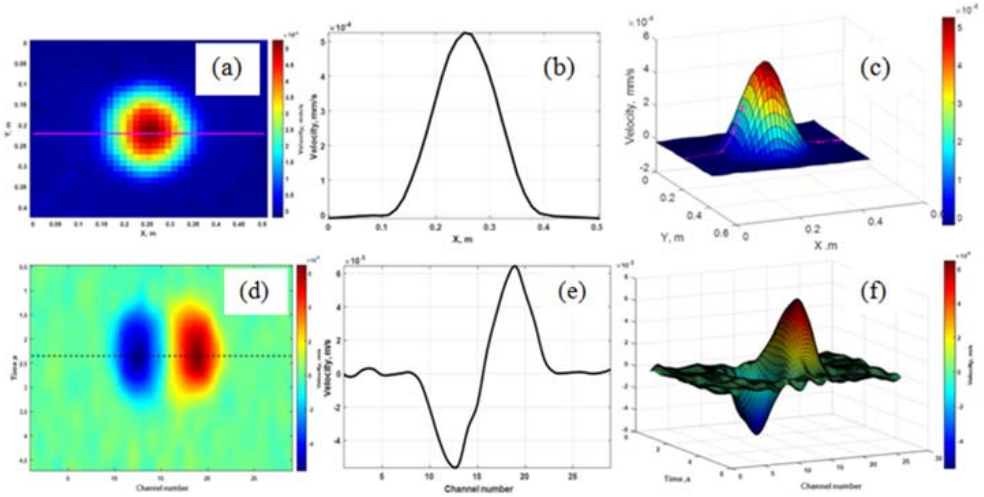

Figure 26. Vibration velocity image (a) and (c) and the velocity profile across the center of the plate (b) of a vibrating circumferentially clamped circular plate obtained with a scanning LDV, and the relative velocity image (d) and (f) and the relative velocity profile (e) measured with LMBDIS.

Figure 26 illustrates the difference between the LMBDIS and LDV measurement results. LMBDIS measures relative vibration velocity between corresponding points on the object, while a LDV measures vibration velocity of the object relative to the LDV. Spatial relative velocity profile measured with LMBDIS could be treated as a gradient of the spatial velocity profile measured with a LDV, if the interval between corresponding points on the object is considerably smaller than the size of the deformation profile.

10 Assessment of LMBDIS sensitivity to vibration of a buried object

Sensitivity of the LMBDIS to vibration of a buried object has been assessed experimentally in the laboratory. The measurements were conducted by obtaining vibration images of a buried object excited with a loudspeaker. A layout of the experimental setup is shown in Figure 27.

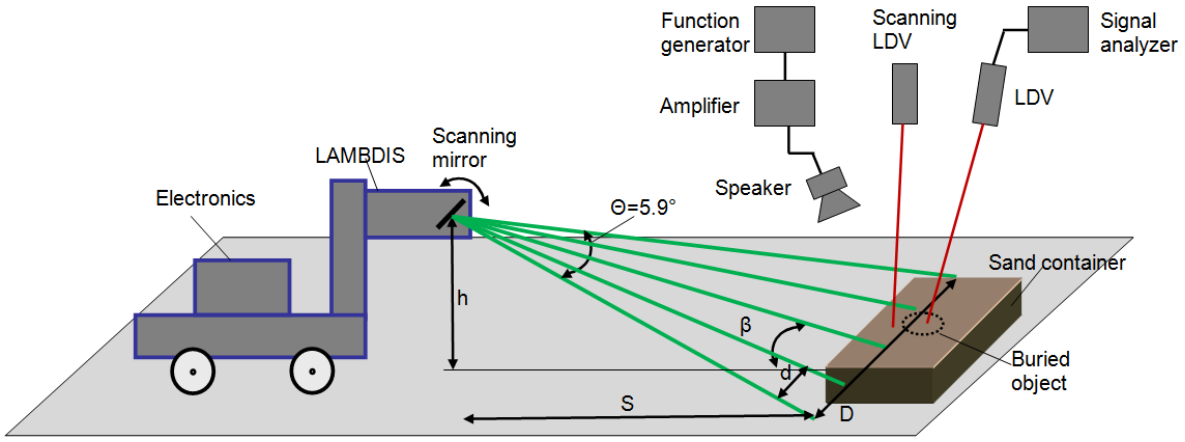

Figure 27. Functional layout of the experimental setup for assessment of LMBDIS sensitivity.

A linear array of 30 beams from the LMBDIS output is horizontal, directed to the floor surface at an angle which depends on the standoff distance S. A metal circular container 22 cm in diameter buried flush in a 1 m x 1 m size sand container was used as an object. The following geometrical parameters were used in the experiments: the height of the beams above the sand surface h = 216 cm, the standoff distance S = 10 m, and the grazing angle of beams β = 12°. The spread of beams on the sand surface D = 103 cm and the distance between the neighboring beams d = 3.6 cm. The shear between interfering beams was equal to three inter-beam intervals. So, the LMBDIS was measuring the relative velocities between corresponding points illuminated with beams 1 and 4, beams 2 and 5, and so on. The separation between corresponding points was 10.8 cm. A photograph of the object buried in the sand container is shown in Figure 28. Two metal strips were located on the edges of the sand container to provide spikes in LMBDIS signals due to the strips high reflectance. These spikes were used as markers to accurately calculate the speed of laser beams over the object. Vibration of the object was excited with a loudspeaker and was measured first with a scanning LDV PSV300, Polytec, Inc. The resonance frequency of the object was found to be 120 Hz. The sensitivity was estimated by obtaining a vibration image of the sand surface excited at 120 Hz frequency, while gradually, step by step, reducing the excitation level. Vibration of the sand at each step was also measured with the scanning LDV,

used as a reference sensor. Vibration of the sand surface above the center of the object was monitored using a single point LDV, PDV100, Polytec, Inc., and a signal analyzer, Agilent 35670A. The LMBDIS vibration images were obtained by scanning the beams across the sand surface at 10 cm/s from a stationary vehicle.

The vibration velocity images and velocity profiles obtained with LMBDIS and the scanning LDV for different amplitudes of vibration, are shown in Figures 29-32.

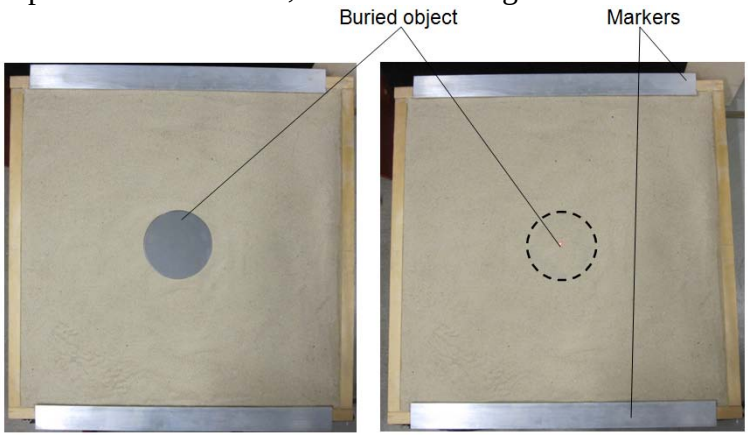

Figure 28. A photograph of the object buried in the sand container.

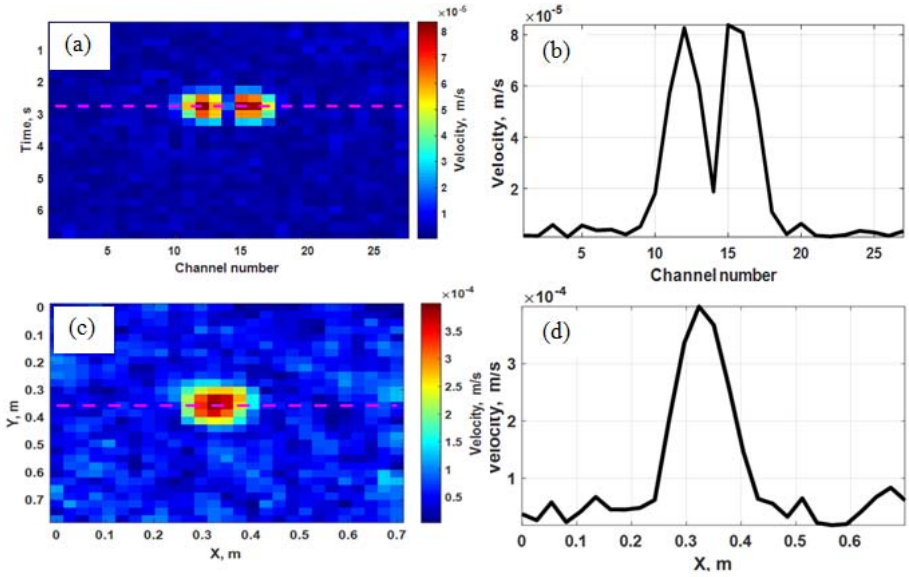

Figure 29. Vibration image of a buried object with a vibration magnitude of 0.4 mm/s rms above the center of the object. (a) and (b) - vibration velocity magnitude image and velocity magnitude profile obtained with LMBDIS, (b) and (c) - vibration velocity magnitude image, and a velocity magnitude profile obtained with a scanning LDV.

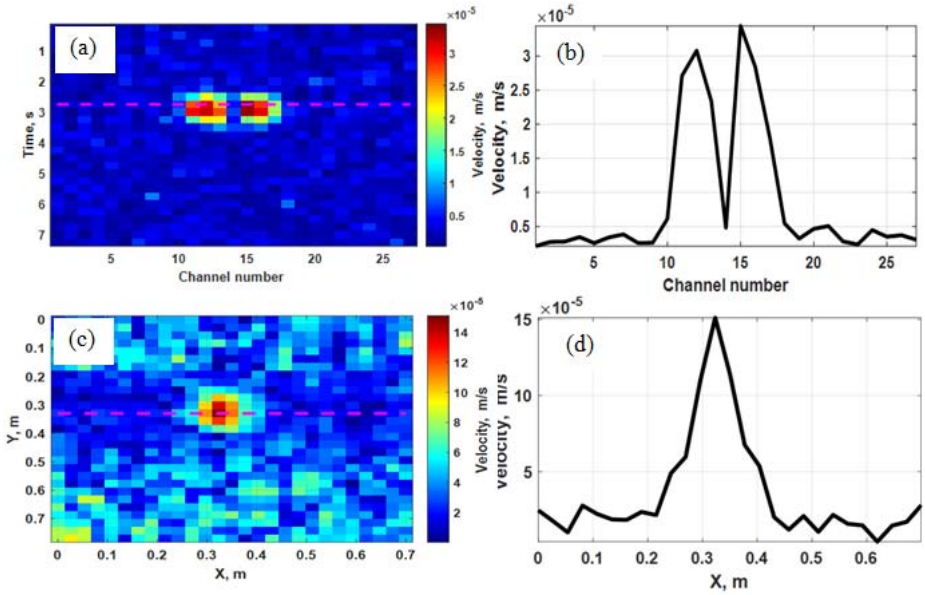

Figure 30. Vibration image of a buried object with a vibration magnitude of 0.15 mm/s rms above the center of the object. (a) and (b) - vibration velocity magnitude image and profile obtained with LMBDIS, (b) and (c) - vibration velocity magnitude image, and a profile obtained with a scanning LDV.

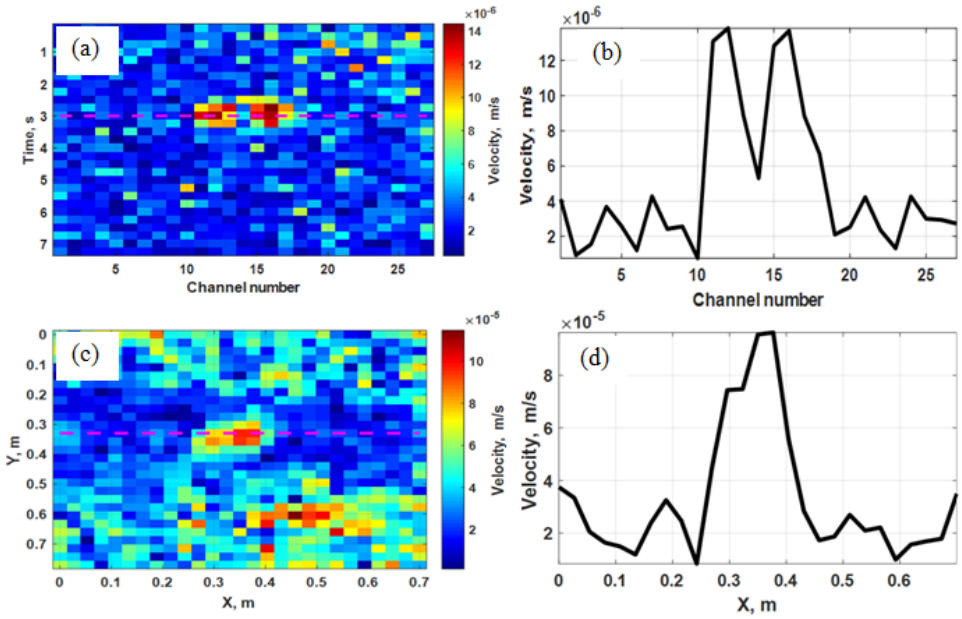

Figure 31 Vibration image of a buried object with a vibration magnitude of 0.09 mm/s rms above the center of the object. (a) and (b) - vibration velocity image and profile obtained with LMBDIS, (c) and (d) - vibration velocity image and profile obtained with a scanning LDV.

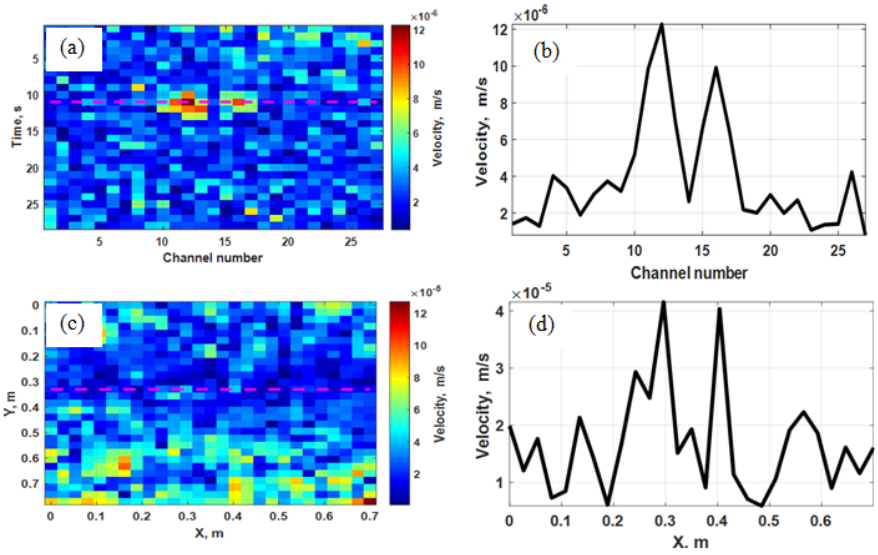

Figure 32. Vibration image of a buried object for vibration excited with ambient room noise. (a) and (b) - vibration velocity image and profile obtained with LMBDIS, (c) and (d) - vibration velocity image and profile obtained with a scanning LDV.

Vibration images obtained with the LMBDIS show relative vibration velocity between corresponding points on the object, while a LDV measures vibration velocity of the object relative to the LDV itself. One can see from Figures 29-32 that the contrast of the vibration image decreases with the decrease of the excitation level. When there was no excitation applied from the loudspeaker, the object vibration was excited by ambient acoustic and vibration noise of the room. One can see from Figure 32 that the buried object was detectable from the LMBDIS vibration image, but was not seen on the scanning LDV vibration image. A possible reason that the object was not seen on the scanning LDV image is that the relative vibration between the LDV and the sand container was higher than the vibration of the object at the time of measurements. One can see from Figures 29-32 that off target relative velocity of the sand surface measured with LMBDIS was below 4 μm/s. Assuming that the sand surface exhibits out-of-plane vibration, the actual velocities are (1/Sinβ) = 4.8 time higher. So, the off target relative velocity of sand surface measured with LMBDIS was below 19 μm/s. As shown in Figure 32 (a, b), the object was detected without the loudspeaker excitation provided. The vibration was caused by ambient room noise. The maximum on target relative velocity was approximately 60 μm/s, or three times higher than the velocity off target. It should be noted, that the measured LMBDIS performance was not limited by the LMBDIS itself, but the whole setup, especially by the ambient noise.

11 Investigation of LMBDIS performance for different speed of beams

The ability of the LMBDIS to detect a buried vibrating object has been investigated in laboratory.

Laboratory experiments on the detection of a buried object have been conducted in the scanning and moving modes. A circular shape mechanical shaker (model UW30, Electro-Voice, Inc.), buried one inch deep in a 1 x 1 meter size sand container, was used as a vibrating object. A

photograph of the shaker buried in the sand container is shown in Figure 33. The distance between the LMBDIS and the measured object was limited by the laboratory space and was S = 7.5 m. The beams were incident onto the sand surface at grazing angle $\beta = 16°$. The inter-beam interval was 25 mm on the sand surface, and the spread of beams was 725 mm. The shear between interfering beams was equal to one inter-beam interval. So, the LMBDIS was measuring the relative velocities between corresponding points illuminated with neighboring beams, for example beams 1 and 2, beams 2 and 3, and so on. Beams on the sand surface were defocused in order to reduce the speckle noise caused by the beams motion, and their diameter was approximately 9 mm. The shaker was excited at 180 Hz single frequency tone. A scanning LDV PSV300, Polytec, Inc. was used as a reference sensor to measure vibration of the sand surface.

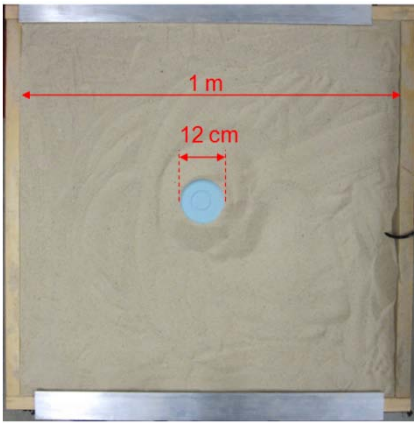

Figure 33. A photograph of the shaker buried in 1 m x 1 m size sand container

Figure 34 shows an example the vibration velocity image of sand surface above the shaker and the velocity profile along the X-direction across the center of the shaker measured with a scanning LDV. The maximum velocity of the sand surface above the shaker shown in Figure 8 was approximately 1.2 mm/s. The LMBDIS measurements were conducted for four different values of the maximum velocity of the sand surface above the shaker: 1.2 mm/s, 0.6 mm/s, 0.3 mm/s, and 0.15 mm/s. Figures 35 - 38 show the vibration velocity image of the area measured with the LMBDIS in the moving mode. Figure 35 shows the vibration velocity image of the area measured with the LMBDIS in the moving mode for 1.2 mm/s velocity of the sand surface above the shaker. The measurements were done for different speeds of vehicle: 0.6 m/s, 1.7 m/s, 2.8 m/s, and 3.8 m/s. The maximum speed was limited by the short distance to ramp up to speed.

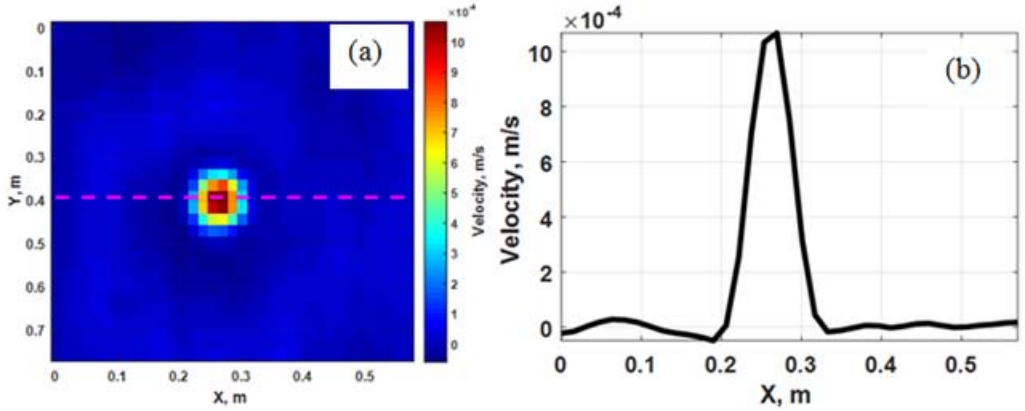

Figure 34. Vibration velocity image (a) of sand surface above the shaker and the velocity profile along the X-direction across the center of the shaker (b) measured with a scanning LDV

Figure 35 shows that the buried object was detected for each speed of the vehicle motion, and that the velocity noise increases with the speed.

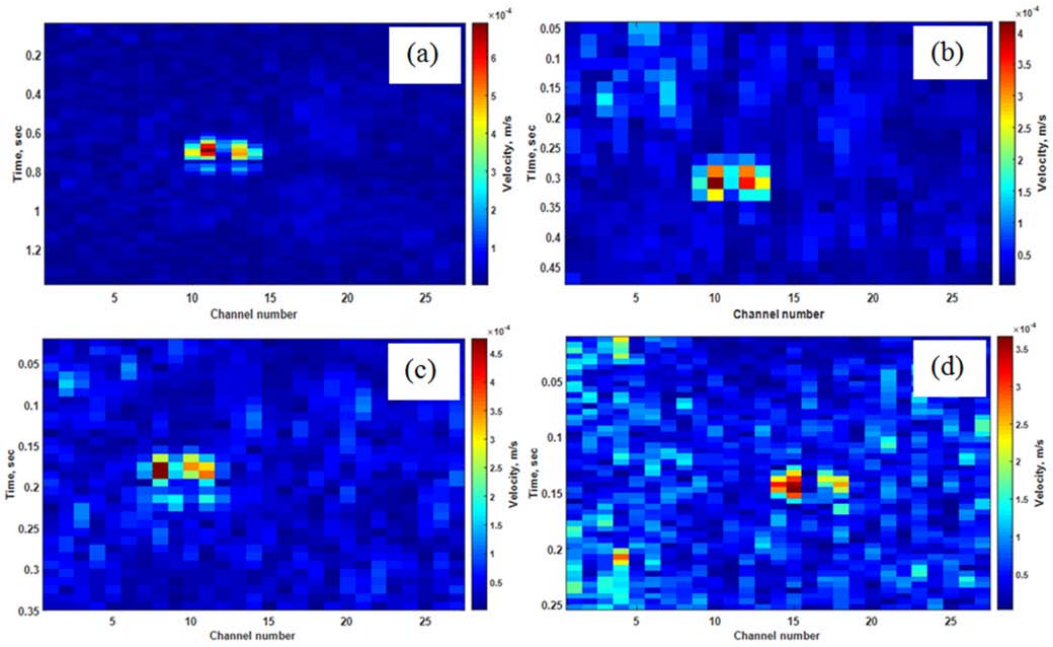

Figure 35. Vibration image of sand surface above the shaker obtained with the LMBDIS in a moving mode for 1.2 mm/s velocity of the sand surface above the shaker for different speeds of vehicle: (a) - 0.6 m/s, (b) - 1.7 m/s, (c) - 2.8 m/s, (d) - 3.8 m/s.

Figure 36 shows the vibration velocity image of the area measured with the LMBDIS in the moving mode for 0.6 mm/s velocity of the sand surface above the shaker. The measurements were done for different speeds of vehicle: 0.54 m/s, 0.87 m/s, 1.47 m/s, 2.2 m/s, 2.8 m/s, and 2.9 m/s. The maximum speed of vehicle at which the buried object was detected was 2.9 m/s.

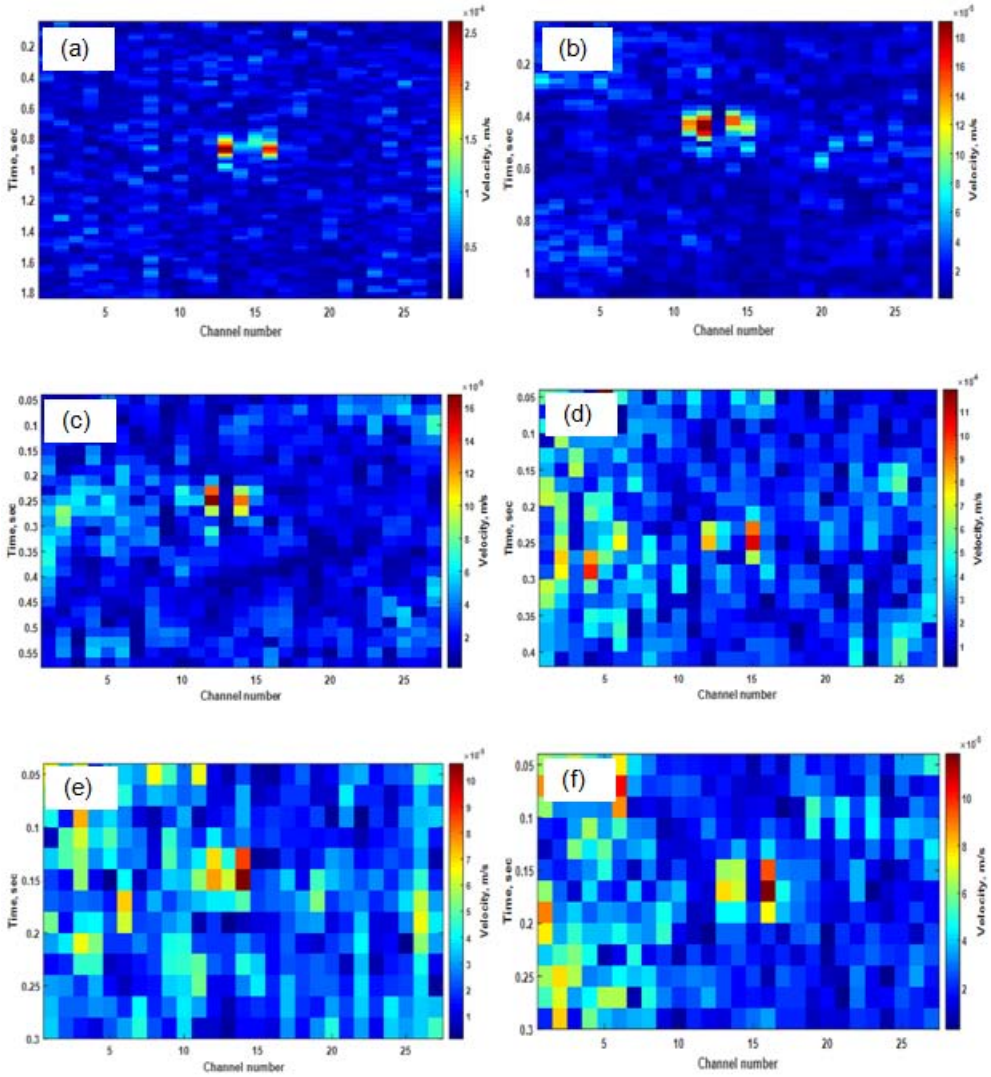

Figure 36. Vibration image of sand surface above the shaker obtained with the LMBDIS in a moving mode for 0.6 mm/s velocity of the sand surface above the shaker for different speeds of vehicle: (a) - 0.54 m/s, (b) - 0.87 m/s, (c) - 1.47 m/s, (d) - 2.2 m/s, (e) - 2.8 m/s, (f) - 2.9 m/s.

Figure 37 shows the vibration velocity image of the area measured with the LMBDIS in the moving mode for 0.3 mm/s velocity of the sand surface above the shaker. The measurements presented were done for two different speeds of vehicle: 0.59 m/s, and 1 m/s. The maximum speed of vehicle at which the buried object was detected was 1 m/s.

Figure 38 shows the vibration velocity image of the area measured with the LMBDIS in the moving mode for 0.15 mm/s velocity of the sand surface above the shaker. The maximum speed of vehicle at which the buried object was detected was 0.52 m/s.

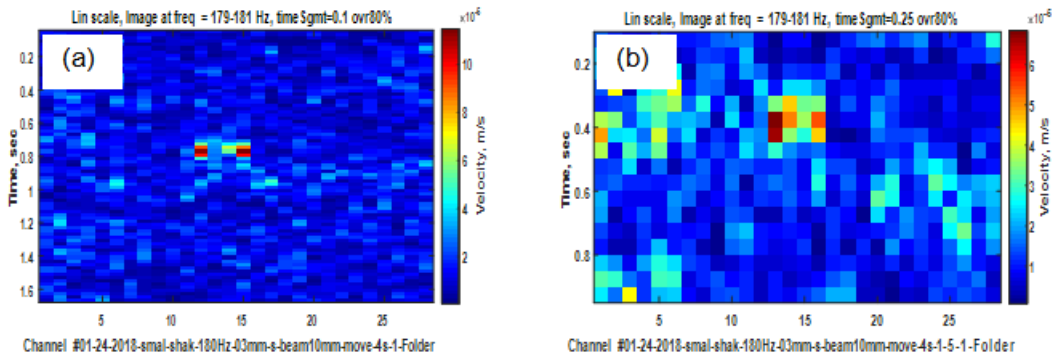

Figure 37. Vibration image of sand surface above the shaker obtained with the LMBDIS in a moving mode for 0.3 mm/s velocity of the sand surface above the shaker for different speeds of vehicle: (a) - 0.59 m/s, and (b) - 1 m/s.

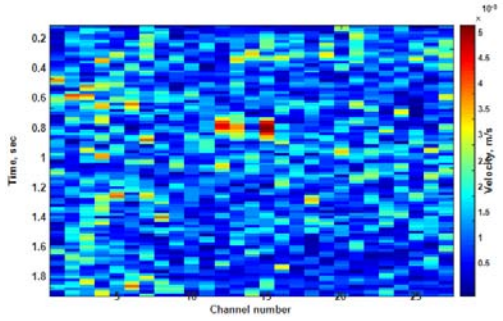

Figure 38 Vibration image of sand surface above the shaker obtained with the LMBDIS in a moving mode for 0.15 mm/s velocity of the sand surface above the shaker.

Figures 39 - 42 show the vibration velocity image of the area measured with the LMBDIS in the scanning mode. Figure 39 shows the vibration velocity image of the area measured with the LMBDIS in the scanning mode for 1.2 mm/s velocity of the sand surface above the shaker. The measurements were done for different speeds of scanning beams in the range from 1 m/s to 10 m/s. Figure 39 shows that the object was detected for each of the scanning speeds.

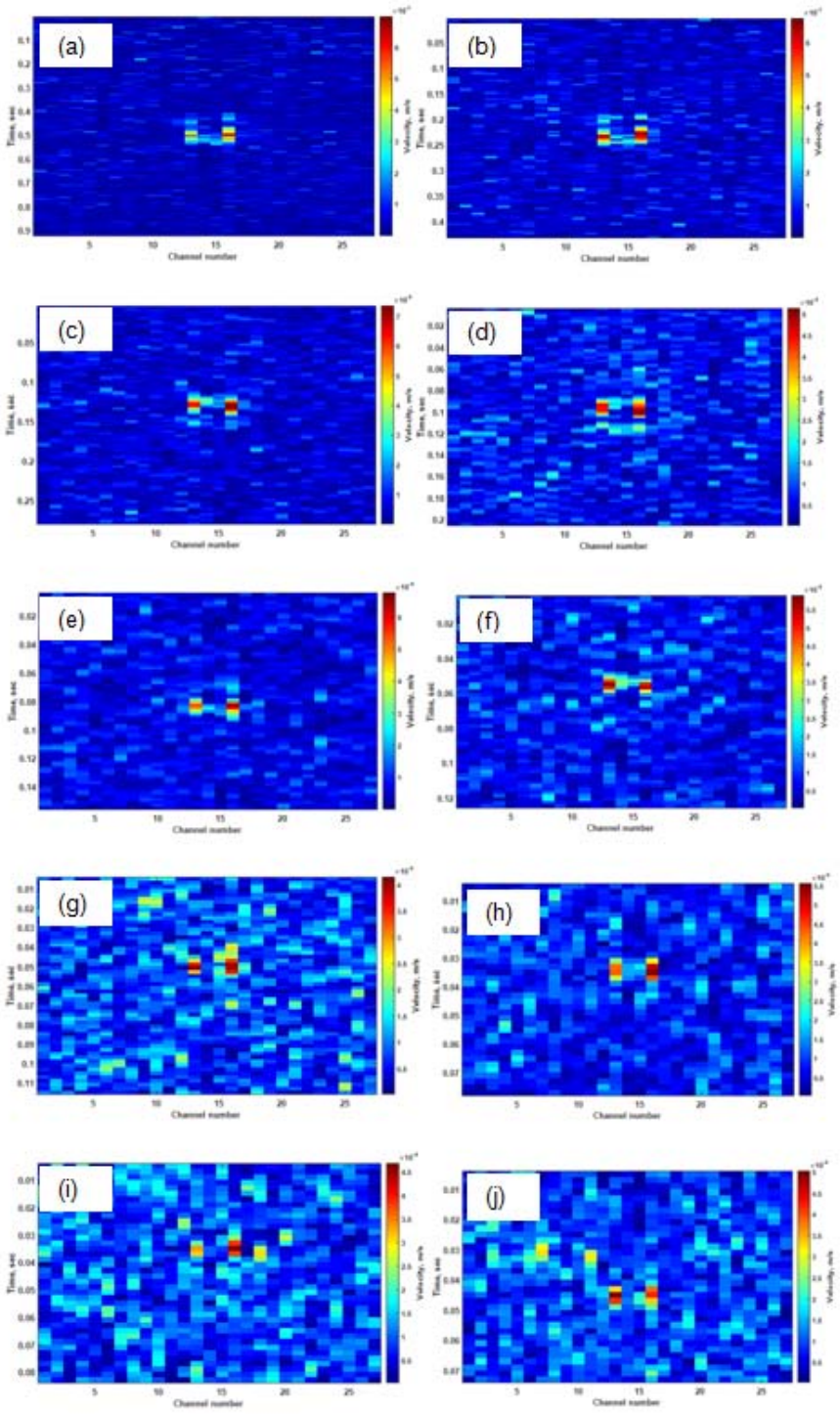

Figure 39. Vibration image of sand surface above the shaker obtained with the LMBDIS in a scanning mode for 1.2 mm/s velocity of the sand surface above the shaker for different speeds of beams: (a) - 1 m/s, (b) - 2 m/s, (c) - 3 m/s, (d) - 4 m/s, (e) - 5 m/s, (f) - 6 m/s, (g) - 7 m/s, (h) - 8 m/s, (i) - 9 m/s, (j) - 10 m/s.

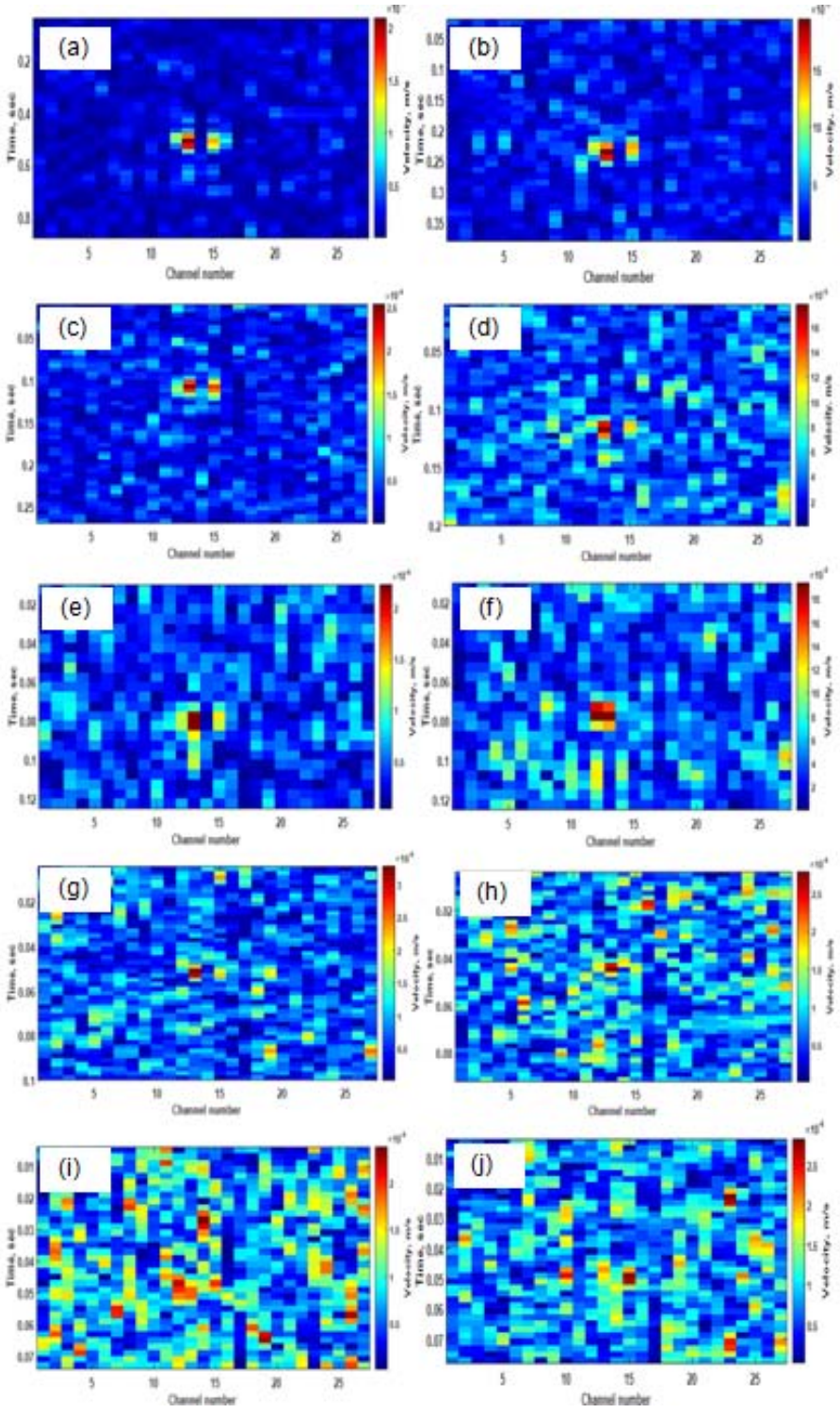

Figure 40. Vibration image of sand surface above the shaker obtained with the LMBDIS in a scanning mode for 0.6 mm/s velocity of the sand surface above the shaker for different speeds of beams: (a) - 1 m/s, (b) - 2 m/s, (c) - 3 m/s, (d) - 4 m/s, (e) - 5 m/s, (f) - 6 m/s, (g) - 7 m/s, (h) - 8 m/s, (i) - 9 m/s, (j) - 10 m/s.

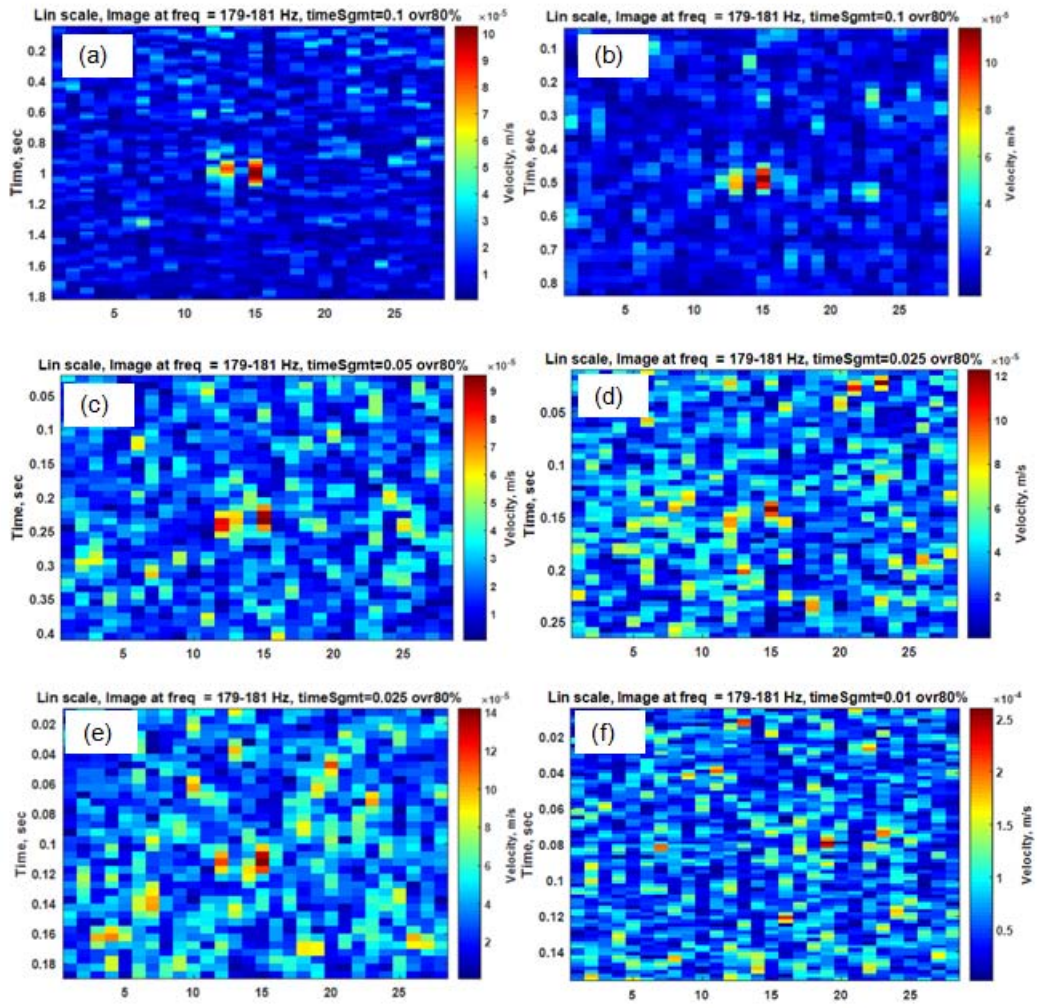

Figure 41. Vibration image of sand surface above the shaker obtained with the LMBDIS in a scanning mode for 0.3 mm/s velocity of the sand surface above the shaker for different speeds of beams: (a) - 1 m/s, (b) - 2 m/s, (c) - 3 m/s, (d) - 4 m/s, (e) - 5 m/s, (f) - 6 m/s.

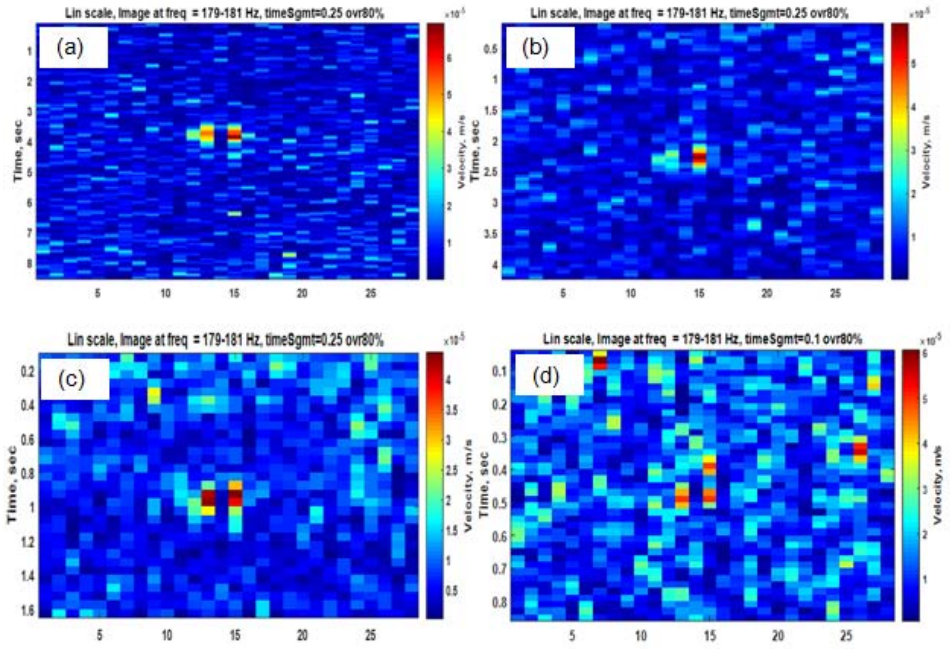

Figure 42. Vibration image of sand surface above the shaker obtained with the LMBDIS in a scanning mode for 0.15 mm/s velocity of the sand surface above the shaker for different speeds of beams: (a) - 0.1 m/s, (b) - 0.2 m/s, (c) - 0.5 m/s, and (d) - 1 m/s.

The major results on performance of LMBDIS for different speeds of scanning and moving beams are summarized in Table 1, which shows the maximum speed of beams for which the buried shaker has been detected. For example, for vibration velocity above the center of the shaker of 0.3 mm/s, the shaker was detected with the 4 m/s maximum speed of beams in the scanning mode and with 1 m/s speed of beams in the moving mode.

Table 1. Performance of LMBDIS for different speed of scanning and moving beams

Vibration velocity magnitude above the center of shaker, mm/s	1.2	0.6	0.3	0.15
Maximum speed of scanning at which object was detected, m/s	10	7	5	1
Maximum speed of moving at which object was detected, m/s	3.8	2.9	1	0.5

12 Field experiments

Field experiments were performed at the AUX4 site at Eglin AFB from September 9 to September 20, 2018. A layout of the site is shown in Figure 43. Objects were buried at 20

locations along a line. Objects included AT mines, plastic 5 gallon gasoline jugs, metal oil cans, and a plastic box of 36" x 32' x 6" dimensions. Objects were buried at different depths according to the layout in Figure 43. A circular mechanical shaker (model TST329, Clark Synthesis, Inc.)[20] buried at the beginning of the line was used as a vibration source with known amplitude to verify performance of the LMBDIS. The high frequency wheel station (HFWS was) placed at 10 m down the track from a measured target. The LMBDIS was driven on plywood tracks which provided smooth motion of the electric vehicle.

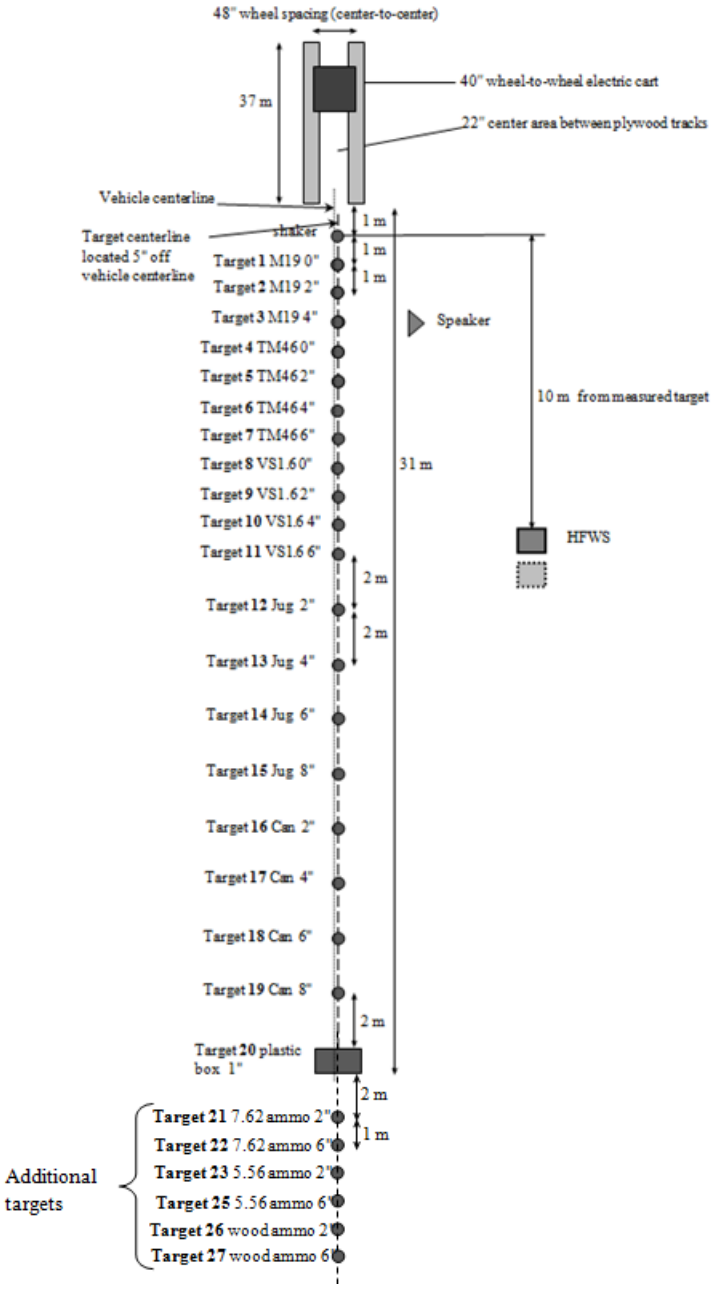

Figure 43. Layout of the field experiments site

The LMBDIS was mounted on a small Taylor-Dunn electric vehicle in order to conduct field experiments. A photograph of the LMBDIS mounted on the electric vehicle is shown in Figure 44. The LMBDIS optical head is mounted on the front of the vehicle and the supporting electronics, which includes a data acquisition computer and a power supply, is mounted in a 19-inch rack on the back of the vehicle. A lifting mechanism allows adjustment of the height of the optical head from 1.50 m to 2.4 m measured at the scanning mirror.

The concept of using the LMBDIS for acoustic detection of buried objects is illustrated by Figure 44. A linear array of 30 beams from the LMBDIS output is horizontal, directed to the ground surface at an angle which depends on the standoff distance S. For example, for a height of beams of 2.4 m above the ground and a 10 m standoff distance, the grazing angle of beams was 13.5°. Given the full angle of beam pattern of Θ = 5.9° and the inter-beam angle of 0.203°, the spread of beams D on the ground is D = 103 cm and the distance between the neighboring beams is d=3.6 cm at a 10 m standoff distance; for 20 m distance, D = 206 cm, d = 7.2 cm; for 40 m distance, D = 412 cm, d = 14.4 cm. The number of informative channels N_S (channels producing heterodyne signals) depends on the total number of beams N_B and the number of inter-beam intervals N_{INT} by which one image is sheared relative to another.

$$N_S = N_B - N_{INT} \tag{15}$$

For example, for the shear equal to one interval between neighboring laser spots, the number of channels is 29; for the shear equal to three intervals between neighboring laser spots in the image plane, the number of channels is 27.

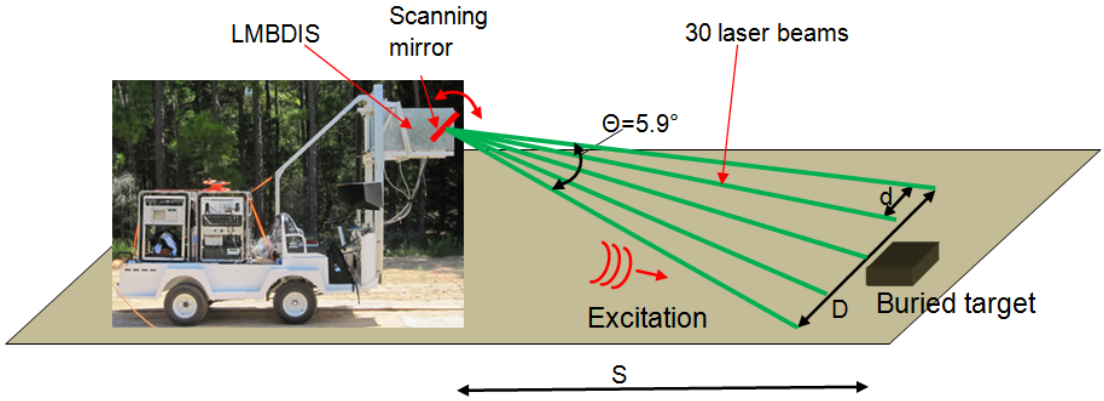

Figure 44. Concept of using LMBDIS for acoustic detection of buried objects.

For the field experiments, the LMBDIS alignment was made in such a way that two images of the laser spots on the PDA were sheared relative each other by three intervals between neighboring laser spots in the image plane. As a result, LMBDIS measured relative velocities between points of the object separated by three intervals between the points: channel 1 provided relative velocity between points 1 and 4, channel 2 - between points 2 and 5, and so on. With 30 beams on the object, there were 27 measurement signals. The measurements were conducted in two modes of operation:

1. Moving mode. Beams scan the ground due to the vehicle motion. The sensor is moving forward and the scanning mirror is stationary. The scanning mirror angle defines the standoff distance.
2. Scanning mode. The sensor/vehicle is stationary. Initial angle of the scanning mirror defines the standoff distance. The scanning mirror scans the beams along the track by a predetermined distance, for example one meter. The speed of scanning and a scanning distance can be selected by the operator.

12.1 Vibration imaging of buried objects from a moving vehicle

Performance of the LMBDIS in a moving mode was evaluated by measuring buried objects at different speeds of the vehicle. The speed of the vehicle was controlled by using a simple speed limiting device installed on the vehicle, which allowed moving the vehicle at a selected constant speed. For the precise estimation of the speed of beams over the measured area, two metal bars, used as markers, were placed on the ground in front and behind the measured object across the track at a known distance between the bars. Due to the high reflectivity of the metal bars, two sharp spikes were formed in the photodetector signals when laser beams passed over the markers. The speed of beams over the measured area was determined by calculating the ratio of the distance between the markers to the time between the spikes in the signal. Figure 45 shows an example of the photodetector signal of one of the channels (channel 9) that contains two spikes due to laser beams passing over the markers, and a vibration image of a buried object positioned between the markers. In the example, the distance between the two markers was 1 m, and the time separation between the two spikes was 1.19 s. This gives the speed of moving beams at approximately 0.84 m/s.

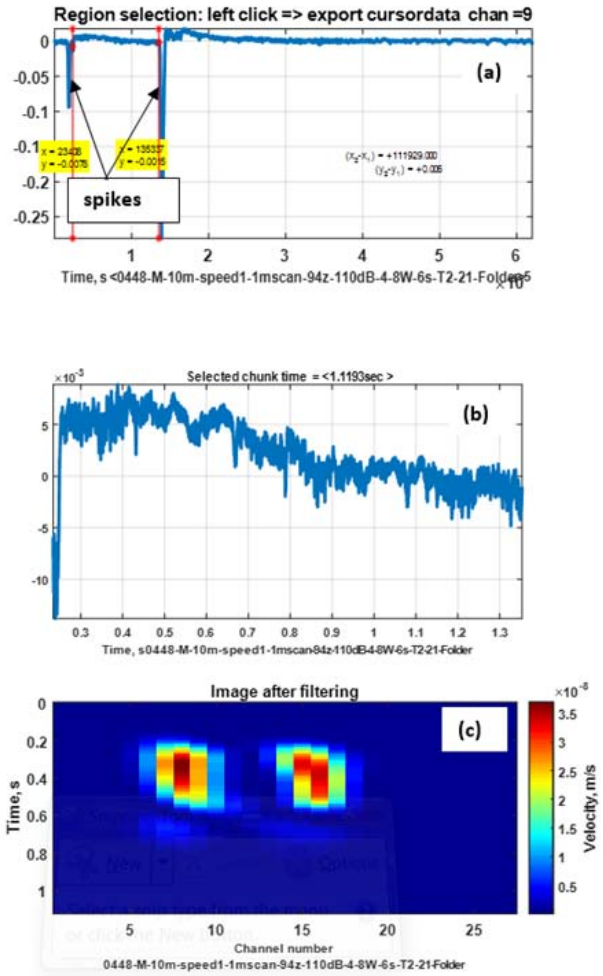

Figure 45. Photodetector signal (a) of LMBDIS channel 9 that has two spikes caused by laser beams passing over the markers, (b) time segment of 1.12 seconds duration between two markers (b), and a vibration image (c) of a buried object positioned between the markers.

Measurements in a moving mode were completed for selected objects, whose frequency response was characterized earlier using geophones. The objects were measured at distances of 10 m and 20 m. Measurements in a moving mode at 40 m distance were not doable, because beams were missing objects due to a small unevenness of the plywood tracks on which the electric vehicle was driven. Excitation was provided by a speaker and the HFWS for measurements at 10 m distance, and only by a speaker for measurements at 20 m distance. In measurements with a speaker, the speaker was located about 2 m from the measured object. The HFWS was located at 10 m from a measured target. Table 2 shows a list of measured objects for the moving mode, the excitation source used, the frequency of excitation, and the distance to the object for each measurement. It also shows if the object was detected or not detected by using symbols "Y" for detected, and "N" for not detected. Symbol "N/A" shows that the object was not measured. Figures 46 - 54 show vibration images of detected targets from a moving vehicle at 10

m standoff distance using a speaker as an excitation source. The SPL level for speaker excitation was in the range from 107 dB to 110 dB.

Vibration images of buried targets were made with application of a filtering algorithm developed by Dr. Brian Lidmark of NSWC PCD. The algorithm improves the signal-to-noise ratio and enhances contrast of vibration images. Application of the algorithm reduces the velocity values in the vibration image.

Table 2. Accomplished measurements for the moving mode. Y - detected, N - not detected, N/A - not measured

Target position	Target type	Depth	Distance 10 m		Distance 20 m	
			Speaker	HFWS	Speaker	HFWS
Target1	M19	0”	N/A	N/A	N/A	N/A
Target2	M19	2”	Y, 94 Hz	Y, 94 Hz	Y, 94 Hz	N/A
Target3	M19	4”	Y, 103 Hz	Y, 94 Hz	Y, 103 Hz	N/A
Target4	TM46	0”	N/A	N/A	N/A	N/A
Target5	TM46	2”	Y, 115 Hz	N, 94 Hz	Y, 115 Hz	N/A
Target6	TM46	4”	Y, 115 Hz	Y, 94 Hz	Y, 115 Hz	N/A
Target7	TM46	6”	Y, 115 Hz	Y, 94 Hz	Y, 115 Hz	N/A
Target8	VS1.6	0”	N/A	N/A	N/A	N/A
Target9	VS1.6	2”	N/A	Y, 120 Hz	N/A	N/A
Target10	VS1.6	4”	N/A	Y, 150 Hz	Y, 120 Hz	N/A
Target11	VS1.6	6”	N/A	Y, 150 Hz	N	N/A
Target12	Jug	2”	Y, 79 Hz	Y, 80 Hz	Y, 80 Hz	N/A
Target13	Jug	4”	Y, 79 Hz	Y, 90 Hz	Y, 83 Hz	N/A
Target14	Jug	6”	N/A	Y, 110 Hz	Y, 84 Hz	N/A
Target15	Jug	8”	N/A	Y, 65 Hz	N	N/A
Target16	Can	2”	Y, 80 Hz	Y, 80 Hz	Y, 73 Hz	N/A
Target17	Can	4”	Y, 86 Hz	Y, 86 Hz	Y, 86 Hz	N/A
Target18	Can	6”	Y, 89 Hz	Y, 89 Hz	Y, 89 Hz	N/A
Target19	Can	8”	Y, 94 Hz	Y, 80 Hz	Y, 94 Hz	N/A

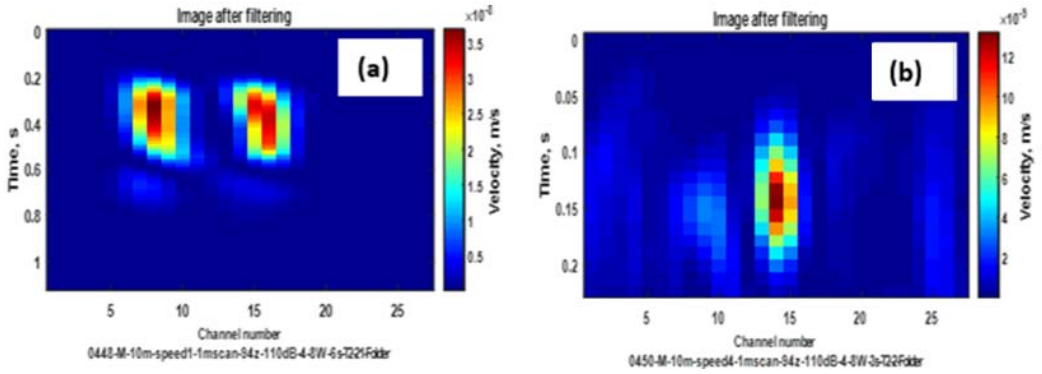

Figure 46. Vibration image of target 2 obtained in a moving mode at 10 m distance for different speeds of vehicle: (a) - 0.9 m/s (2 mph); (b) - 4.5 m/s (10 mph). Excitation at 94 Hz frequency was provided by a speaker.

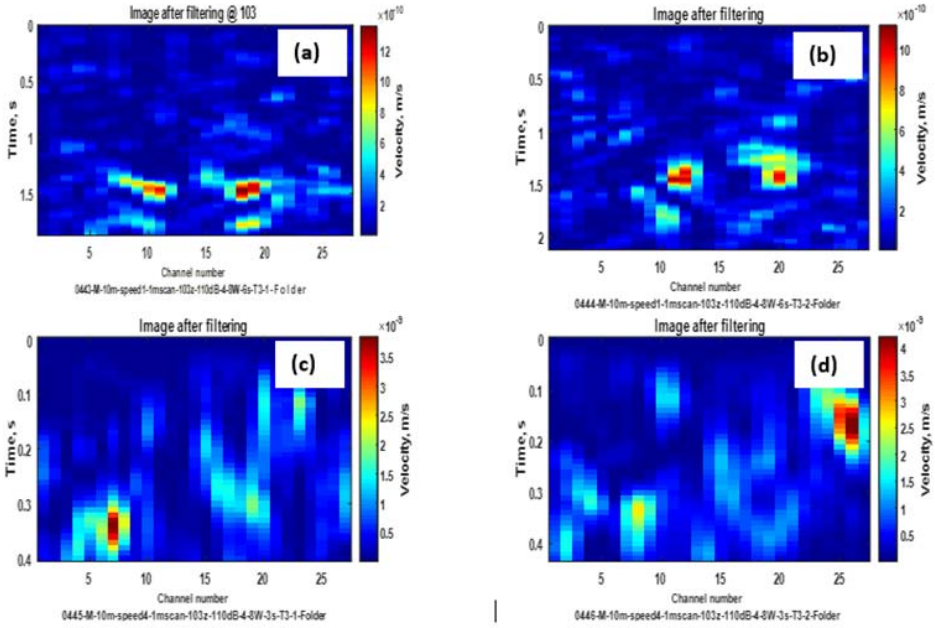

Figure 47. Vibration image of target 3 obtained in a moving mode at 10 m distance for different speeds of vehicle: (a) - 0.53 m/s (1.2 mph); (b) - 0.47 m/s (1 mph), (c) - 2.5 m/s (5.6 mph), (d) - 2.3 m/s (5.1 mph). Excitation at 103 Hz frequency was provided by a speaker.

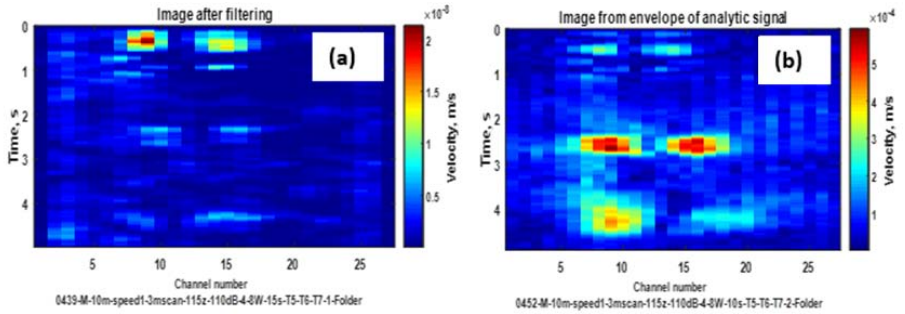

Figure 48. Vibration image of targets 5, 6, and 7 obtained in a moving mode at 10 m distance for different speeds of vehicle: (a) - 0.6 m/s (1.3 mph) , (b) - 0.56 m/s (1.25 mph). Excitation at 115 Hz frequency was provided by a speaker.

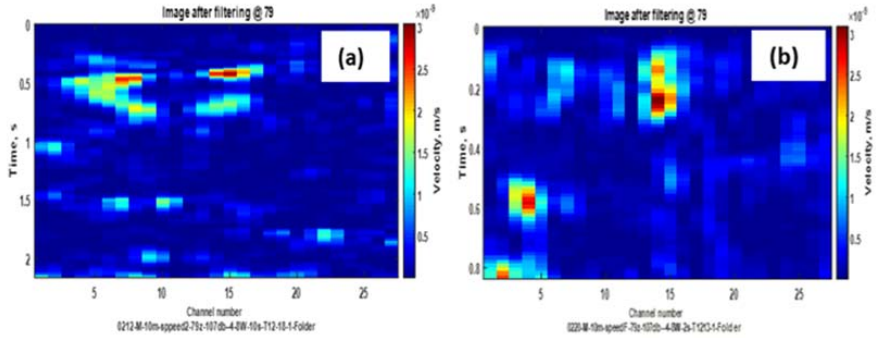

Figure 49. Vibration image of targets 12 and 13 obtained in a moving mode at 10 m distance for different speeds of vehicle: (a) - 1.4 m/s (3.1 mph) , (b) - 3.6 m/s (8 mph). Excitation at 79 Hz frequency was provided by a speaker.

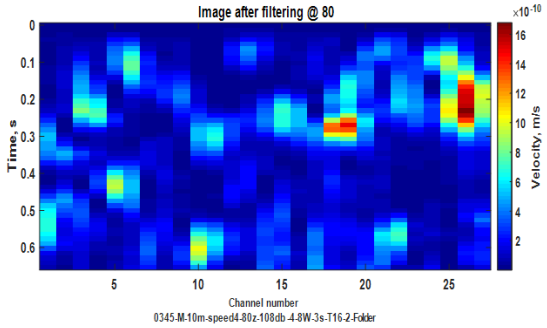

Figure 50. Vibration image of target 16 obtained in a moving mode at 10 m distance for speed of vehicle 3.0 m/s (6.7 mph). Excitation at 80 Hz frequency was provided by a speaker.

Figure 51 shows a vibration image of targets 17 and 18 excited with a speaker at 79 Hz frequency obtained in a moving mode at 10 m distance for a speed of vehicle: (a) - 2.9 m/s (6.5 mph) , (b) - 3.6 m/s (8 mph). Only object 17 is clearly seen on the image. However, when measured separately with excitation at a frequency of the maximum frequency response, 86 Hz for target 17 and 89 Hz for target 18, both targets provide high contrast vibration images, as shown in Figures 52 and 53.

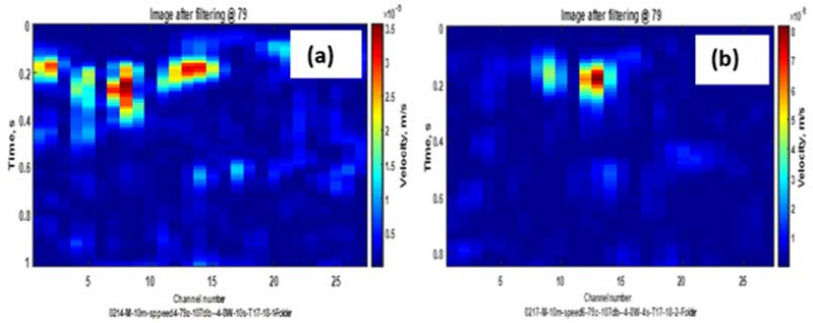

Figure 51. Vibration image of targets 17 and 18 obtained in a moving mode at 10 m distance for different speeds of vehicle: (a) - 2.9 m/s (6.5 mph) , (b) - 3.6 m/s (8 mph). Excitation at 79 Hz frequency was provided by a speaker.

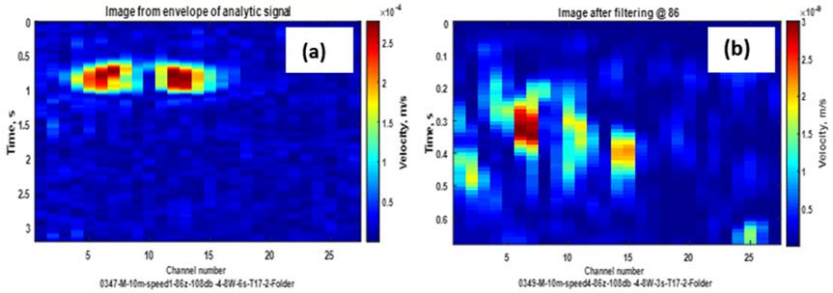

Figure 52. Vibration image of target 17 obtained in a moving mode at 10 m distance for different speeds of vehicle: 0.63 m/s (1.4 mph) , (b) - 3 m/s (6.7 mph). Excitation at 86 Hz frequency was provided by a speaker.

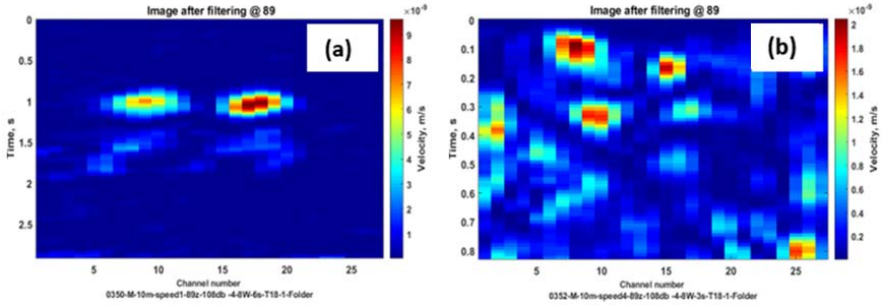

Figure 53. Vibration image of target 18 obtained in a moving mode at 10 m distance for different speeds of vehicle: (a) - 0.69 m/s (1.5 mph) , (b) - 2.4 m/s (5.4 mph). Excitation at 89 Hz frequency was provided by a speaker.

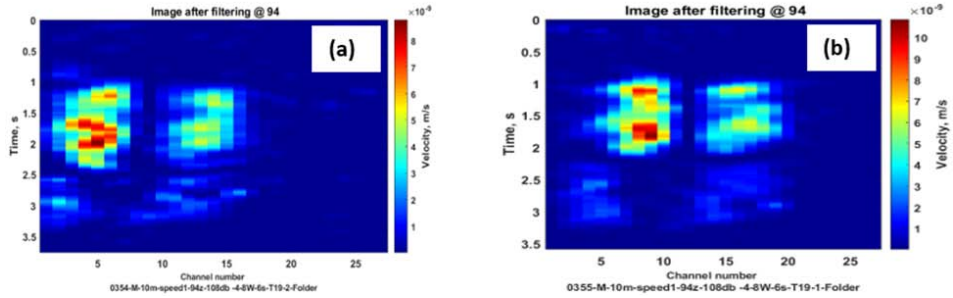

Figure 54. Vibration image of target 19 obtained in a moving mode at 10 m distance for different speeds of vehicle: (a) - 0.53 m/s (1.19 mph) , (b) - 0.55 m/s (1.23 mph). Excitation at 94 Hz frequency was provided by a speaker.

Figures 55 - 67 show vibration images of buried objects measured from a moving vehicle for 10 m standoff distance using the HFWS for excitation.

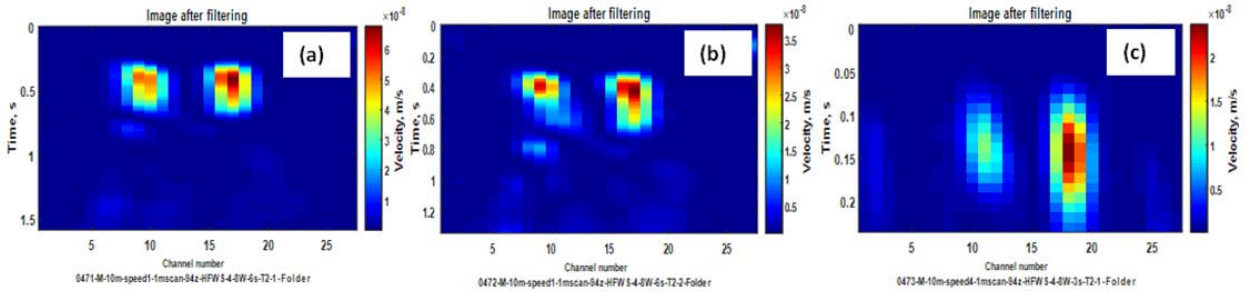

Figure 55. Vibration image of target 2 obtained in a moving mode at 10 m distance for different speeds of vehicle: (a) - 0.63 m/s (1.4 mph) , (b) - 0.75 m/s (1.7 mph), (c) - 4.35 m/s (9.7 mph). Excitation at 94 Hz frequency was provided by HFWS

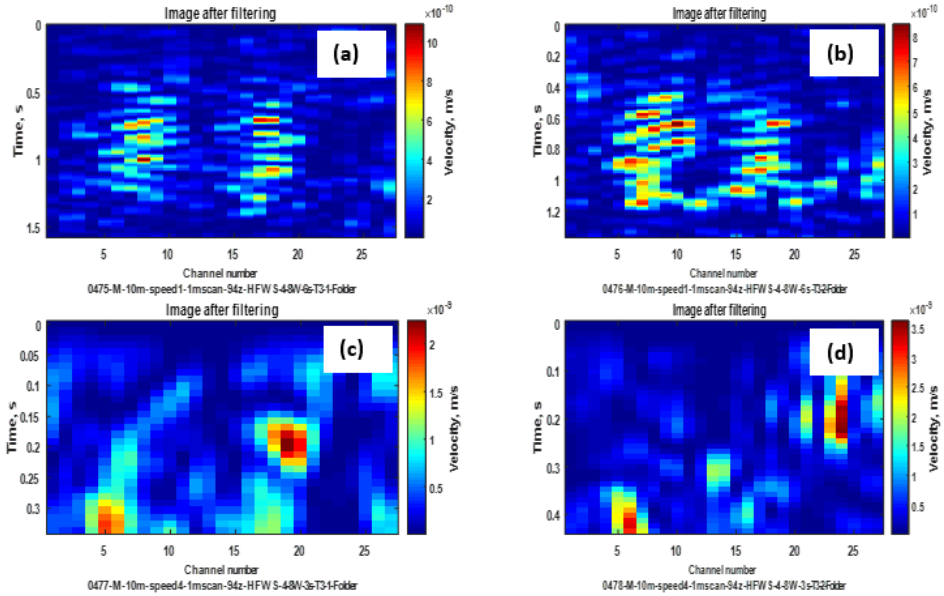

Figure 56. Vibration image of target 3 obtained in a moving mode at 10 m distance for different speeds of vehicle: (a) - 0.63 m/s (1.4 mph) , (b) - 0.73 m/s (1.6 mph), (c) - 2.8 m/s (6.3 mph), (d) - 2.3 m/s (5.1 mph). Excitation at 94 Hz frequency was provided by HFWS

Targets 5, 6, and 7 were measured in one move with 94 Hz frequency excitation. As one can see from Figure 57, target 5 is not seen on the image, and target 6 shows a weak contrast. It is probably caused by weak response of those targets, and also high contrast of the target 7 image could mask images of targets 5 and 6.

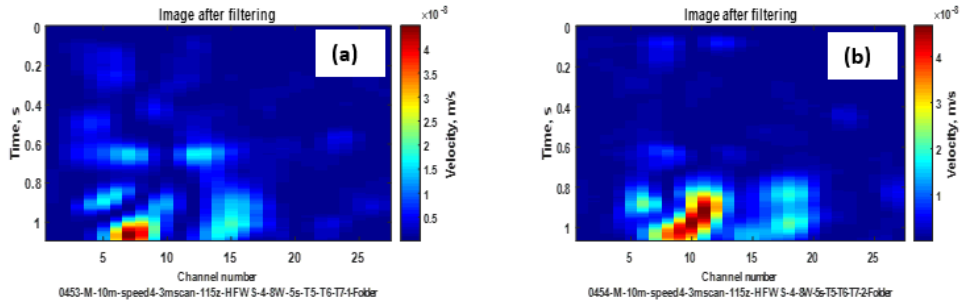

Figure 57. Vibration image of targets 5,6, and 7 obtained in a moving mode at 10 m distance for different speeds of vehicle: (a) - 2.75 m/s (6.1 mph) , (b) - 2.82 m/s (6.3 mph). Excitation at 94 Hz frequency was provided by HFWS.

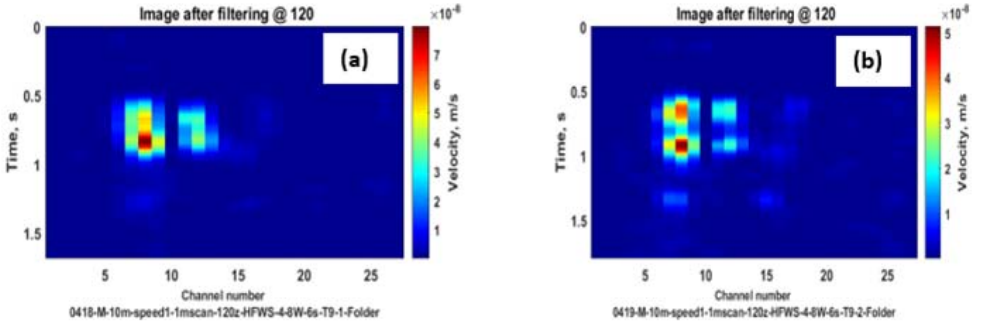

Figure 58. Vibration image of target 9 obtained in a moving mode at 10 m distance for different speeds of vehicle: (a) - 0.59 m/s (1.3 mph) , (b) - 0.56 m/s (1.25 mph). Excitation at 120 Hz frequency was provided by HFWS.

Targets 10 and 11 were measured in one move with 150 Hz frequency excitation. As one can see from Figure 57, target 11 has weak contrast, which is probably higher contrast of target 10 image.

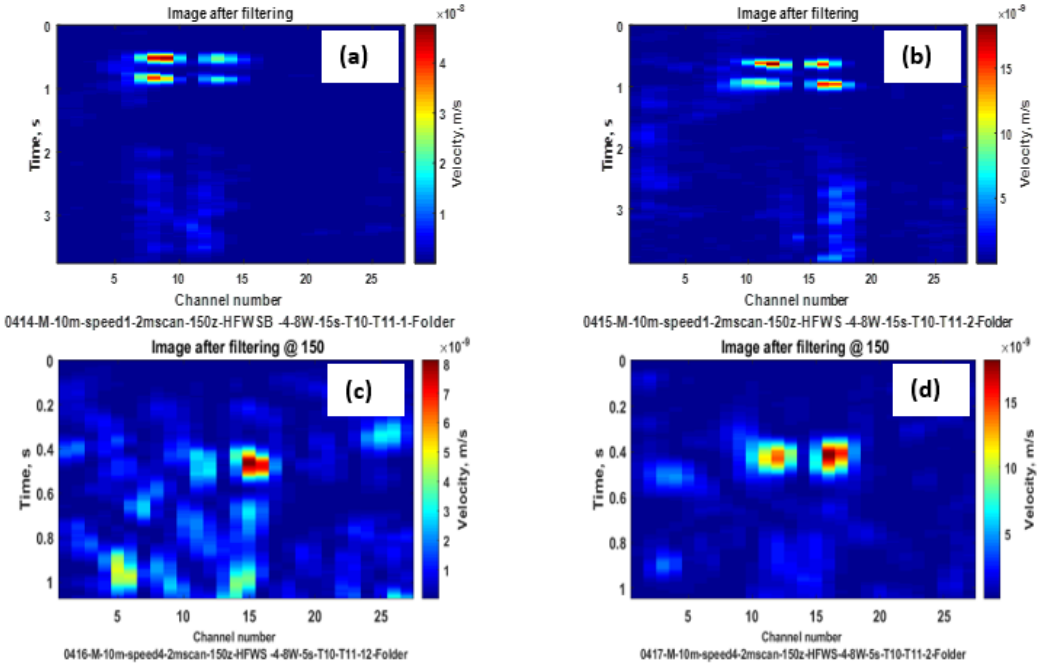

Figure 59. Vibration image of targets 10 and 11 obtained in a moving mode at 10 m distance for different speeds of vehicle: (a) - 0.51 m/s (1.1 mph) , (b) - 0.50 m/s (1.1 mph), (c) - 1.87 m/s (4.2 mph) , (d) - 1.92 m/s (4.3 mph). Excitation at 150 Hz frequency was provided by HFWS.

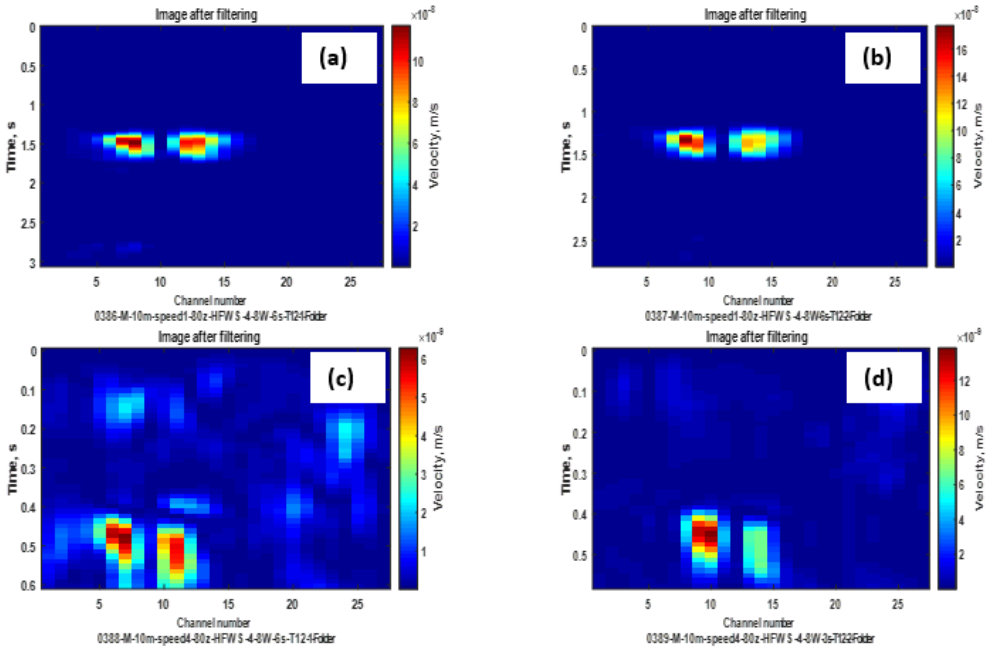

Figure 60. Vibration image of target 12 obtained in a moving mode at 10 m distance for different speeds of vehicle: (a) - 0.65 m/s (1.45 mph) , (b) - 0.71 m/s (1.59 mph), (c) - 3.33 m/s (7.4 mph) , (d) - 3.46 m/s (7.7 mph). Excitation at 80 Hz frequency was provided by HFWS.

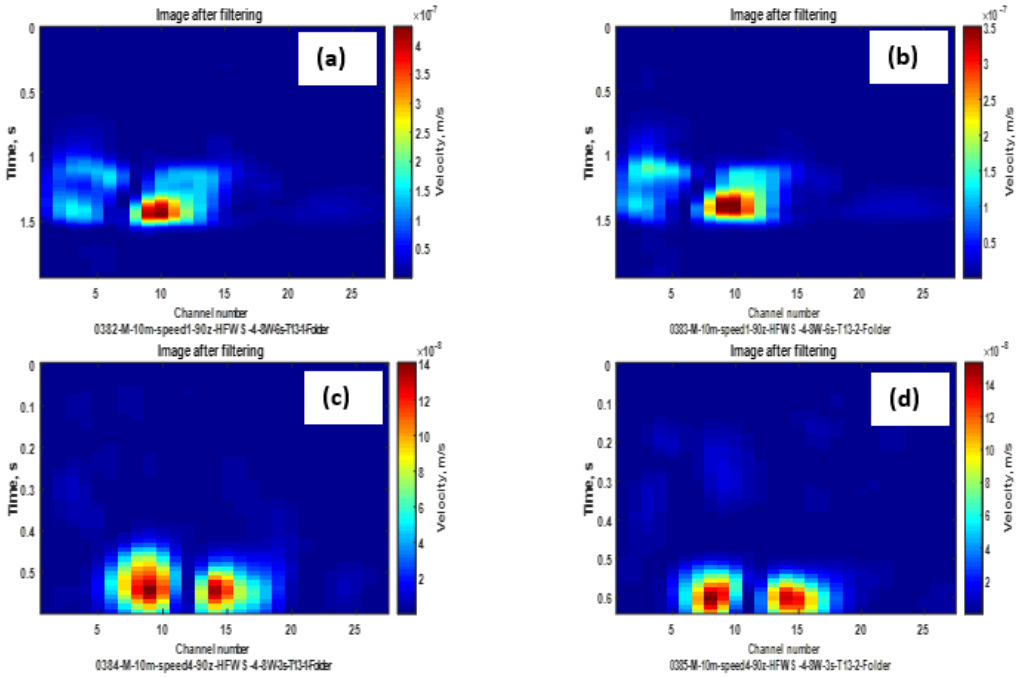

Figure 61. Vibration image of target 13 obtained in a moving mode at 10 m distance for different speeds of vehicle: (a) - 1.04 m/s (2.3 mph) , (b) - 1.03 m/s (2.3 mph), (c) - 3.39 m/s (7.6 mph) , (d) - 3.14 m/s (7.0 mph). Excitation at 90 Hz frequency was provided by HFWS.

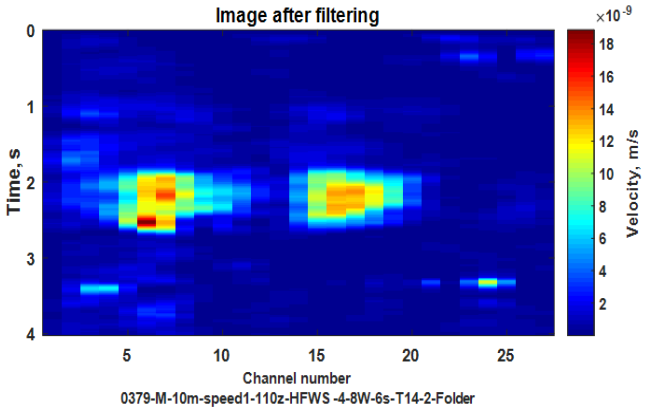

Figure 62. Vibration image of target 14 obtained in a moving mode at 10 m distance for speed of vehicle 0.5 m/s (1.1 mph). Excitation at 110 Hz frequency was provided by HFWS.

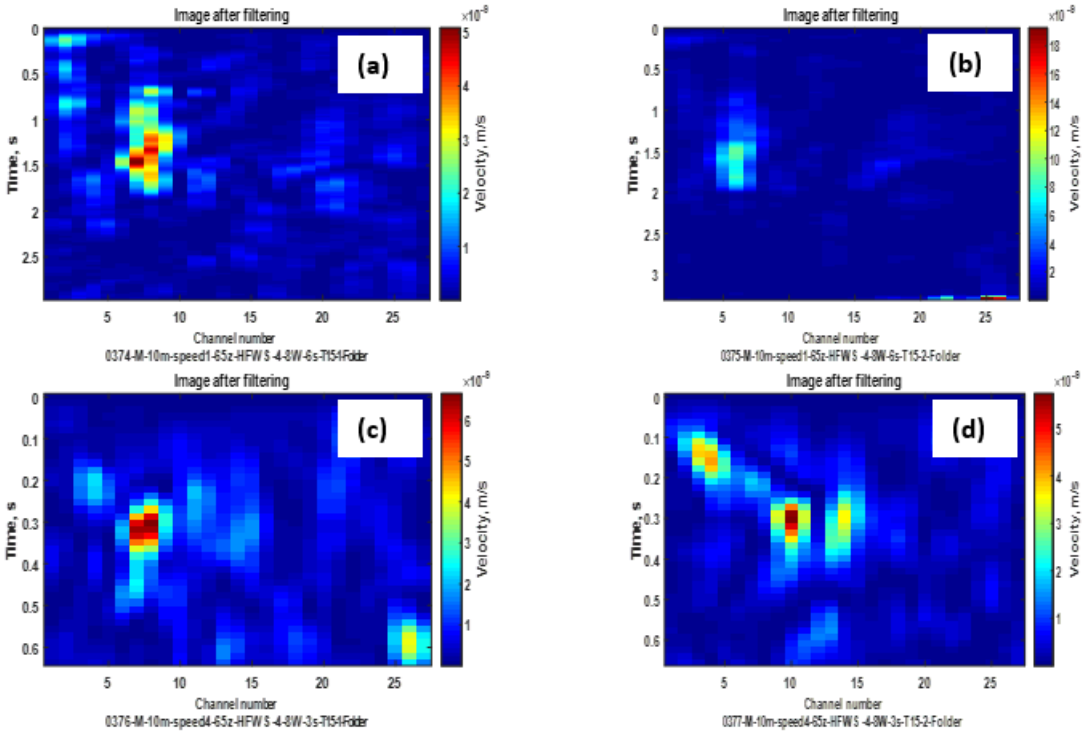

Figure 63. Vibration image of target 15 obtained in a moving mode at 10 m distance for different speeds of vehicle: (a) - 0.68 m/s (1.5 mph) , (b) - 0.6 m/s (1.3 mph), (c) - 3.14 m/s (7.0 mph) , (d) - 3.05 m/s (6.8 mph). Excitation at 65 Hz frequency was provided by HFWS.

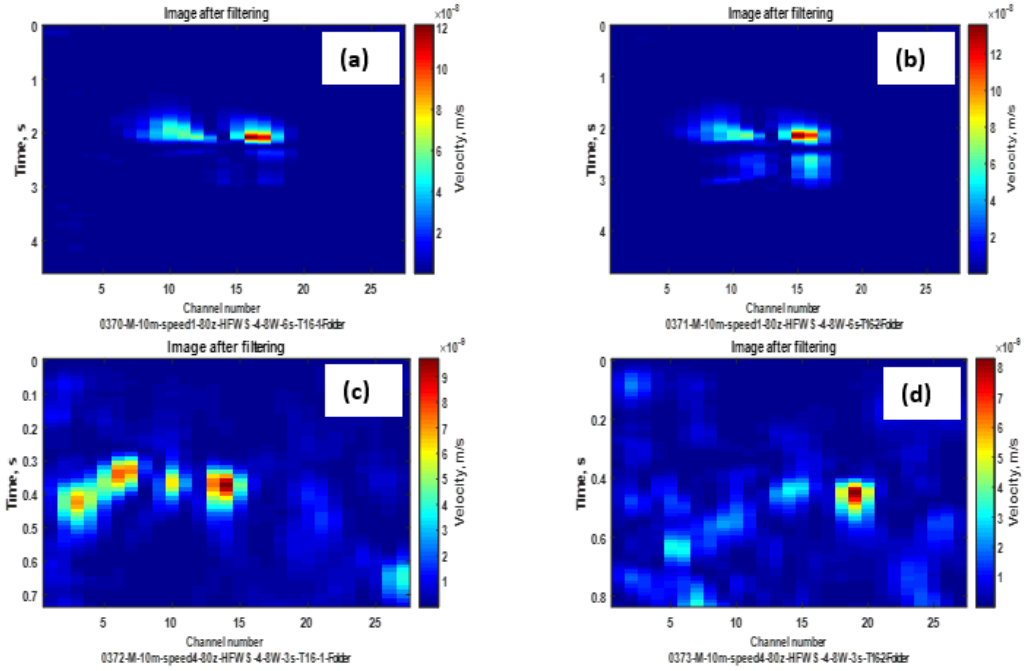

Figure 64. Vibration image of target 16 obtained in a moving mode at 10 m distance for different speeds of vehicle: (a) - 0.43 m/s (0.96 mph) , (b) - 0.41 m/s (0.91 mph), (c) - 2.74 m/s (6.1 mph) , (d) - 2.41 m/s (5.4 mph). Excitation at 80 Hz frequency was provided by HFWS.

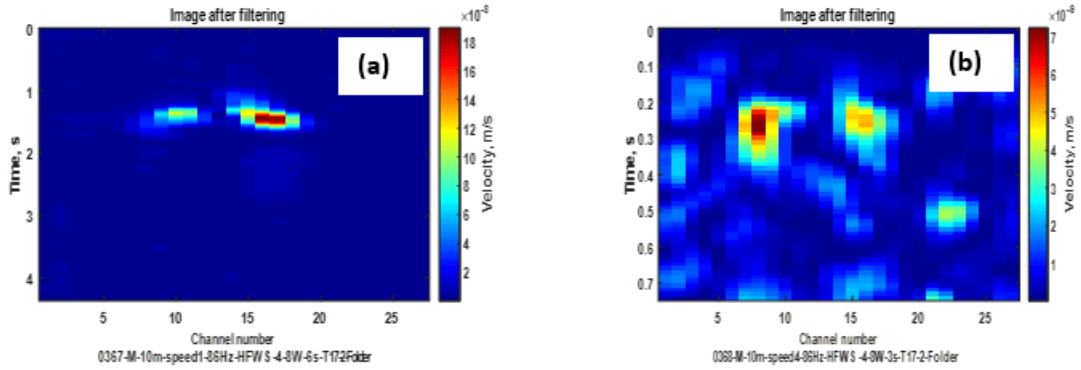

Figure 65. Vibration image of target 17 obtained in a moving mode at 10 m distance for different speeds of vehicle: (a) - 0.46 m/s (1.03 mph) , (b) - 2.69 m/s (6.0 mph). Excitation at 86 Hz frequency was provided by HFWS.

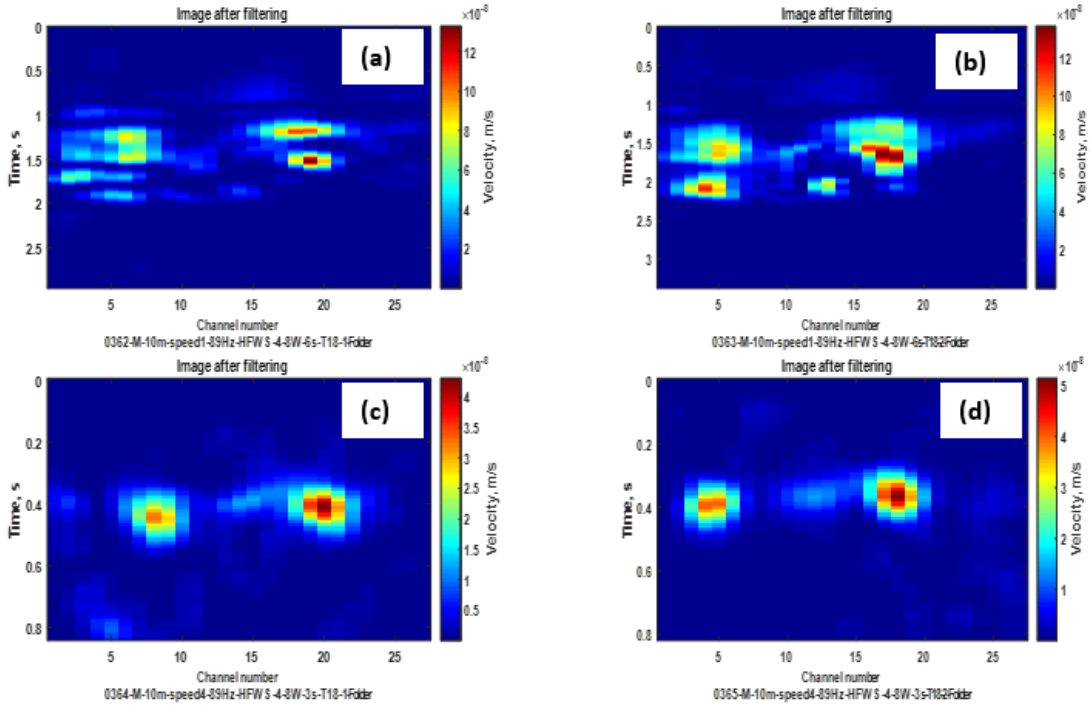

Figure 66. Vibration image of target 18 obtained in a moving mode at 10 m distance for different speeds of vehicle: (a) - 0.68 m/s (1.5 mph) , (b) - 0.59 m/s (1.3 mph), (c) - 2.39 m/s (5.3 mph) , (d) - 2.47 m/s (5.5 mph). Excitation at 89 Hz frequency was provided by HFWS.

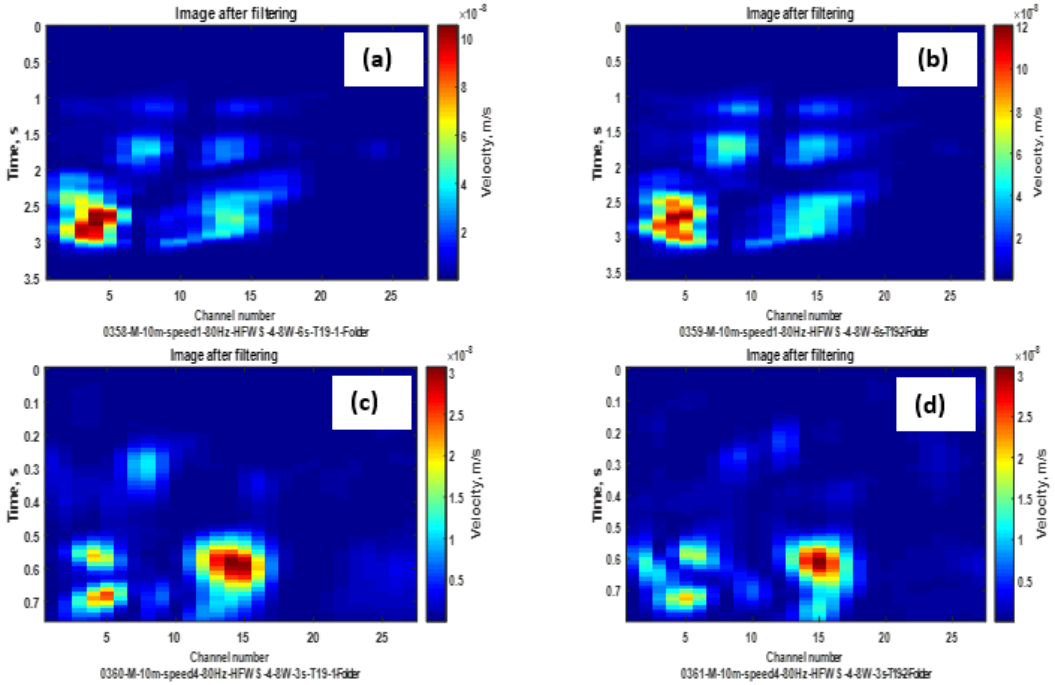

Figure 67. Vibration image of target 19 obtained in a moving mode at 10 m distance for different speeds of vehicle: (a) - 0.57 m/s (1.27 mph) , (b) - 0.55 m/s (1.23 mph), (c) - 2.65 m/s (5.9 mph) , (d) - 2.52 m/s (5.6 mph). Excitation at 80 Hz frequency was provided by HFWS.

Figures 68 - 78 show vibration images of buried objects measured from a moving vehicle for 20 m standoff distance using a speaker for excitation.

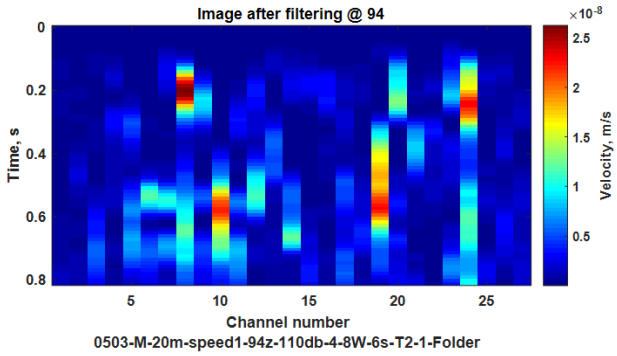

Figure 68. Vibration image of target 2 obtained in a moving mode at 20 m distance for speed of vehicle 1.25 m/s (2.8 mph). Excitation at 94 Hz frequency was provided by a speaker.

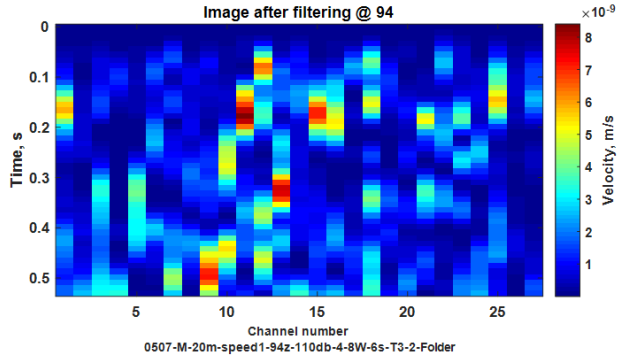

Figure 69. Vibration image of target 3 obtained in a moving mode at 20 m distance for speed of vehicle 1.89 m/s (4.2 mph). Excitation at 94 Hz frequency was provided by a speaker.

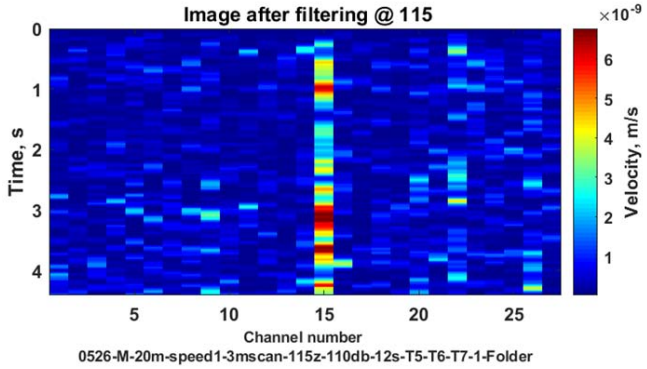

Figure 70. Vibration image of targets 5, 6, and 7 obtained in a moving mode at 20 m distance for speed of vehicle 0.68 m/s (1.5 mph). Excitation at 115 Hz frequency was provided by a speaker.

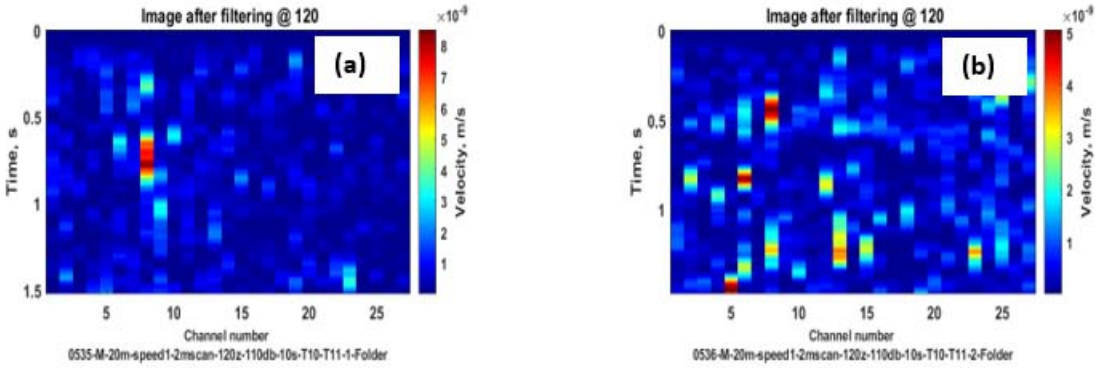

Figure 71. Vibration image of targets 10 and 11 obtained in a moving mode at 20 m distance for different speeds of vehicle: (a) - 1.32 m/s (2.95 mph), (b) - 1.37 m/s (3.0 mph). Excitation at 120 Hz frequency was provided by a speaker.

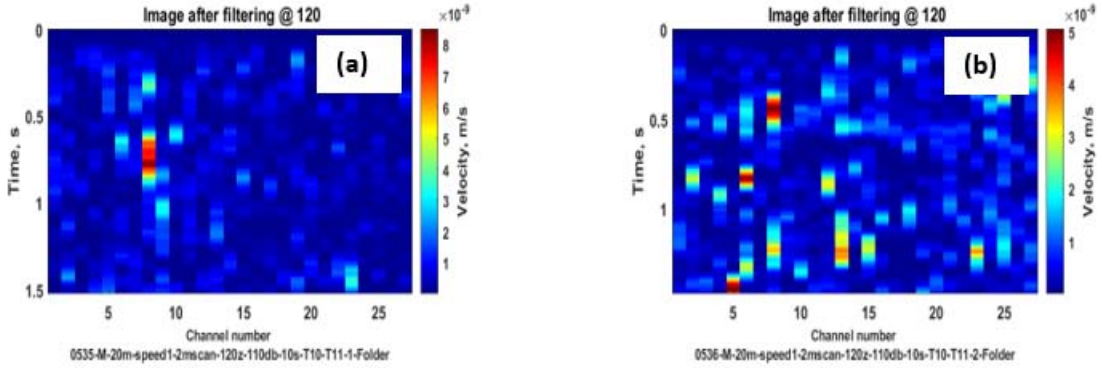

Figure 72. Vibration image of target 12 obtained in a moving mode at 20 m distance for different speeds of vehicle: (a) - 0.65 m/s (1.45 mph), (b) - 0.54 m/s (1.2 mph). Excitation at 80 Hz frequency was provided by a speaker.

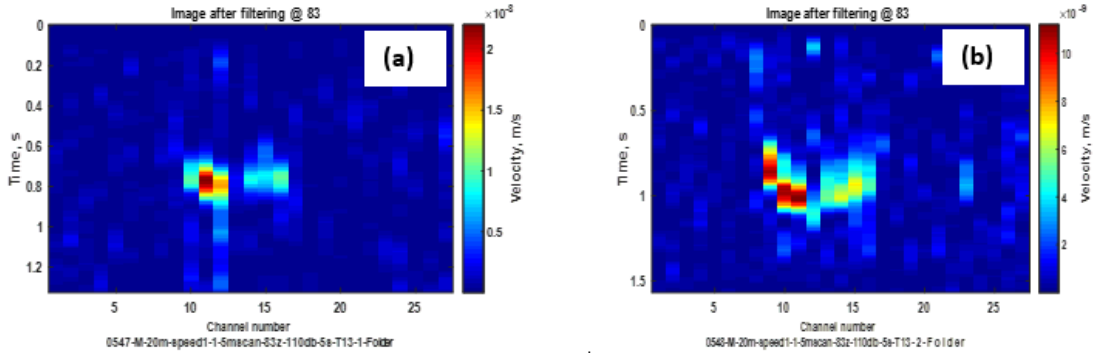

Figure 73. Vibration image of target 13 obtained in a moving mode at 20 m distance for different speeds of vehicle: (a) - 1.13 m/s (2.5 mph), (b) - 0.9 m/s (2.0 mph). Excitation at 83 Hz frequency was provided by a speaker.

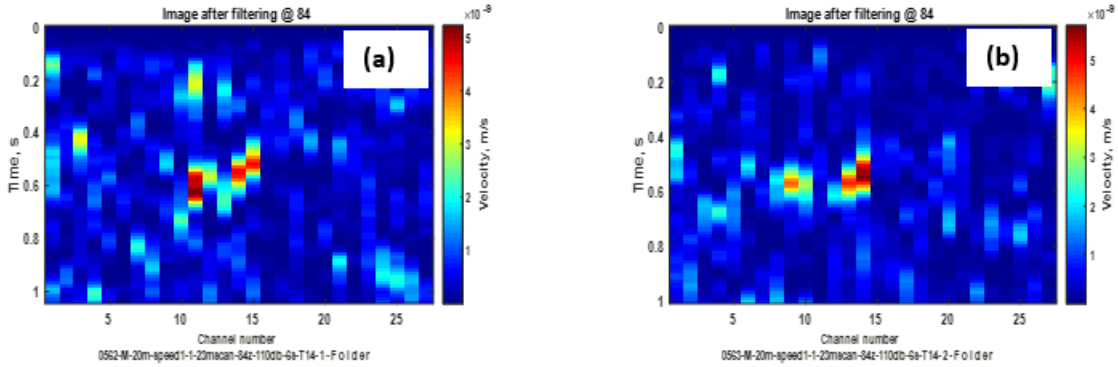

Figure 74. Vibration image of target 14 obtained in a moving mode at 20 m distance for different speeds of vehicle: (a) - 1.18 m/s (2.6 mph), (b) - 1.23 m/s (2.75 mph). Excitation at 84 Hz frequency was provided by a speaker.

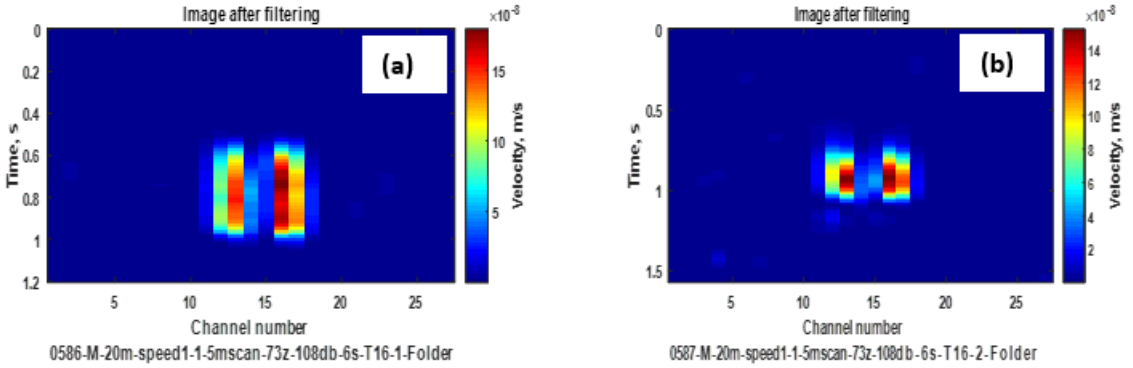

Figure 75. Vibration image of target 16 obtained in a moving mode at 20 m distance for different speeds of vehicle: (a) - 1.26 m/s (2.8 mph), (b) - 0.95 m/s (2.1 mph). Excitation at 73 Hz frequency was provided by a speaker.

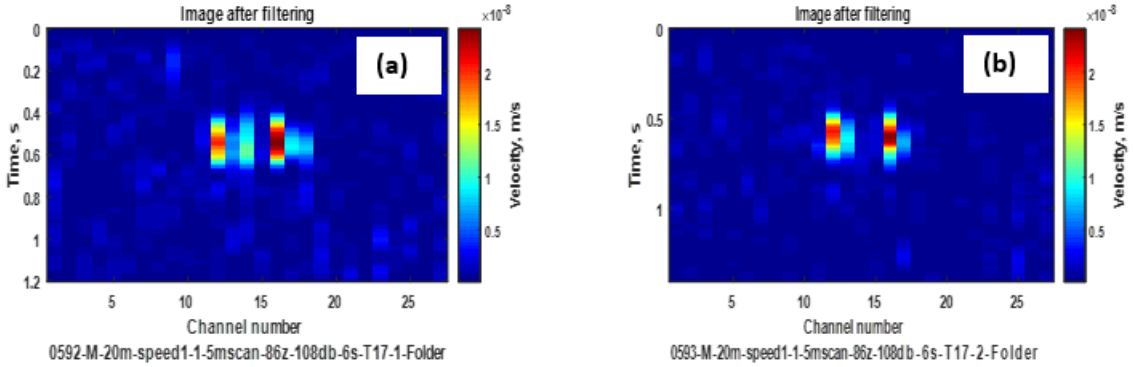

Figure 76. Vibration image of target 17 obtained in a moving mode at 20 m distance for different speeds of vehicle: (a) - 1.26 m/s (2.8 mph), (b) - 0.95 m/s (2.1 mph). Excitation at 86 Hz frequency was provided by a speaker.

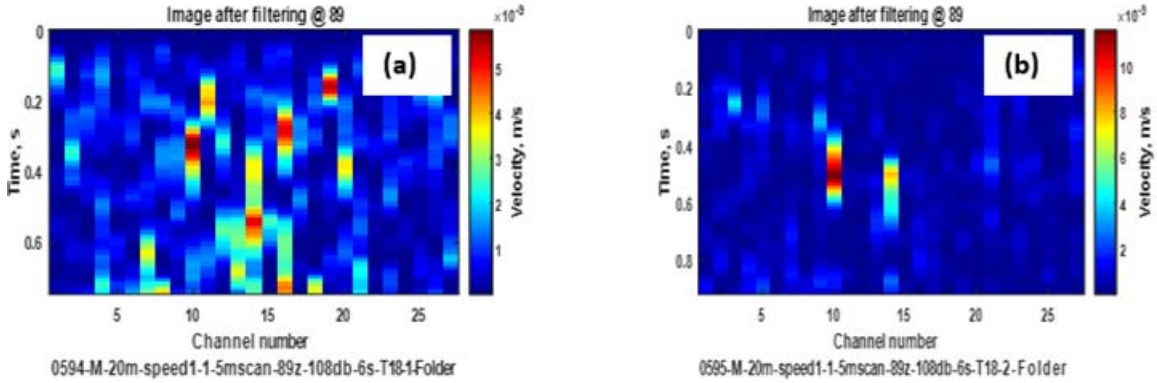

Figure 77. Vibration image of target 18 obtained in a moving mode at 20 m distance for different speeds of vehicle: (a) - 2.14 m/s (4.8 mph), (b) - 1.66 m/s (3.7 mph). Excitation at 89 Hz frequency was provided by a speaker.

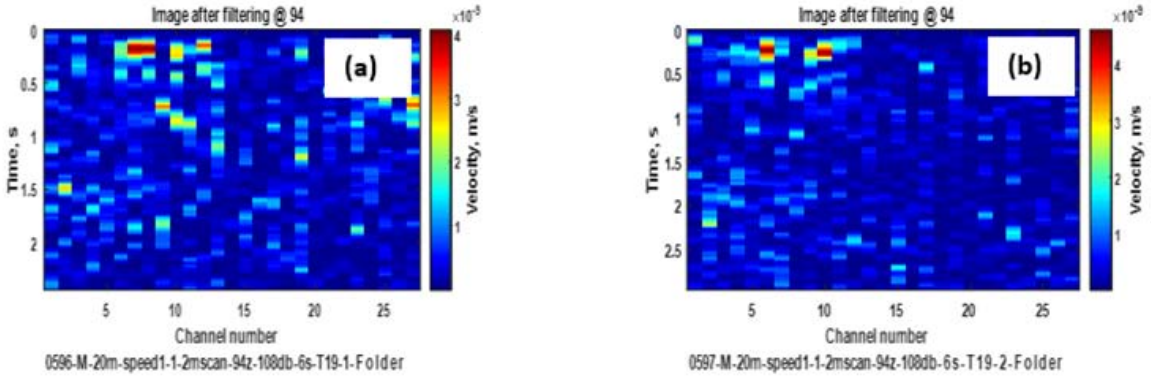

Figure 78. Vibration image of target 19 obtained in a moving mode at 20 m distance for different speeds of vehicle: (a) - 0.61 m/s (1.36 mph), (b) - 0.51 m/s (1.14 mph). Excitation at 94 Hz frequency was provided by a speaker.

One can see from Figures 68 - 78 that vibration images of some targets show low spatial resolution, having only one or two pixels, which is caused by large, 72 mm, separation between beams on the ground for 20 m standoff distance.

12.2 Vibration imaging of buried objects from a stationary vehicle

Vibration imaging of a buried object in a scanning mode was completed by scanning laser beams over the selected ground area due to angular motion of the LMBDIS scanning mirror, on a stationary vehicle. Laser beams scanned the object back and forth two times during data recording. As a result, the vibration image of the scanned area contains two images of the object - each image for the beams scanning in one direction. The objects were measured for both speaker and HFWS excitation sources. Measurements were completed for selected objects, whose frequency response was characterized earlier using geophones. The objects were measured at distances of 10 m and 20 m for excitation provided by a speaker and a HFWS. A plastic box 36"x32'x6" was measured at 40 m distance, using a speaker for excitation. Measurements of other objects at 40 m distance were not practical, because of large separation, 144 mm, between beams on the ground for 40 m standoff distance. In measurements with a speaker, the speaker was located about 2 m from the measured object. The HFWS was located at 10 m from a measured target. Table 3 shows a list of measured objects for the scanning mode, the excitation source used, the frequency of excitation, and the distance to the object for each measurement. It also shows if the object was detected or not detected by using symbols "Y" for detected, and "N" for not detected. Symbol "N/A" shows that the object was not measured.

Table 3. Accomplished measurements for the scanning mode. Y - detected, N - not detected, N/A - not measured

Target position	Target type	Depth	Distance 10 m		Distance 20 m		Distance 40 m
			Speaker	HFWS	Speaker	HFWS	Speaker
Target1	M19	0”	Y, 115 Hz	N/A	N/A	N/A	N/A
Target2	M19	2”	Y, 118 Hz	Y, 94 Hz	Y, 94 Hz	N/A	N/A
Target3	M19	4”	Y, 110 Hz	Y, 103 Hz	Y,103Hz	N/A	N/A
Target4	TM46	0”	Y, 167 Hz	N/A	N/A	N/A	N/A
Target5	TM46	2”	Y, 115 Hz	N, 115 Hz	N, 130 Hz	N, 130 Hz	N/A
Target6	TM46	4”	N, 110 Hz	Y, 115 Hz	Y, 130 Hz	Y, 130 Hz	N/A
Target7	TM46	6”	Y, 114 Hz	Y, 115 Hz	Y, 130 Hz	Y, 130 Hz	N/A
Target8	VS1.6	0”	Y, 151 Hz	N/A	N/A	N/A	N/A
Target9	VS1.6	2”	Y, 104 Hz	Y, 120 Hz	N/A	N/A	N/A
Target10	VS1.6	4”	Y, 118 Hz	Y, 150 Hz	Y, 120 Hz	N/A	N/A
Target11	VS1.6	6”	Y, 112 Hz	Y, 150 Hz	N	N/A	N/A
Target12	Jug	2”	Y, 79 Hz	Y, 80 Hz	Y, 80 Hz	N/A	N/A
Target13	Jug	4”	Y, 81 Hz	Y, 80 Hz	Y, 85 Hz	N/A	N/A
Target14	Jug	6”	Y, 92 Hz	Y, 90 Hz	Y, 97 Hz	Y, 84 Hz	N/A
Target15	Jug	8”	Y, 90 Hz	Y, 70 Hz	Y, 90 Hz	Y, 90 Hz	N/A
Target16	Can	2”	Y, 95 Hz	Y, 80 Hz	Y, 71 Hz	N/A	N/A
Target17	Can	4”	Y, 79 Hz	Y, 70 Hz	Y, 86 Hz	N/A	N/A
Target18	Can	6”	Y, 89 Hz	Y, 89 Hz	Y, 89 Hz	Y, 125 Hz	N/A
Target19	Can	8”	Y, 86 Hz	Y, 80 Hz	N/A	Y, 94 Hz, 125Hz	N/A
Target 20	Box	1"	N/A	N/A	N/A	N/A	Y, 58 Hz

Figures 79 - 96 show vibration images of detected targets from a stationary vehicle at 10 m standoff distance using a speaker as an excitation source. The SPL level was in the range from 107 dB to 110 dB.

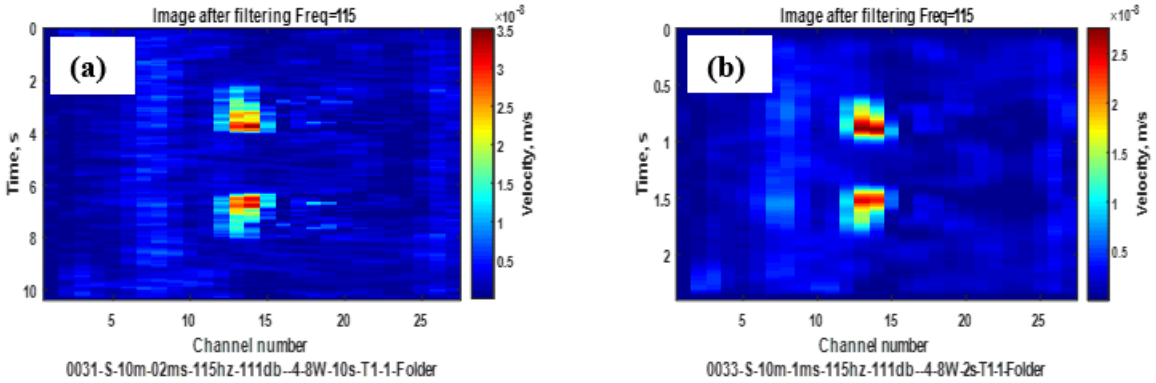

Figure 79. Vibration image of target 1 obtained from a stationary vehicle in a scanning mode at 10 m distance for different speeds of beams: (a) - 0.2 m/s (0.45 mph), (b) - 1 m/s (2.2 mph). Excitation at 115 Hz frequency was provided by a speaker.

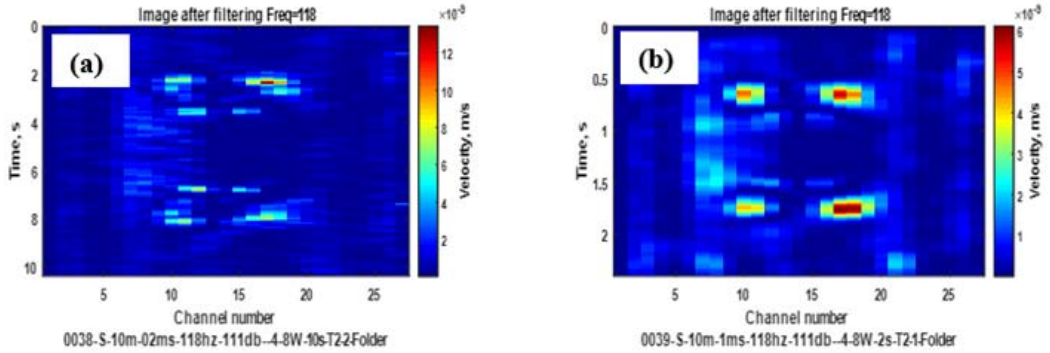

Figure 80. Vibration image of target 2 obtained from a stationary vehicle in a scanning mode at 10 m distance for different speeds of beams: (a) - 0.2 m/s (0.45 mph), (b) - 1 m/s (2.2 mph). Excitation at 118 Hz frequency was provided by a speaker.

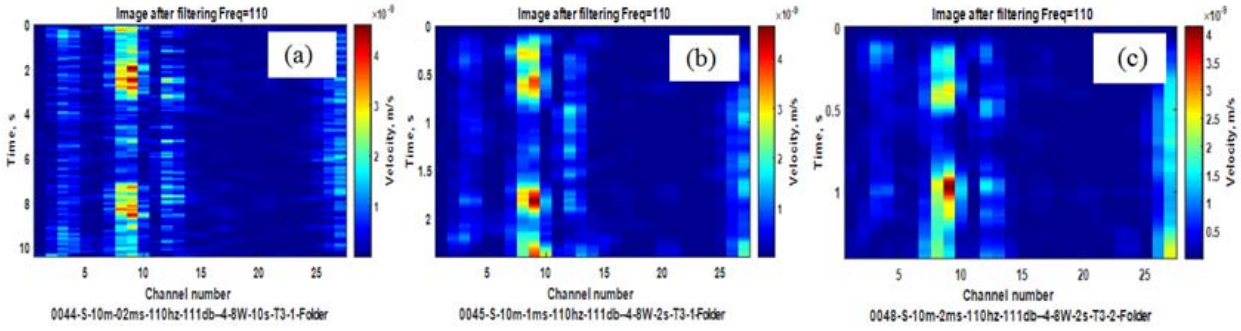

Figure 81. Vibration image of target 3 obtained from a stationary vehicle in a scanning mode at 10 m distance for different speeds of beams: (a) - 0.2 m/s (0.45 mph), (b) - 1 m/s (2.2 mph), and (c) - 2 m/s (4.4 mph). Excitation at 110 Hz frequency was provided by a speaker.

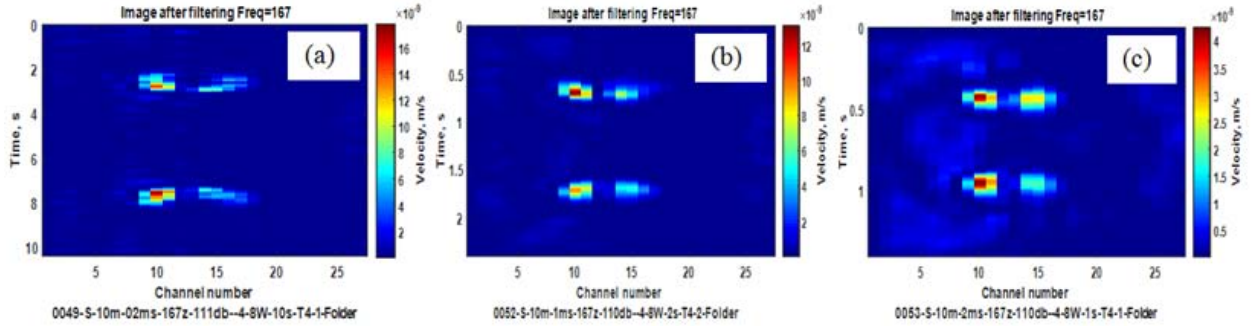

Figure 82. Vibration image of target 4 obtained from a stationary vehicle in a scanning mode at 10 m distance for different speeds of beams: (a) - 0.2 m/s (0.45 mph), (b) - 1 m/s (2.2 mph), and (c) - 2 m/s (4.4 mph). Excitation at 167 Hz frequency was provided by a speaker.

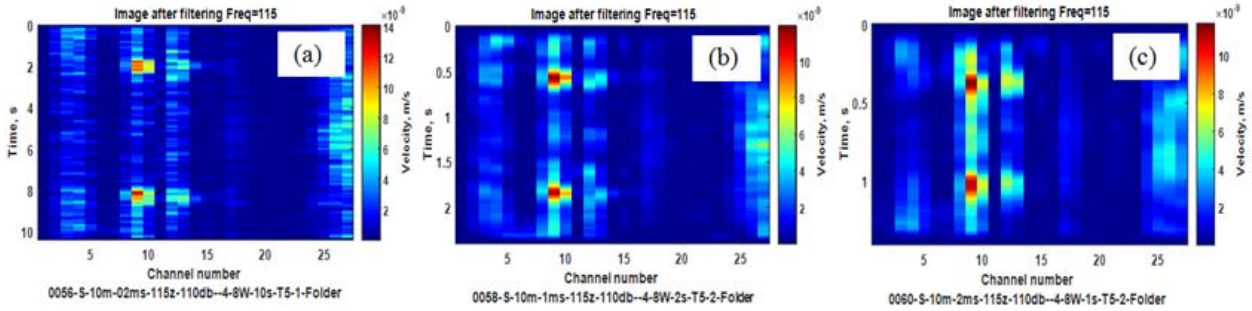

Figure 83. Vibration image of target 5 obtained from a stationary vehicle in a scanning mode at 10 m distance for different speeds of beams: (a) - 0.2 m/s (0.45 mph), (b) - 1 m/s (2.2 mph), and (c) - 2 m/s (4.4 mph). Excitation at 115 Hz frequency was provided by a speaker.

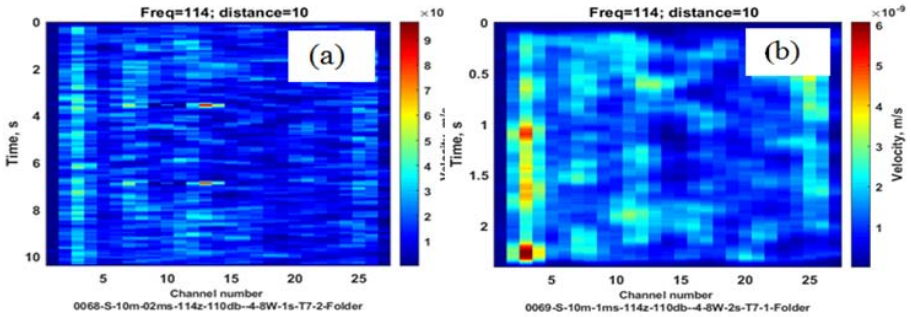

Figure 84. Vibration image of target 7 obtained from a stationary vehicle in a scanning mode at 10 m distance for different speeds of beams: (a) - 0.2 m/s (0.45 mph), (b) - 1 m/s (2.2 mph). Excitation at 114 Hz frequency was provided by a speaker.

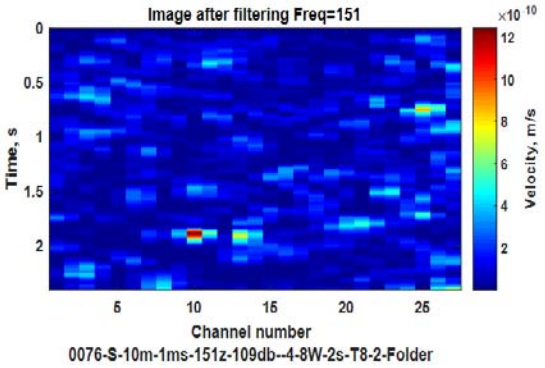

Figure 85. Vibration image of target 8 obtained from a stationary vehicle in a scanning mode at 10 m distance for speed of beams 1 m/s (2.2 mph). Excitation at 151 Hz frequency was provided by a speaker.

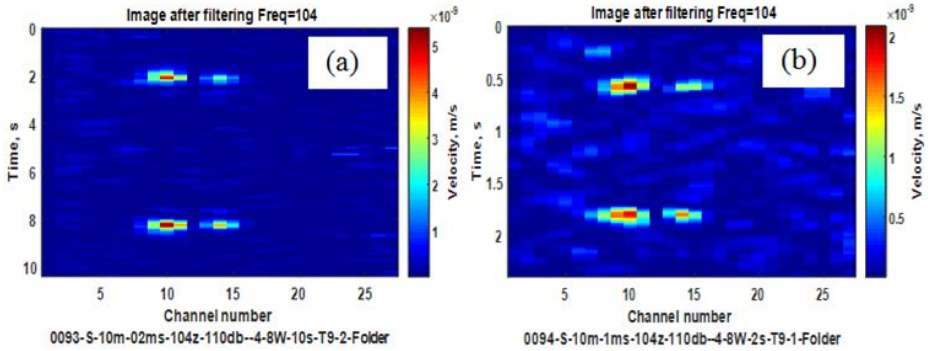

Figure 86. Vibration image of target 9 obtained from a stationary vehicle in a scanning mode at 10 m distance for different speeds of beams: (a) - 0.2 m/s (0.45 mph), (b) - 1 m/s (2.2 mph). Excitation at 104 Hz frequency was provided by a speaker.

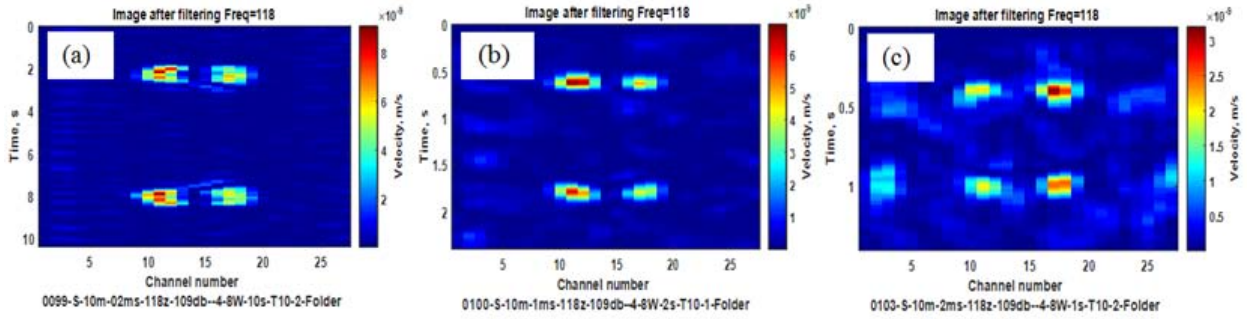

Figure 87. Vibration image of target 10 obtained from a stationary vehicle in a scanning mode at 10 m distance for different speeds of beams: (a) - 0.2 m/s (0.45 mph), (b) - 1 m/s (2.2 mph), and (c) - 2 m/s (4.4 mph). Excitation at 118 Hz frequency was provided by a speaker.

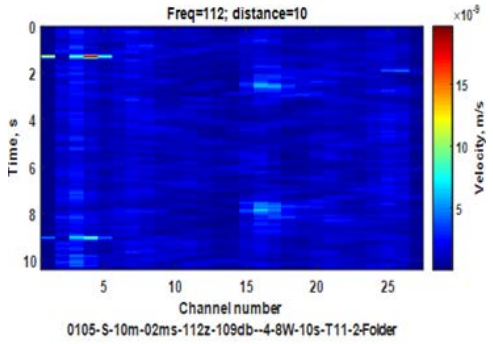

Figure 88. Vibration image of target 11 obtained from a stationary vehicle in a scanning mode at 10 m distance for the speed of beams 0.2 m/s (0.45 mph) Excitation at 112 Hz frequency was provided by a speaker.

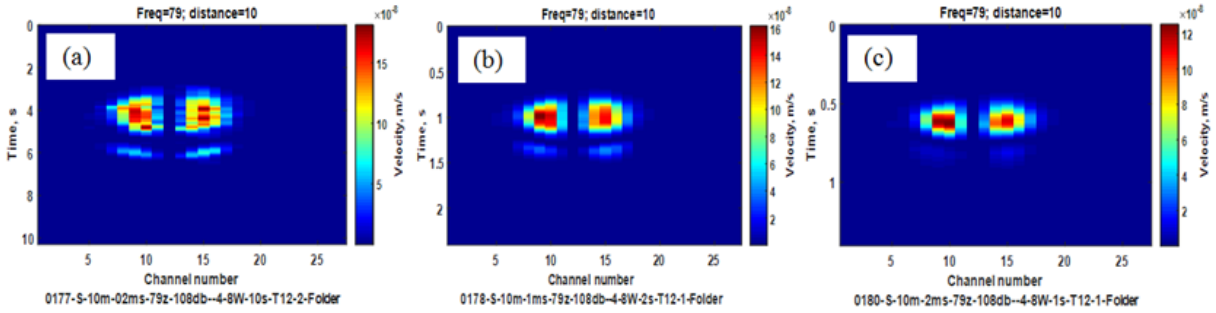

Figure 89. Vibration image of target 12 obtained from a stationary vehicle in a scanning mode at 10 m distance for different speeds of beams: (a) - 0.1 m/s (0.22 mph), (b) - 0.5 m/s (1.1 mph), and (c) - 1 m/s (2.2 mph). Excitation at 79 Hz frequency was provided by a speaker.

Target 12 was measured by scanning beams only in one direction. So, the scanned area contains only one image.

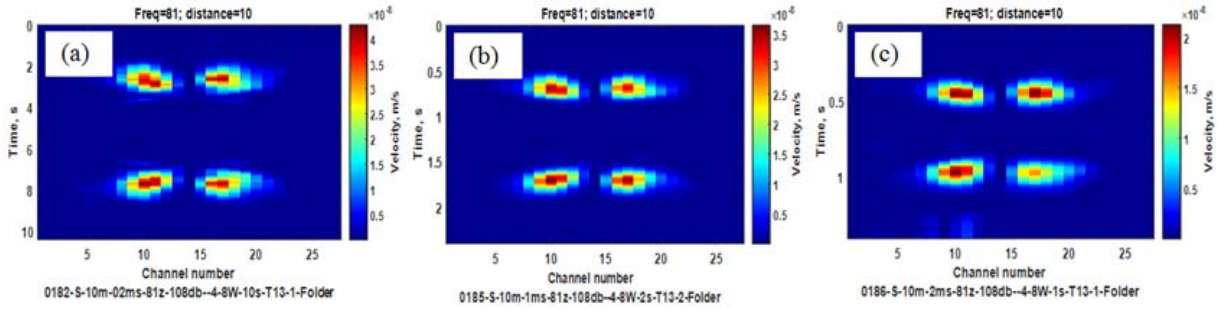

Figure 90. Vibration image of target 13 obtained from a stationary vehicle in a scanning mode at 10 m distance for different speeds of beams: (a) - 0.2 m/s (0.45 mph), (b) - 1 m/s (2.2 mph), and (c) - 2 m/s (4.4 mph). Excitation at 81 Hz frequency was provided by a speaker.

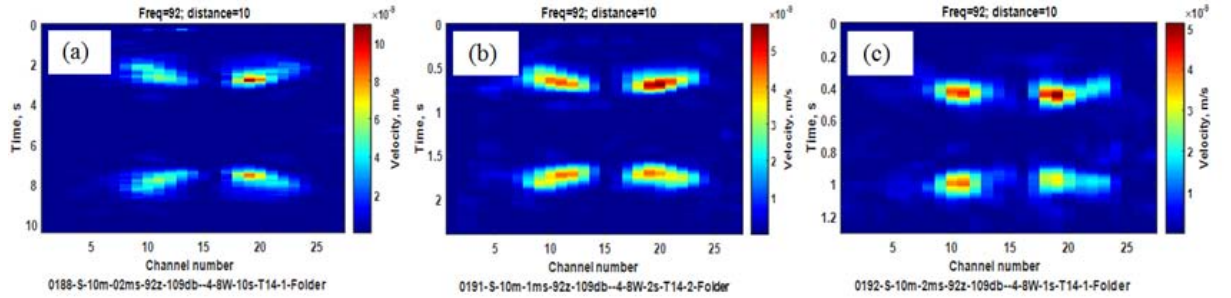

Figure 91. Vibration image of target 14 obtained from a stationary vehicle in a scanning mode at 10 m distance for different speeds of beams: (a) - 0.2 m/s (0.45 mph), (b) - 1 m/s (2.2 mph), and (c) - 2 m/s (4.4 mph). Excitation at 92 Hz frequency was provided by a speaker.

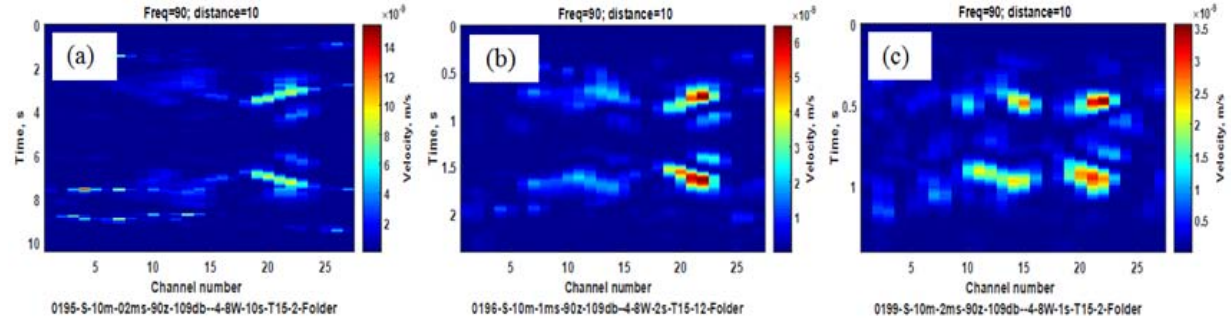

Figure 92. Vibration image of target 15 obtained from a stationary vehicle in a scanning mode at 10 m distance for different speeds of beams: (a) - 0.2 m/s (0.45 mph), (b) - 1 m/s (2.2 mph), and (c) - 2 m/s (4.4 mph). Excitation at 90 Hz frequency was provided by a speaker.

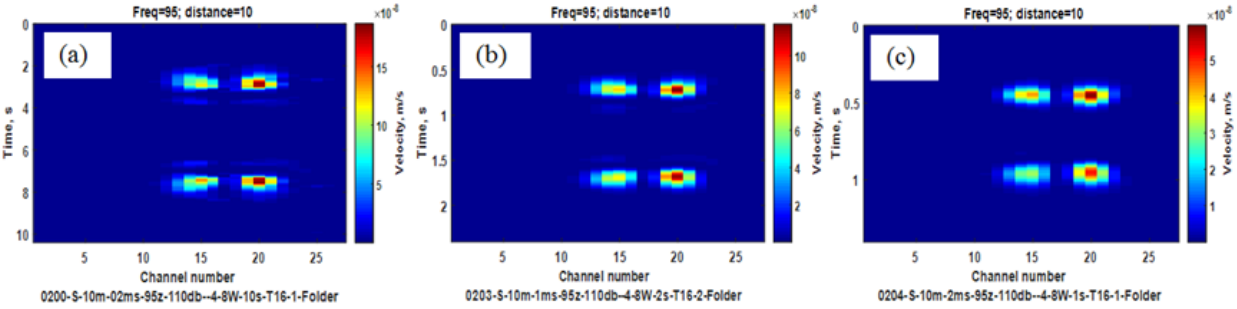

Figure 93. Vibration image of target 16 obtained from a stationary vehicle in a scanning mode at 10 m distance for different speeds of beams: (a) - 0.2 m/s (0.45 mph), (b) - 1 m/s (2.2 mph), and (c) - 2 m/s (4.4 mph). Excitation at 95 Hz frequency was provided by a speaker.

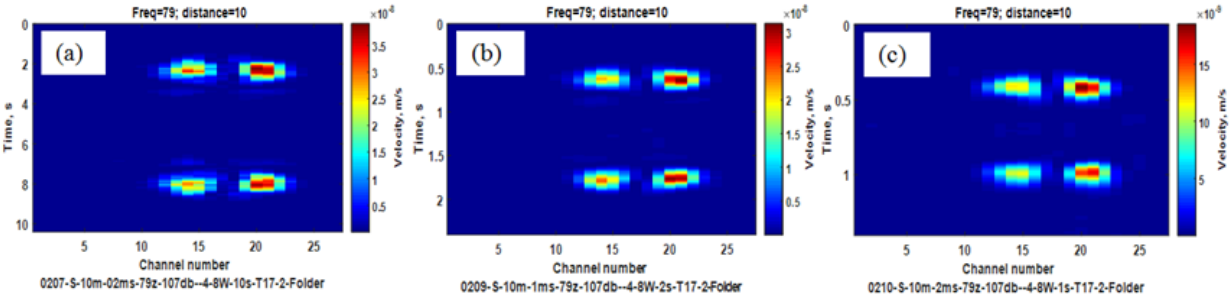

Figure 94. Vibration image of target 17 obtained from a stationary vehicle in a scanning mode at 10 m distance for different speeds of beams: (a) - 0.2 m/s (0.45 mph), (b) - 1 m/s (2.2 mph), and (c) - 2 m/s (4.4 mph). Excitation at 79 Hz frequency was provided by a speaker.

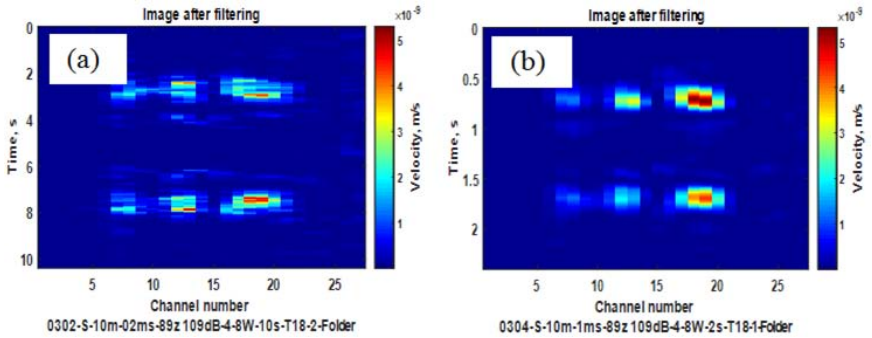

Figure 95. Vibration image of target 18 obtained from a stationary vehicle in a scanning mode at 10 m distance for different speeds of beams: (a) - 0.2 m/s (0.45 mph), (b) - 1 m/s (2.2 mph) Excitation at 89 Hz frequency was provided by a speaker.

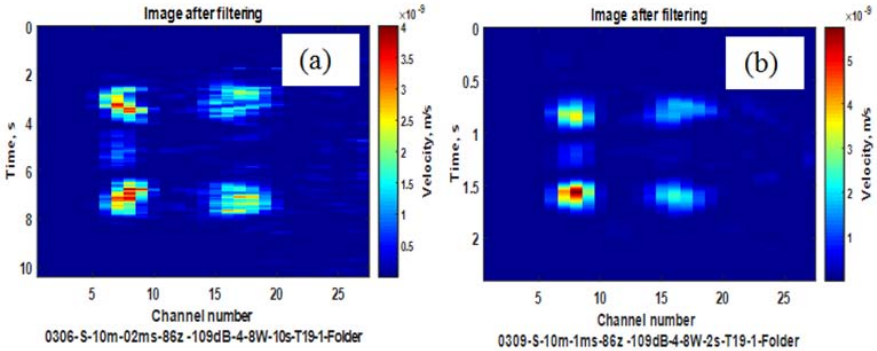

Figure 96. Vibration image of target 19 obtained from a stationary vehicle in a scanning mode at 10 m distance for different speeds of beams: (a) - 0.2 m/s (0.45 mph), (b) - 1 m/s (2.2 mph) Excitation at 86 Hz frequency was provided by a speaker.

Figures 97 - 112 show vibration images of detected targets from a stationary vehicle at 10 m standoff distance using a HFWS as an excitation source.

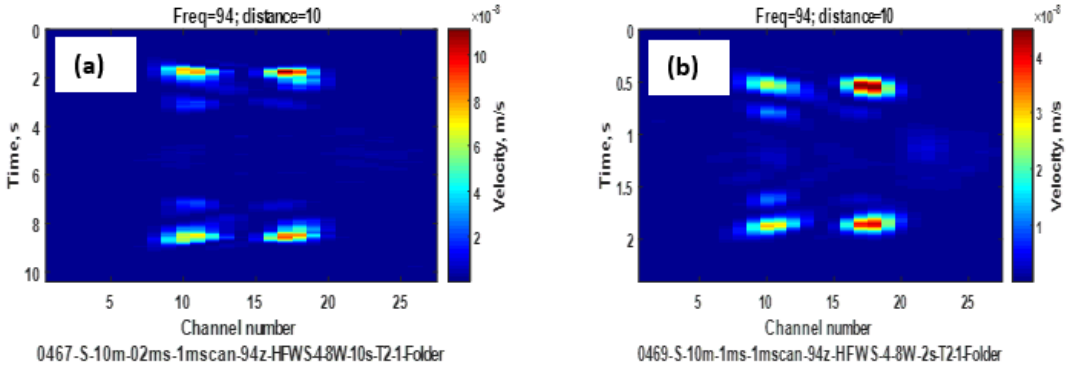

Figure 97. Vibration image of target 2 obtained from a stationary vehicle in a scanning mode at 10 m distance for different speeds of beams: (a) - 0.2 m/s (0.45 mph), (b) - 1 m/s (2.2 mph). Excitation at 94 Hz frequency was provided by HFWS.

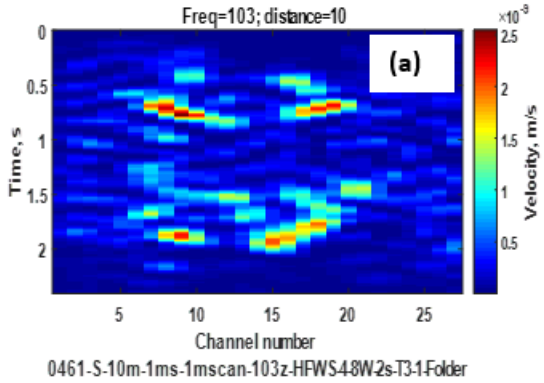

Figure 98. Vibration image of target 3 obtained from a stationary vehicle in a scanning mode at 10 m distance for different speeds of beams: (a) - 0.2 m/s (0.45 mph), (b) - 1 m/s (2.2 mph). Excitation at 103 Hz frequency was provided by HFWS.

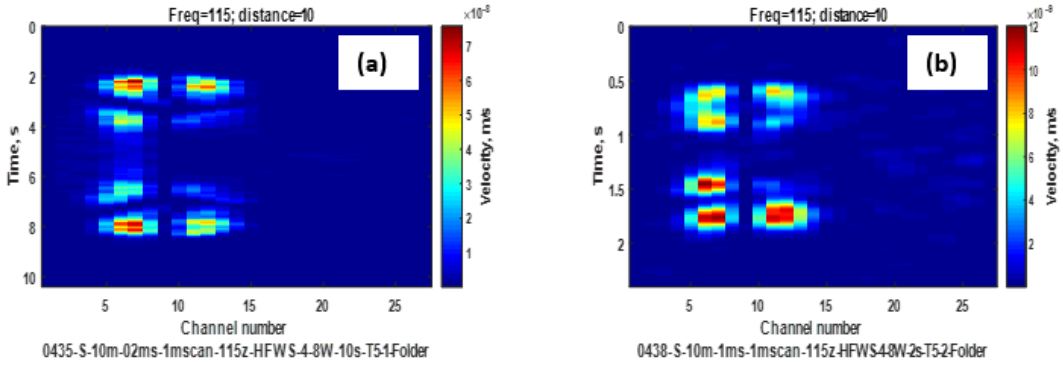

Figure 99. Vibration image of target 5 obtained from a stationary vehicle in a scanning mode at 10 m distance for different speeds of beams: (a) - 0.2 m/s (0.45 mph), (b) - 1 m/s (2.2 mph). Excitation at 115 Hz frequency was provided by HFWS.

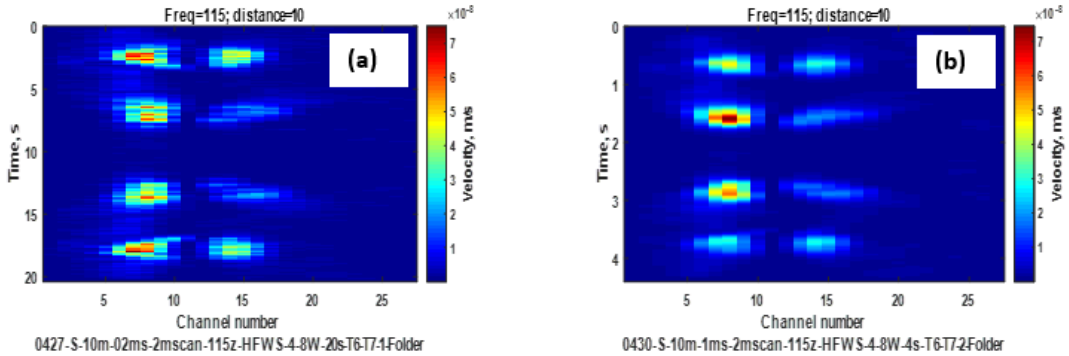

Figure 100. Vibration image of targets 6 and 7 obtained from a stationary vehicle in a scanning mode at 10 m distance for different speeds of beams: (a) - 0.2 m/s (0.45 mph), (b) - 1 m/s (2.2 mph). Excitation at 115 Hz frequency was provided by HFWS.

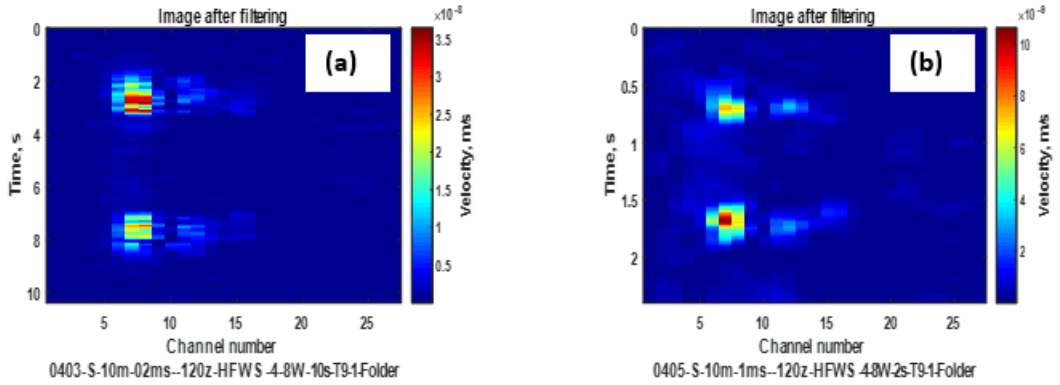

Figure 101. Vibration image of target 9 obtained from a stationary vehicle in a scanning mode at 10 m distance for different speeds of beams: (a) - 0.2 m/s (0.45 mph), (b) - 1 m/s (2.2 mph). Excitation at 120 Hz frequency was provided by HFWS.

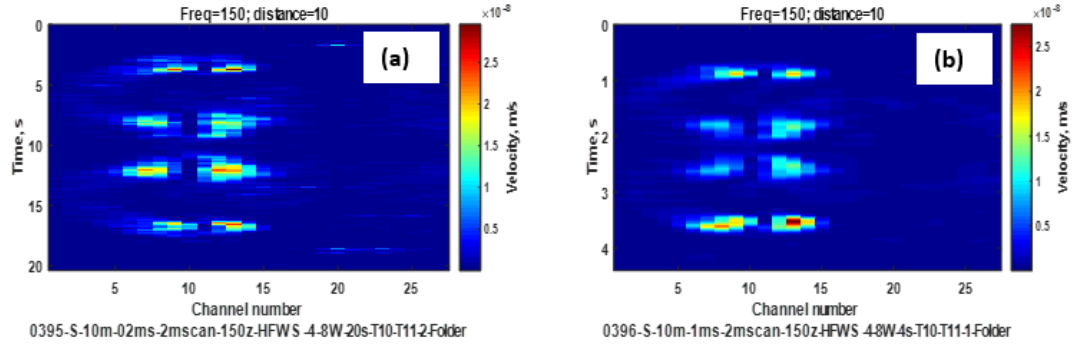

Figure 102. Vibration image of target 10 and 11 obtained from a stationary vehicle in a scanning mode at 10 m distance for different speeds of beams: (a) - 0.2 m/s (0.45 mph), (b) - 1 m/s (2.2 mph). Excitation at 150 Hz frequency was provided by HFWS.

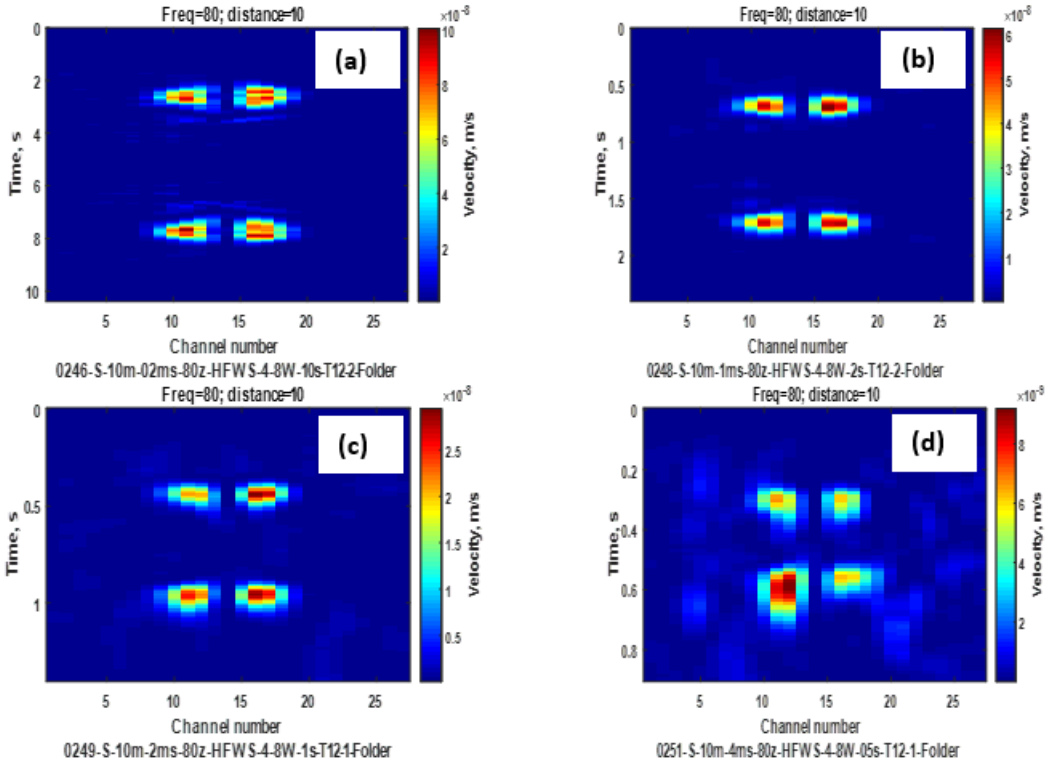

Figure 103. Vibration image of target 12 obtained from a stationary vehicle in a scanning mode at 10 m distance for different speeds of beams: (a) - 0.2 m/s (0.45 mph), (b) - 1 m/s (2.2 mph), (c) - 2 m/s (4.4 mph), (d) - 4 m/s (8.9 mph). Excitation at 80 Hz frequency was provided by HFWS.

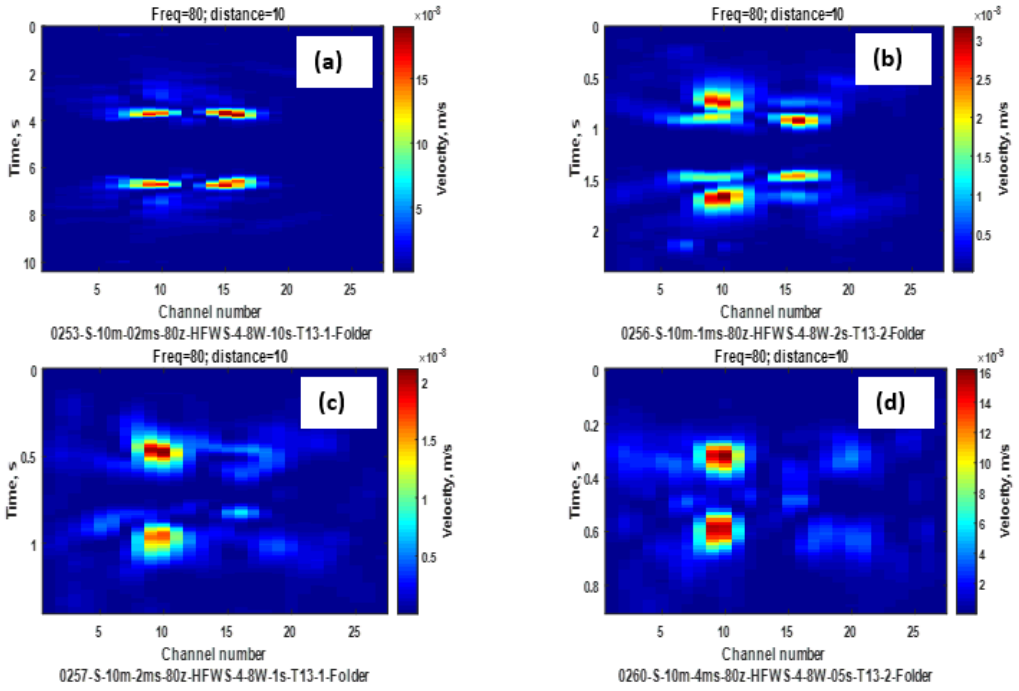

Figure 104. Vibration image of target 13 obtained from a stationary vehicle in a scanning mode at 10 m distance for different speeds of beams: (a) - 0.2 m/s (0.45 mph), (b) - 1 m/s (2.2 mph), (c) - 2 m/s (4.4 mph), (d) - 4 m/s (8.9 mph). Excitation at 80 Hz frequency was provided by HFWS.

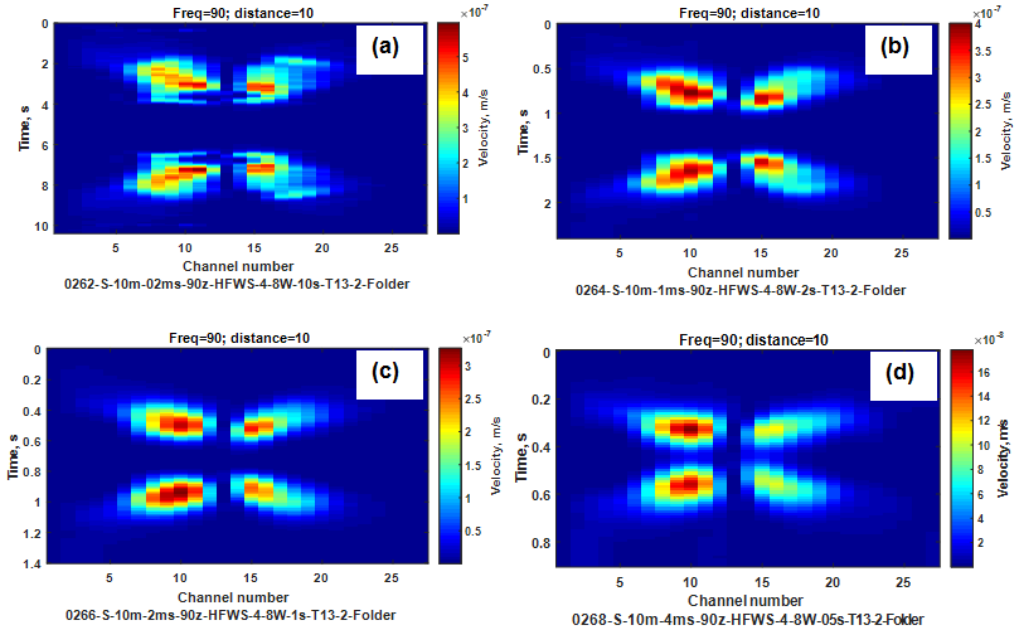

Figure 105. Vibration image of target 13 obtained from a stationary vehicle in a scanning mode at 10 m distance for different speeds of beams: (a) - 0.2 m/s (0.45 mph), (b) - 1 m/s (2.2 mph),

(c) - 2 m/s (4.4 mph), (d) - 4 m/s (8.9 mph). Excitation at 90 Hz frequency was provided by HFWS.

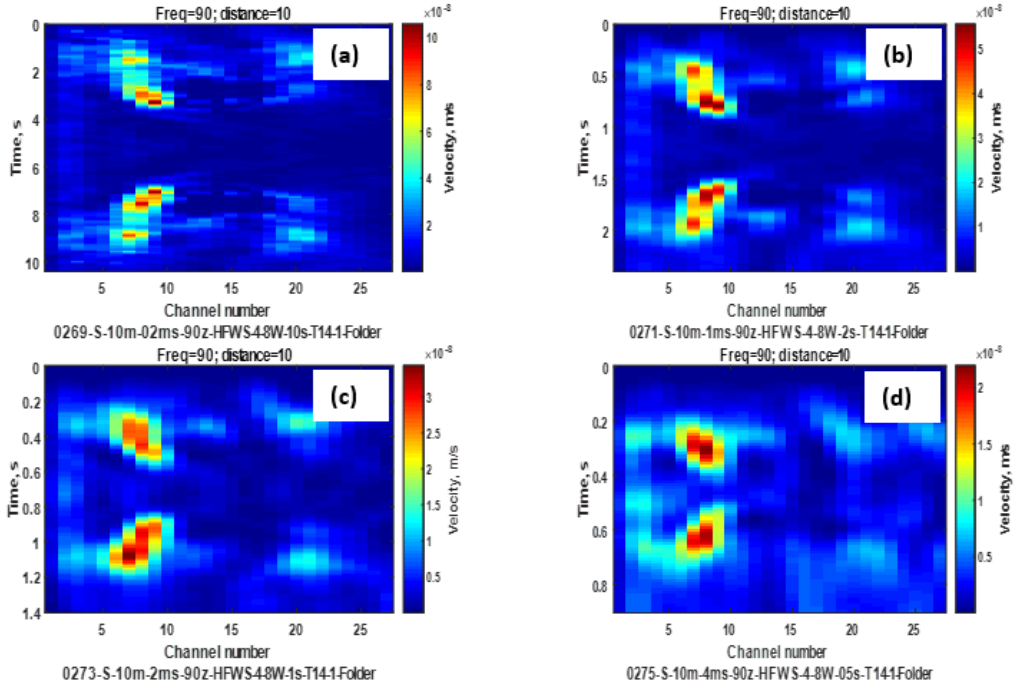

Figure 106. Vibration image of target 14 obtained from a stationary vehicle in a scanning mode at 10 m distance for different speeds of beams: (a) - 0.2 m/s (0.45 mph), (b) - 1 m/s (2.2 mph), (c) - 2 m/s (4.4 mph), (d) - 4 m/s (8.9 mph). Excitation at 90 Hz frequency was provided by HFWS.

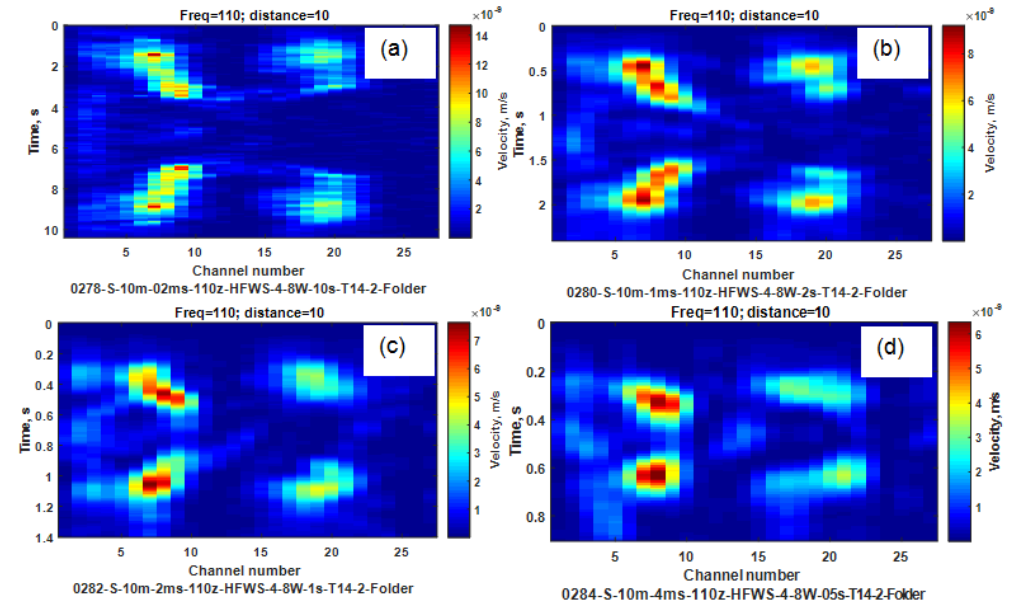

Figure 107. Vibration image of target 14 obtained from a stationary vehicle in a scanning mode at 10 m distance for different speeds of beams: (a) - 0.2 m/s (0.45 mph), (b) - 1 m/s (2.2 mph), (c) - 2 m/s (4.4 mph), (d) - 4 m/s (8.9 mph). Excitation at 110 Hz frequency was provided by HFWS.

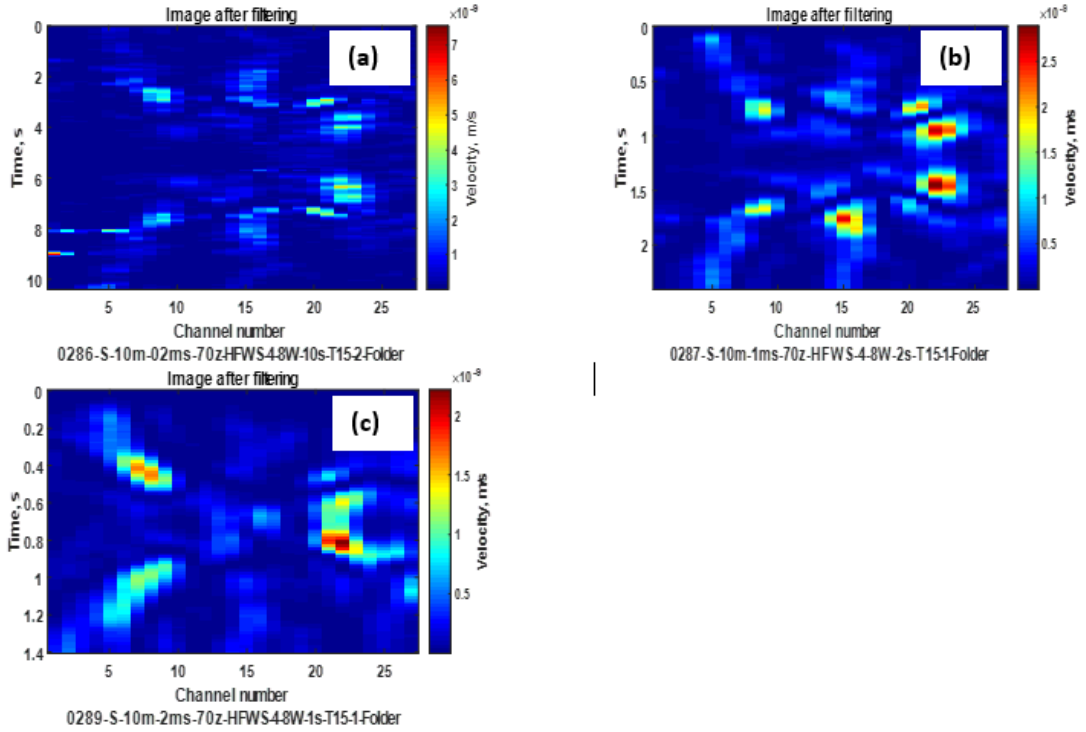

Figure 108. Vibration image of target 15 obtained from a stationary vehicle in a scanning mode at 10 m distance for different speeds of beams: (a) - 0.2 m/s (0.45 mph), (b) - 1 m/s (2.2 mph), (c) - 2 m/s (4.4 mph). Excitation at 70 Hz frequency was provided by HFWS.

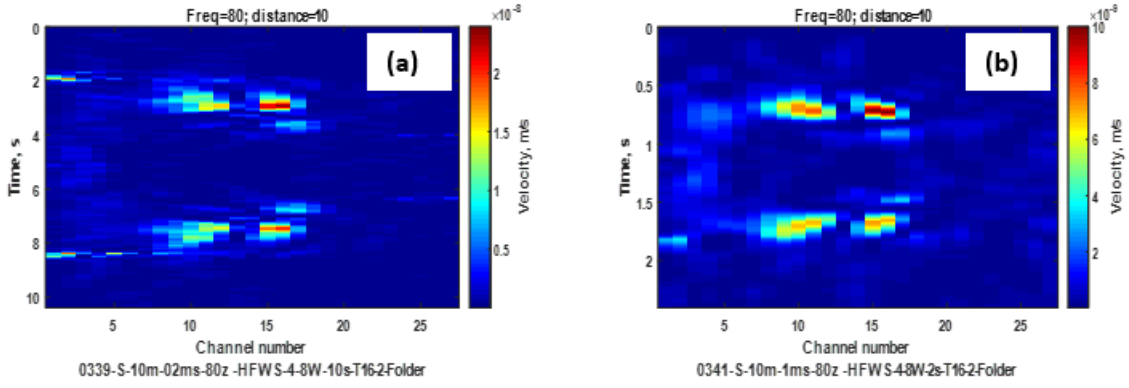

Figure 109. Vibration image of target 16 obtained from a stationary vehicle in a scanning mode at 10 m distance for different speeds of beams: (a) - 0.2 m/s (0.45 mph), (b) - 1 m/s (2.2 mph) Excitation at 80 Hz frequency was provided by HFWS.

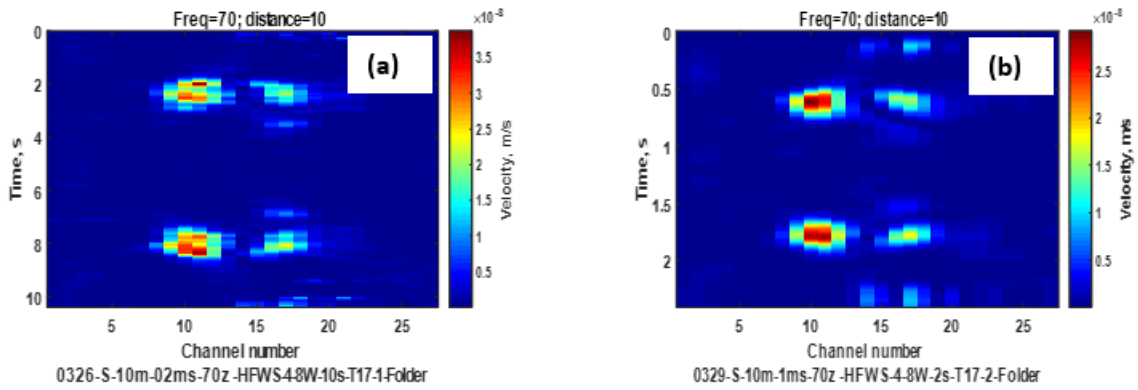

Figure 110. Vibration image of target 17 obtained from a stationary vehicle in a scanning mode at 10 m distance for different speeds of beams: (a) - 0.2 m/s (0.45 mph), (b) - 1 m/s (2.2 mph). Excitation at 70 Hz frequency was provided by HFWS.

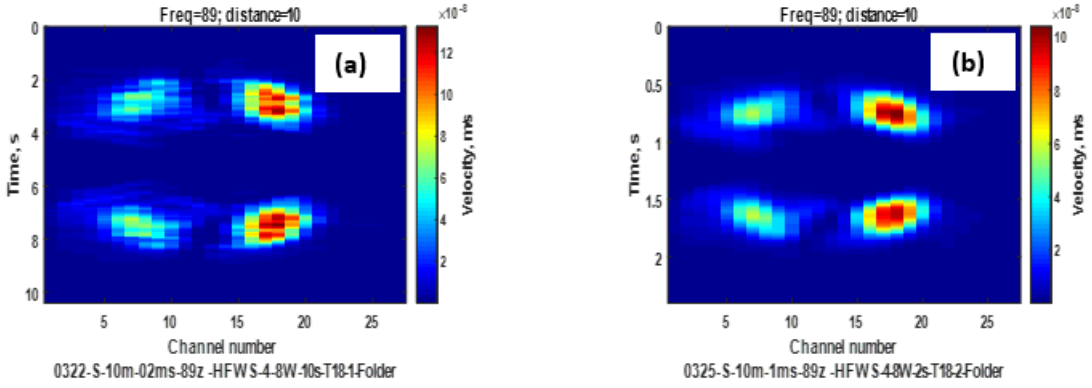

Figure 111. Vibration image of target 18 obtained from a stationary vehicle in a scanning mode at 10 m distance for different speeds of beams: (a) - 0.2 m/s (0.45 mph), (b) - 1 m/s (2.2 mph). Excitation at 89 Hz frequency was provided by HFWS.

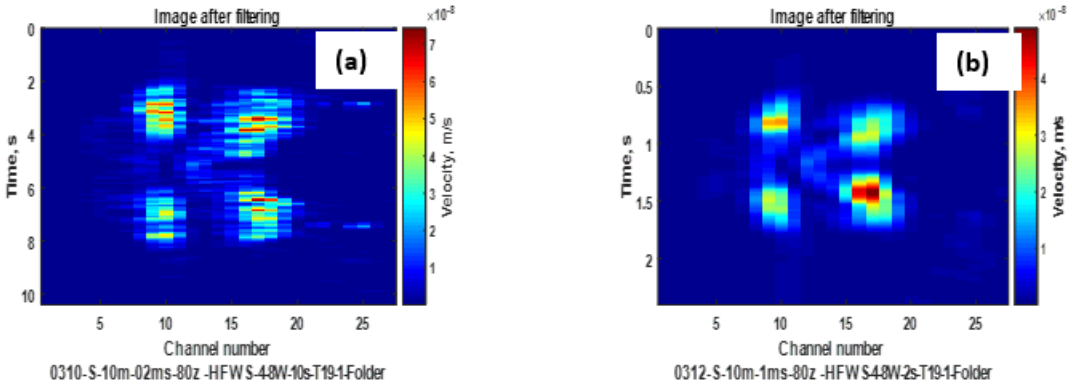

Figure 112. Vibration image of target 19 obtained from a stationary vehicle in a scanning mode at 10 m distance for different speeds of beams: (a) - 0.2 m/s (0.45 mph), (b) - 1 m/s (2.2 mph). Excitation at 80 Hz frequency was provided by HFWS.

Figures 113 - 123 show vibration images of detected targets from a stationary vehicle at 20 m standoff distance using a speaker as an excitation source. Figure 124 shows a vibration image of a plastic box 36 x 32 x 6 inches buried 1 inch deep from a stationary vehicle at 40 m standoff distance using a speaker as an excitation source.

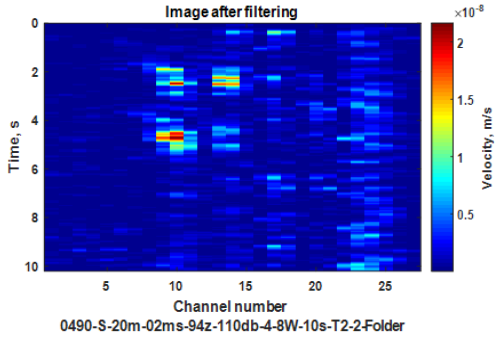

Figure 113. Vibration image of target 2 obtained from a stationary vehicle in a scanning mode at 20 m distance for speed of beams 0.2 m/s (0.45 mph) Excitation at 94 Hz frequency was provided by a speaker.

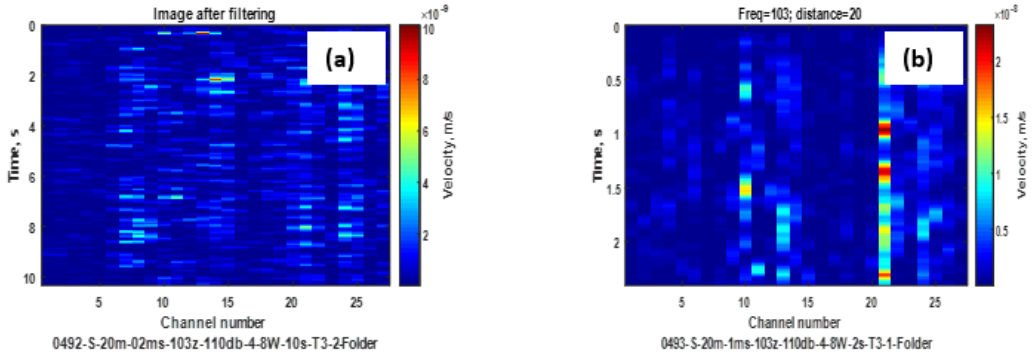

Figure 114. Vibration image of target 3 obtained from a stationary vehicle in a scanning mode at 20 m distance for different speeds of beams: (a) - 0.2 m/s (0.45 mph), (b) - 1 m/s (2.2 mph). Excitation at 103 Hz frequency was provided by a speaker.

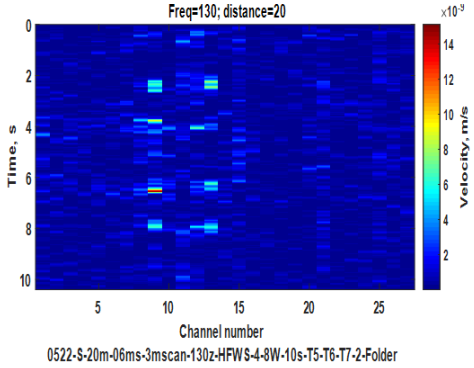

Figure 115. Vibration image of targets 5, 6, and 7 obtained from a stationary vehicle in a scanning mode at 20 m distance for speed of beams 0.2 m/s (0.45 mph). Excitation at 130 Hz frequency was provided by a speaker.

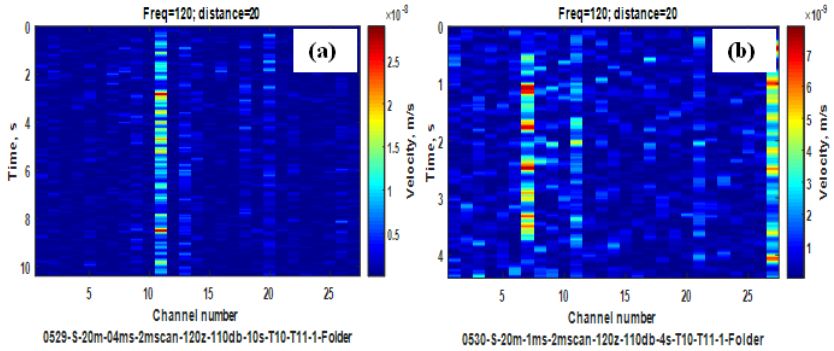

Figure 116. Vibration image of targets 10 and 11 obtained from a stationary vehicle in a scanning mode at 20 m distance for speed of beams 0.2 m/s (0.45 mph), b) - 1 m/s (2.2 mph). Excitation at 120 Hz frequency was provided by a speaker.

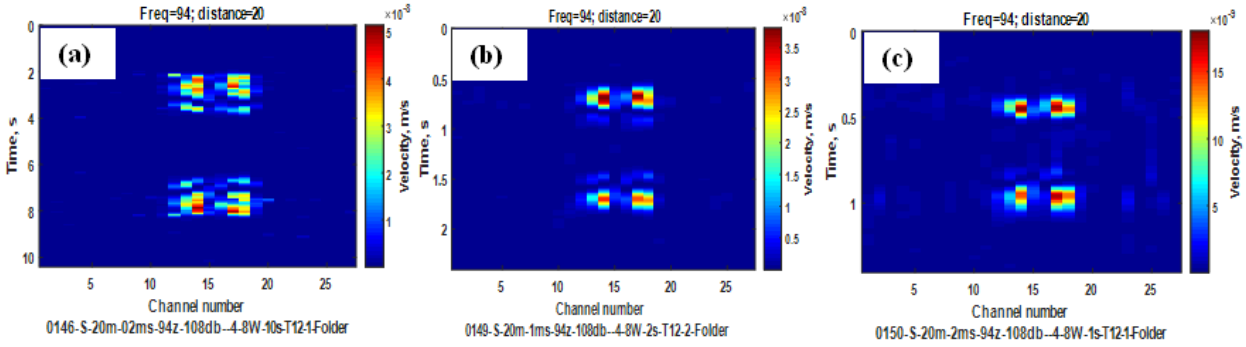

Figure 117. Vibration image of target 12 obtained from a stationary vehicle in a scanning mode at 20 m distance for different speeds of beams: (a) - 0.2 m/s (0.45 mph), (b) - 1 m/s (2.2 mph), (c) - 2 m/s (4.4 mph). Excitation at 94 Hz frequency was provided by a speaker.

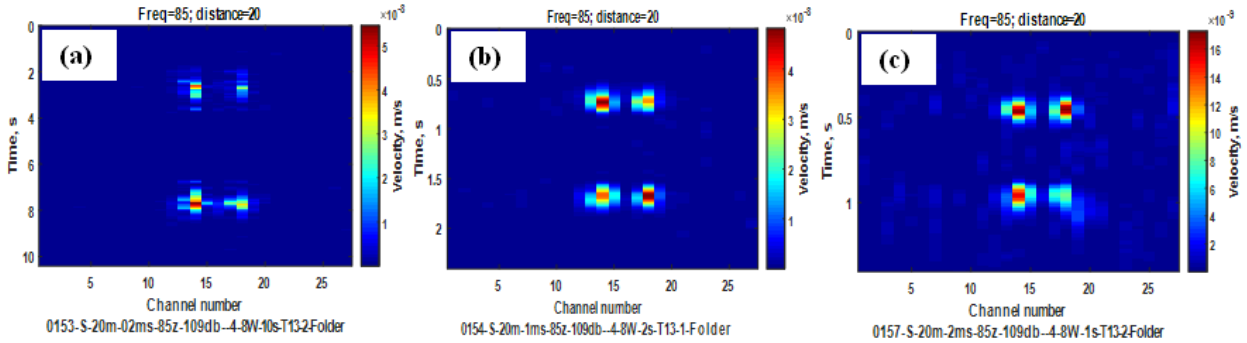

Figure 118. Vibration image of target 13 obtained from a stationary vehicle in a scanning mode at 20 m distance for different speeds of beams: (a) - 0.2 m/s (0.45 mph), (b) - 1 m/s (2.2 mph), (c) - 2 m/s (4.4 mph). Excitation at 85 Hz frequency was provided by a speaker.

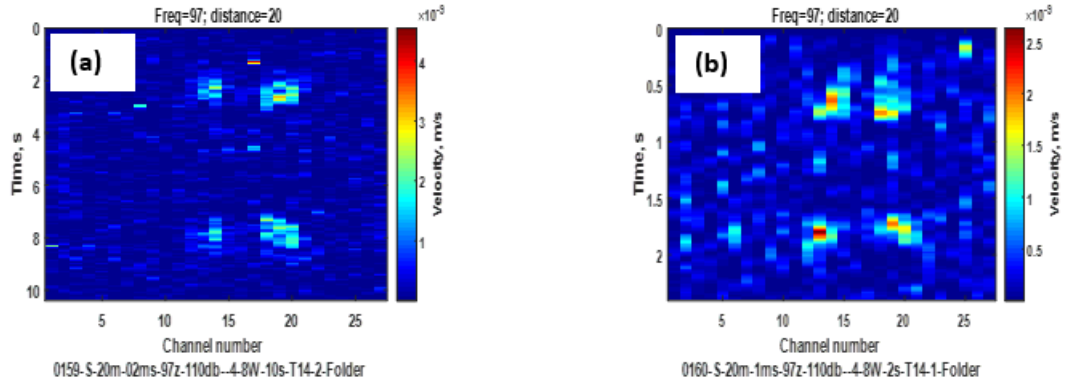

Figure 119. Vibration image of target 14 obtained from a stationary vehicle in a scanning mode at 20 m distance for different speeds of beams: (a) - 0.2 m/s (0.45 mph), (b) - 1 m/s (2.2 mph). Excitation at 97 Hz frequency was provided by a speaker.

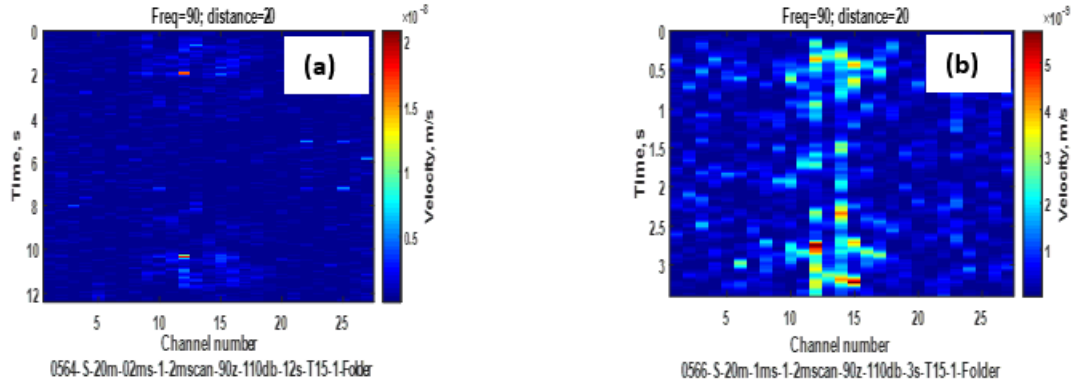

Figure 120. Vibration image of target 15 obtained from a stationary vehicle in a scanning mode at 20 m distance for different speeds of beams: (a) - 0.2 m/s (0.45 mph), (b) - 1 m/s (2.2 mph). Excitation at 90 Hz frequency was provided by a speaker.

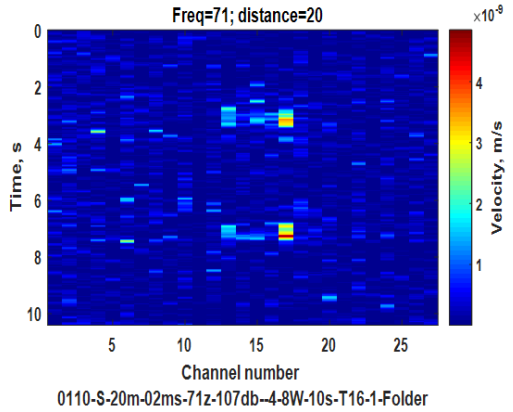

Figure 121. Vibration image of target 16 obtained from a stationary vehicle in a scanning mode at 20 m distance for speed of beams 0.2 m/s (0.45 mph). Excitation at 71 Hz frequency was provided by a speaker.

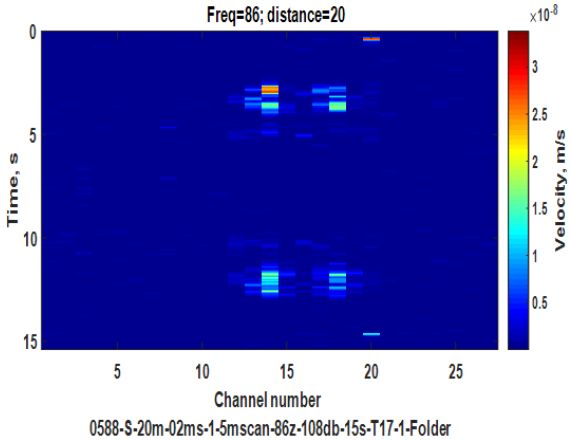

Figure 122. Vibration image of target 17 obtained from a stationary vehicle in a scanning mode at 20 m distance for different speeds of beams: (a) - 0.2 m/s (0.45 mph). Excitation at 86 Hz frequency was provided by a speaker.

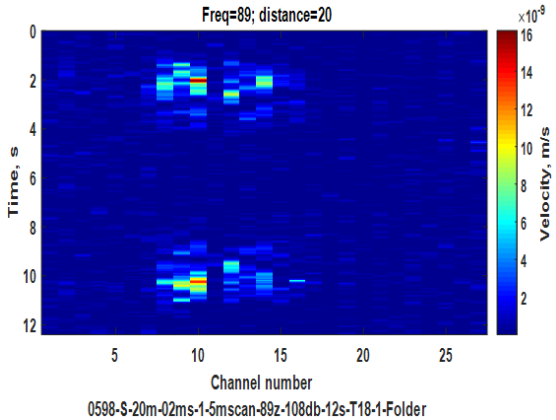

Figure 123. Vibration image of target 18 obtained from a stationary vehicle in a scanning mode at 20 m distance for different speeds of beams: (a) - 0.2 m/s (0.45 mph). Excitation at 89 Hz frequency was provided by a speaker.

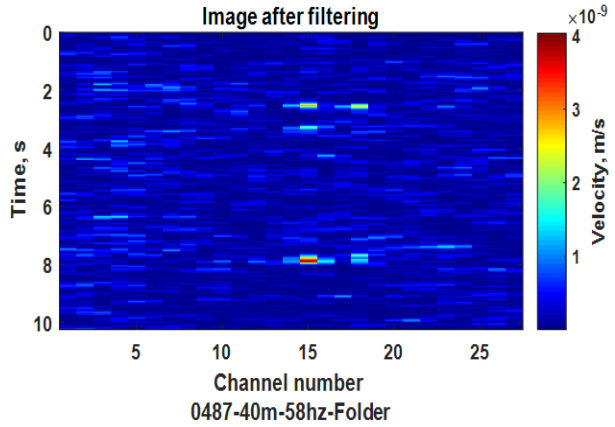

Figure 124. Vibration image of target 20 (plastic box) obtained from a stationary vehicle in a scanning mode at 40 m distance for speed of beams: (a) - 0.4 m/s (0.9 mph). Excitation at 58 Hz frequency was provided by a speaker.

Figures 125 - 131 show vibration images of detected targets from a stationary vehicle at 20 m standoff distance using the HFWS as an excitation source.
Targets 5, 6, and 7 were measured in one scan, which covers 3 meters along the track. Only two targets, 6 and 7, are seen on the vibration image shown in Figure 125.

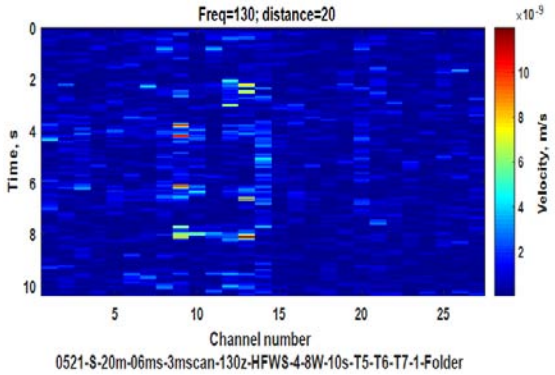

Figure 125. Vibration image of targets 5, 6, and 7 obtained from a stationary vehicle in a scanning mode at 20 m distance for speed of beams 0.6 m/s (1.3 mph). Excitation at 130 Hz frequency was provided by the HFWS.

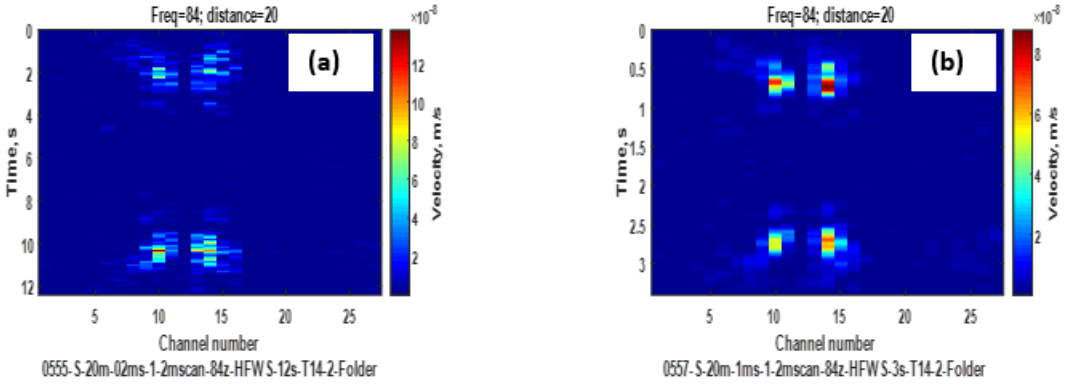

Figure 126. Vibration image of target 14 obtained from a stationary vehicle in a scanning mode at 20 m distance for different speeds of beams: (a) - 0.2 m/s (0.45 mph), (b) - 1 m/s (2.2 mph). Excitation at 84 Hz frequency was provided by the HFWS.

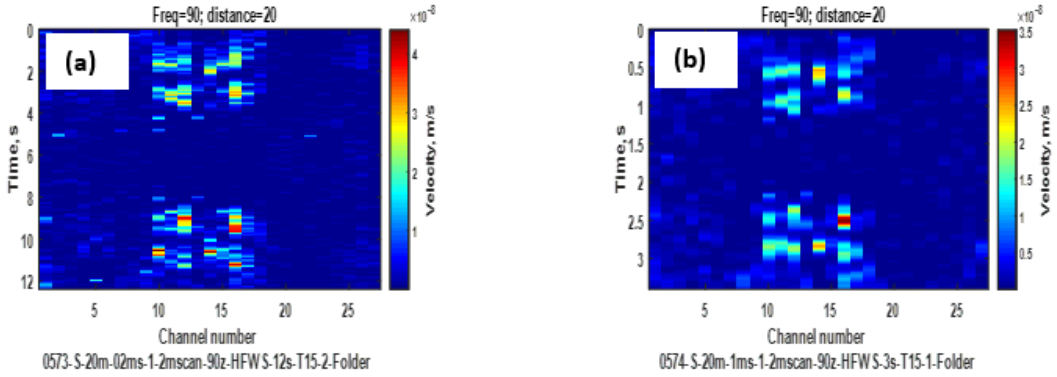

Figure 127. Vibration image of target 15 obtained from a stationary vehicle in a scanning mode at 20 m distance for different speeds of beams: (a) - 0.2 m/s (0.45 mph), (b) - 1 m/s (2.2 mph). Excitation at 90 Hz frequency was provided by the HFWS.

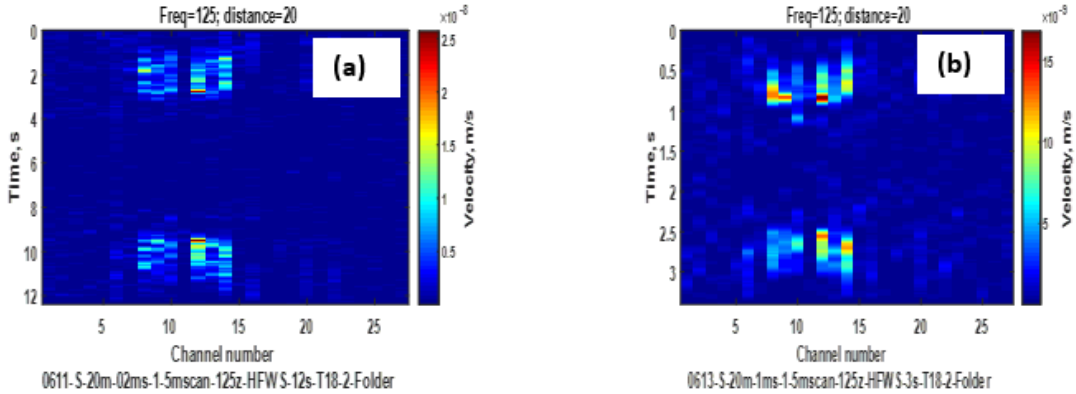

Figure 128. Vibration image of target 18 obtained from a stationary vehicle in a scanning mode at 20 m distance for different speeds of beams: (a) - 0.2 m/s (0.45 mph), (b) - 1 m/s (2.2 mph). Excitation at 125 Hz frequency was provided by the HFWS.

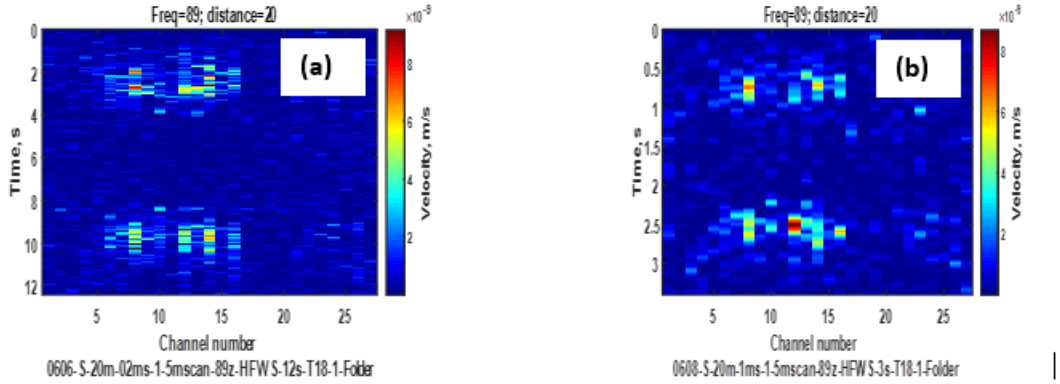

Figure 129. Vibration image of target 18 obtained from a stationary vehicle in a scanning mode at 20 m distance for different speeds of beams: (a) - 0.2 m/s (0.45 mph), (b) - 1 m/s (2.2 mph). Excitation at 89 Hz frequency was provided by the HFWS.

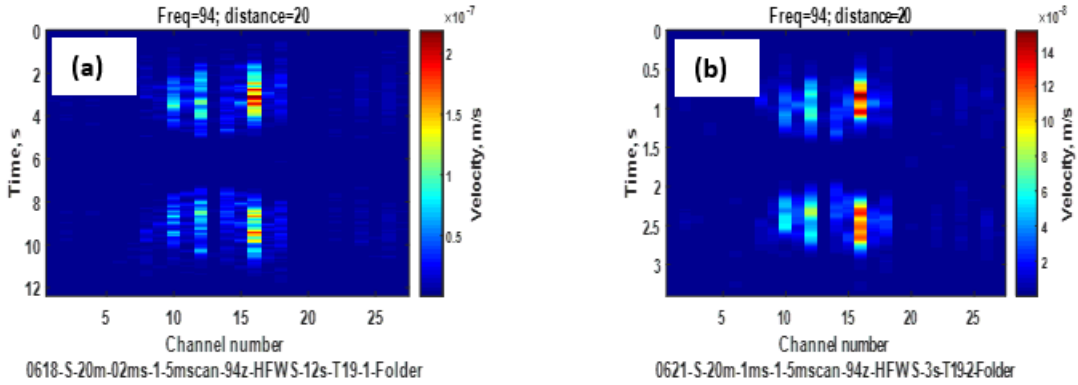

Figure 130. Vibration image of target 19 obtained from a stationary vehicle in a scanning mode at 20 m distance for different speeds of beams: (a) - 0.2 m/s (0.45 mph), (b) - 1 m/s (2.2 mph). Excitation at 94 Hz frequency was provided by the HFWS.

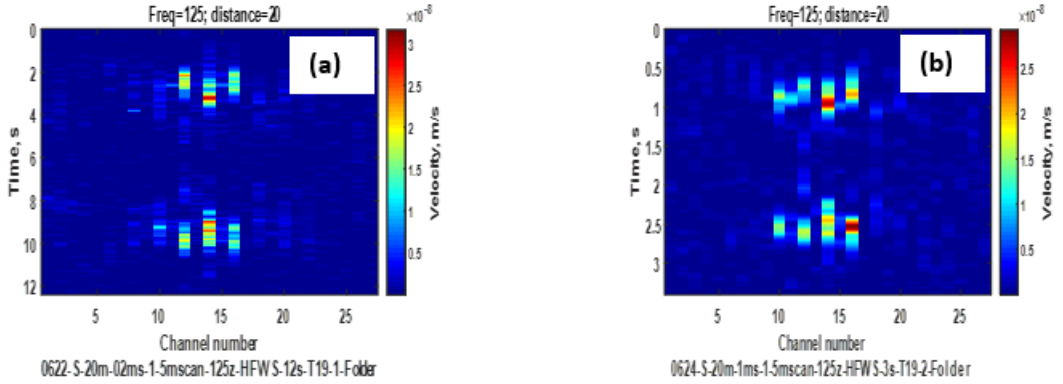

Figure 131. Vibration image of target 19 obtained from a stationary vehicle in a scanning mode at 20 m distance for different speeds of beams: (a) - 0.2 m/s (0.45 mph), (b) - 1 m/s (2.2 mph). Excitation at 125 Hz frequency was provided by the HFWS.

The summary of the detection results is shown in Table 4.

Table 4. Summary of detection results

Operation mode	Excitation source	Standoff distance	Measured targets	Detected targets
Moving vehicle	Speaker	10 m	11	11
		20 m	15	13
	HFWS	10 m	16	15
		20 m	N/A	N/A
Scanning from stationary vehicle	Speaker	10 m	19	18
		20 m	14	12
	HFWS	10 m	16	15
		20 m	7	6

13 Acoustic and mechanical shaker excitation of the ground and the surface response of buried objects.

Related studies of the vibration response of various buried objects and acoustic/seismic properties of different types of grounds using a loudspeaker and a mechanical shaker were conducted. Historically, different types of sources have been used to excite mechanical vibrations into the ground. Such sources consist of electromechanical shakers, impulsive sledgehammer sources, explosives, loudspeakers, and new, in this study, a high frequency wheel station (HFWS). Sources in direct contact with the ground (hammers and shakers) are commonly used in traditional seismic surveys and are referred to here as seismic sources. Most seismic investigations have interests in subsurface structure at meters to kilometers below the ground surface. Loudspeaker sources have been used extensively in acoustic methods for detection of objects buried within tens of centimeters of the ground surface. Both types of sources have been studied extensively by different research communities. A schematic of propagation and coupling of mechanical energy into the ground from seismic and acoustic is presented in Figure 132.

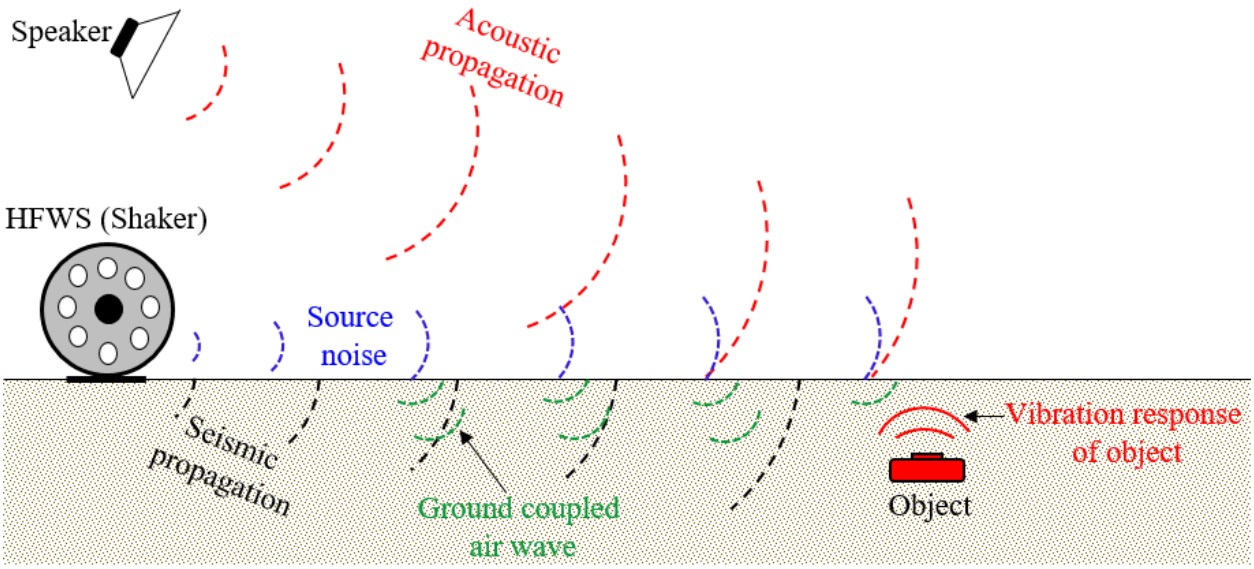

Figure 132: Schematic showing the acoustic versus mechanical excitation of the ground. In addition to mechanical excitation, the HFWS also generates acoustic excitation of the ground.

Like other active acoustic methods, the problem can be divided into: the source characteristics (source strength and coupling), propagation (geometrical spreading and attenuation), and target response.

A loudspeaker produces an airborne acoustic wave that propagates through the air. The coupling of the source to the air is easily characterized in terms of sound pressure levels (SPL). Building loudspeakers with high output can be difficult at low frequencies. The loss of signal due to acoustic propagation is relatively small at the frequencies (50-400Hz) used for buried object detection. The ground induced vibrations due to an impinging acoustic wave is referred to as the acoustic to seismic (a/s) transfer function. For outdoor ground surfaces, much of the acoustic energy can be reflected, and therefore, the efficiency of coupling acoustic energy into ground vibrations is a limiting factor in acoustic detection methods. Furthermore, the a/s transfer function depends on the mechanical properties of the ground and is therefore quite variable.

For seismic sources, the direct contact between the source and the ground surface provides for a better transfer of energy into the ground. However, this coupling is frequency dependent and many surface seismic sources work best for frequencies below 100Hz, which is somewhat lower than needed for buried object detection. For this type of excitation, the energy propagates through the ground primarily as surface seismic waves. Although the geometrical spreading of these waves are less than acoustic waves, their decay with range is usually more due to the larger attenuation of seismic waves in soils. Seismic sources also produce acoustic waves and are referred to as the airwave or blast wave. In traditional seismic applications, this is a source of unwanted noise and can be easily detected in seismic records. For buried object detection at short distances from the source, the ground deformation due to the acoustic and seismic energy cannot be easily separated.

The final component of the problem in buried object detection is the response of the object to the incident mechanical wave. It is postulated and well documented that many man-made objects have unique vibrational responses as a function of frequency. These are associated with different vibrational modes within the structure and depend on the size and construction of

the object. For many objects of interest, it is these unique structural characteristics that allow their detection using low frequency mechanical excitation.

In the following sections, results from two studies related to buried object detection are presented. Some information was obtained from ancillary data collected during the LMBDIS experiment in Eglin, FL. The majority of the results are associated with a more comprehensive study conducted in Oxford, MS.

13.1 Acoustic versus seismic excitation of the ground

Ground surface deformations associated with acoustic and contact mechanical sources were investigated. Measurements were conducted to evaluate the dependence of the ground deformation on:

1. source type, i.e. loudspeaker versus mechanical shaker,
2. soil type, i.e. limestone gravel (hard), clay gravel (medium hard), and grass field (soft),
3. component of the deformation, i.e. in-line velocity (V_x) and vertical velocity (V_z) and
4. distance from the source or range.

The ground surface deformation associated with buried objects was also investigated. Measurements of the different components of the ground surface deformation above and adjacent to buried objects were obtained for different:

1. source types, i.e. loudspeaker versus mechanical shaker,
2. types objects,
3. depths of burial (from 1" to 6")
4. distances from the source or range, and
5. soil types.

The comprehensive study was conducted at an experimental test site located in Oxford, MS. Three different ground types; a limestone gravel lane (hard soil), a clay road (medium hard soil), and a grass field site (soft soil) shown in Figure 133 were selected for testing.

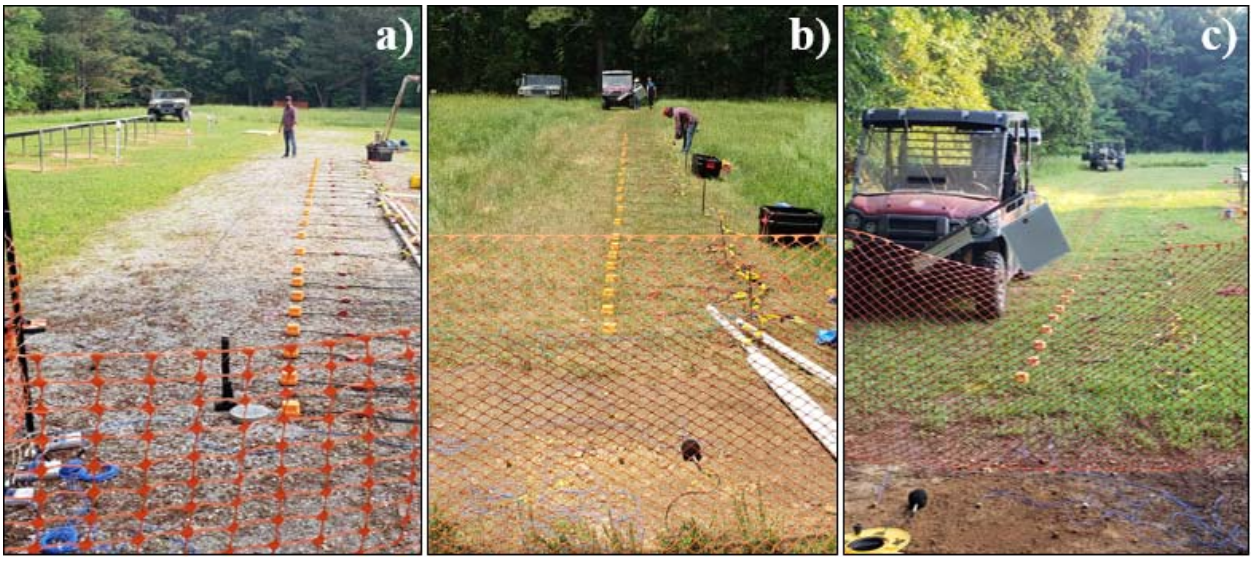

Figure 133: Oxford, MS experimental site: a) Limestone gravel lane, constructed more than 15yrs ago as a test lane, b) clay road site, has been in place for more than 25 years with minimal traffic from small trucks and cars, and c) a grass field site, undisturbed with no vehicular traffic

The sensor layout for measuring the ground surface deformation is shown in Figure 134. Twenty-four three-component geophones were used to study the wave propagation properties in the ground and to back-calculate vibration levels of the source. A group of sensors around the object were used to study how the object responds to an incoming acoustic or seismic wave. Ground surface motion on the object was measured by placing a three-component accelerometer at the center of the object and another accelerometer at a distance of 0.5m was used to measure the off object response. A half-inch B&K microphone was placed close to the target to measure the acoustic pressure.

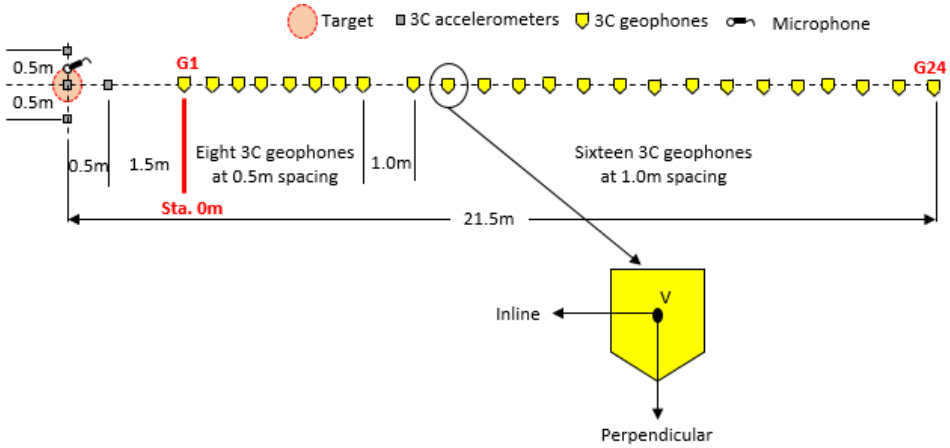

Figure 134: Sensor layout for monitoring the ground surface deformation.

The basic wave propagation attributes associated with seismic and acoustic sources are the wave propagation velocity and attenuation. The wave velocity versus frequency, or

dispersion curve, can be measured using a frequency-wavenumber transform of the geophone array data. This information represents an average over the length of the array. For this analysis the vertical component of the ground was used. The dispersion curves measured using a loudspeaker broadcasting a sweep from 50 to 250 Hz, for the three different types of grounds, is shown in Figure 135. For acoustic sources, the wave propagates via ground coupled airwave with a velocity of 343m/s and is independent of frequency. For a hard ground, such as the limestone gravel, the coupled acoustic wave dominates the energy from 50Hz to 250Hz. Below 50Hz the seismic surface wave is produced by background seismic energy. The feature at 160Hz requires future investigation but is either associated with the geophone response or some local source of seismic energy. For the clay road and grass field, the dispersion curves are more complicated. In these softer soils, it appears that the acoustically coupled energy dominates only at frequencies greater 130Hz for the clay road and 80Hz for the grass field. The ground response below these frequencies is produced by background seismic energy. The aged clay road produces the most complicated dispersion curve, most likely associated with variations in ground properties over the length of the array.

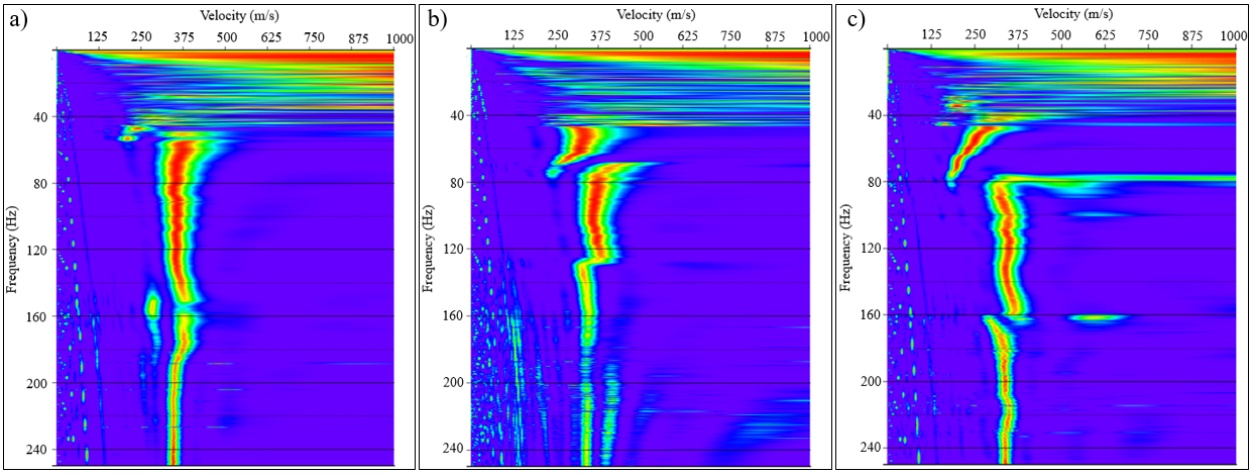

Figure 135: Airwave dispersion curves excited using a loudspeaker for: a) Limestone gravel, b) clay road, c) grass field.

The seismic surface wave velocity measured using a hammer impact source for the three different types of grounds is shown in Figure 136. The energy produced by the hammer source is constrained to frequencies below 150Hz and is significant down to 10Hz (cutoff for geophones). The phase velocity of the waves associated with this energy is almost always less than 343m/s. The dispersion curve for the limestone gravel is the most continuous curve and can be attributed to the homogeneity of the limestone gravel lane, better coupling of the hammer impact (higher S/N), and lower seismic attenuation. The soft grass field site has two predominant surface wave modes indicating some change in ground properties with depth. The first mode at frequencies between 10Hz and 30Hz (velocity~250m/s) is influenced by the deeper soil properties. The dispersion curve between 30Hz and 45 Hz is difficult to interpret. One could postulate that the acoustic energy due to the hammer impacting the metal plate dominates the energy between 35Hz and 45Hz, but that requires further investigation. Above 45Hz to a maximum of 150Hz, the velocity is decreasing with increasing frequency indicating that the soil velocity is decreasing uniformly as it approaches the ground surface. Similar to the loudspeaker source results, the aged clay road produces the most complicated dispersion curve and the energy

is contained in frequencies below 80Hz. The reduced frequency range could be attributed to the hammer source coupling. The dispersion curve at low frequency (less than 25Hz) is much like the grass field. From 30Hz to about 50Hz the velocity increases with frequency, indicating a more compacted subsurface layer at an intermediate depth. In the higher frequency range (greater than 50Hz), the dispersion curve indicates the ground velocity decreases as the depth decreases.

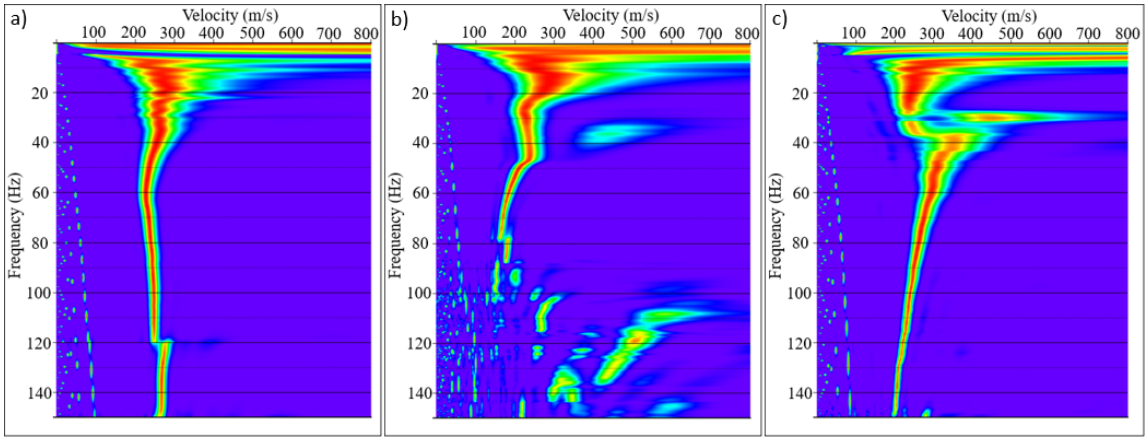

Figure 136: Seismic surface wave dispersion curves calculated using data from a hammer impact source for: a) Limestone gravel, b) clay road, c) grass field.

Dispersion curves calculated during an experiment at Eglin, FL are displayed in Figure 137. An impact from a hammer source at 2m offset produces a single seismic surface wave with a frequency band of 10Hz to 100Hz. The seismic surface velocity in the unconsolidated sand at Eglin is about 120m/s, which is lower than in the ground types investigated in Oxford, MS. The dispersion curve using the loudspeaker located at a 2m offset indicates that much of the energy is propagating at about 343m/s. However, the dispersion curve is not continuous and it is postulated that this could be due to propagation effects associated with temperature gradients near the ground surface. Other causes might be interference from either reflections from nearby objects or other background acoustic sources. In Figure 137c, the dispersion curve is calculated using the background noise. The data from 160Hz-240Hz suggest an acoustic source in-line with the array. This is most likely the gasoline generator used for onsite power. The energy between 120Hz and 160Hz may be associated with a bandlimited seismic source where the waves are impinging on the array at some angle, resulting in a larger apparent velocity. The energy at the low frequency from 45 to 120Hz could be associated with an unidentified seismic source but located closer to inline of the array.

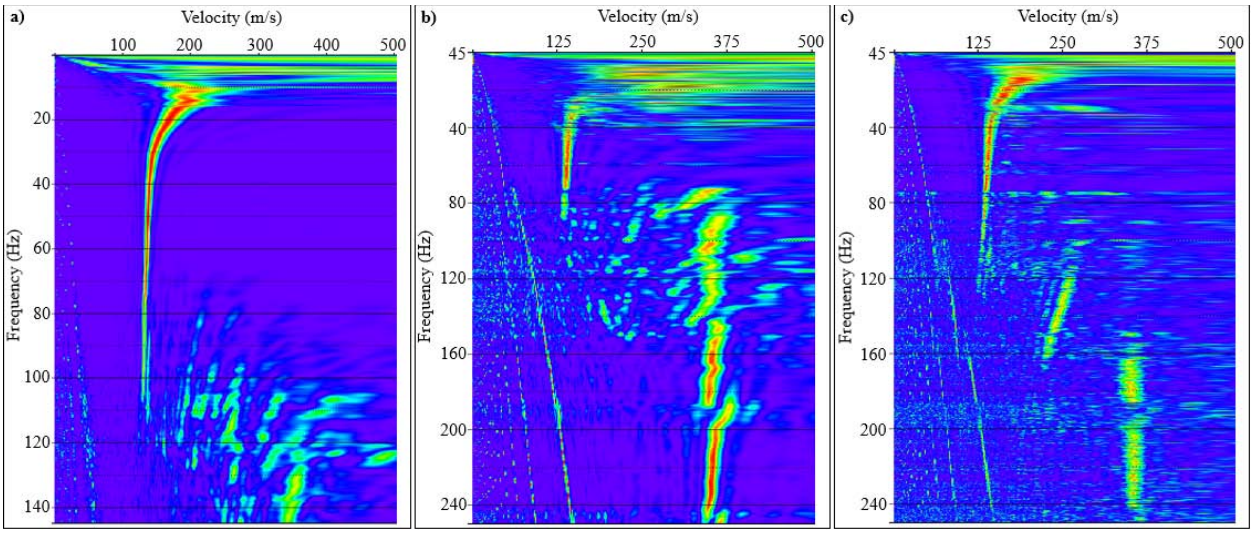

Figure 137: dispersion curves calculated for a) hammer source, b) loudspeaker source and c) using background noise.

The data presented in Figure 136 and Figure 137 clearly illustrate that the propagation of energy away from a loudspeaker source or mechanical source are significantly different and dependent on the local ground conditions.

The magnitude of induced ground motion is dependent on the coupling between the source and ground surface. The coupling of the mechanical source (and the variation in coupling) has not been studied in this effort. The coupling of acoustic energy into seismic energy or the acoustic to seismic transfer function was measured. The acoustic to seismic transfer function for the three ground types in Oxford, MS and Eglin, FL is shown in Figure 138. The acoustic to seismic transfer function is the ratio of the ground vibrations (measured using an accelerometer) to acoustic pressure (measured using a microphone) induced by a loudspeaker at a distance of 2m. The measured acceleration is converted to velocity by dividing by the angular frequency. The transfer functions have more variation in the low frequency range. The hard limestone gravel lane (hard soil) and the Eglin site (loose sand) have the smallest transfer function at low frequency (less than 70Hz). Clearly, the transfer function at low frequency is not solely dependent on the average mechanical properties. The clay road has similar values to the field grass site at low frequency. At higher frequency the behavior becomes more intuitive. Vibrating harder grounds require higher acoustic pressures than softer soils. The deviation from this general idea is that grass may be influencing the measurement above 130Hz. The a/s transfer functions are more constant at the high frequency for the roads, suggesting more uniformity due to construction.

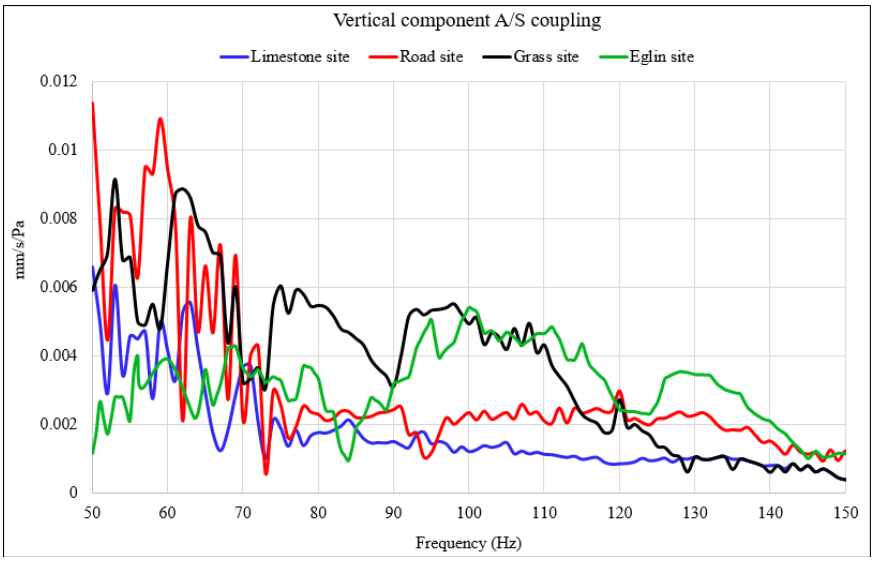

Figure 138: Acoustic to seismic transfer functions.

13.2 Buried object response to acoustic and seismic excitation

The vibration signatures of various objects were compiled and additional objects were measured. For the measurements, objects were placed on a rigid surface (asphalt drive) and excited using a loudspeaker source sweeping from 20-150Hz. The speaker has a fairly flat response over this range of frequencies. The induced vibrations (vertical velocity component) were measured using a single point LDV (PDV 100) at different locations on the surface. The frequency of the largest vibrational amplitude (within this frequency band) is documented in Table 5. Most large objects of interest, such as IED and antitank mines, should have optimum frequencies in the range of 70Hz-250Hz.

Table 5: Resonant frequency of the vibrational response of various objects

Object Name	Resonant Frequency (Hz)	Description (surrogate)	Source
TS-50	520	AP Plastic	literature
VS-50	330	AP Plastic	literature
PONZ-2	380	AP Plastic	literature
VS-1.6	220	AT Plastic	literature
TMA-5	190	AT Plastic	literature
SH-55	280	AT Plastic	literature
VS-HCT-2	465	AT Plastic	literature
VS-2.2	100	AT Plastic	Measured (20-150Hz)
TM-46	250	AT Metal	literature
TM-46	82	AT Metal	Measured (20-150Hz)
TMA-4	250	AT Metal	literature
AT-72	200	AT Wood	literature
5-gallon fuel jug (empty)	100	IED	Measured (20-150Hz)
5-gallon fuel jug (dry granular fill)	105	IED	Measured (20-150Hz)
5-gallon fuel jug (granular and liquid fill)	140	IED	Measured (20-150Hz)
105mm shell	70	IED	Measured (20-150Hz)
5.56mm steel ammo box (top)	100	IED	Measured (20-150Hz)
5.56mm steel ammo box (side)	90	IED	Measured (20-150Hz)
7.62mm steel ammo box (top)	75	IED	Measured (20-150Hz)
7.62mm steel ammo box (side)	75	IED	Measured (20-150Hz)

The modal responses of objects are altered when buried in the ground. The soil type, depth of burial, weather conditions, and how long an object has been buried are all factors that can influence the frequency response. Current detection criteria depended on the difference in vibration levels of the ground surface over buried objects.

At Eglin, FL, the frequency response of buried objects was measured using a four channel dynamic signal analyzer (Agilent 35670A) and two uncased geophones. One geophone was positioned on the ground surface above the buried object, and the other was placed on the ground surface either 0.5m or 1m (depending on target size) from the center of the object. Object excitation was provided by a loudspeaker located at 2m from the center of the object. The source signal was a swept sine (20-150Hz). The on and off object response was also measured using the HFWS at the optimum frequency determined from the loudspeaker measurement. The HFWS was located at a distance of 10m from the object location. In some cases, the frequency was restricted by the upper limit of the HFWS. The resonant frequency and on to off object response of buried objects at the Eglin test site is presented in Table 6. Most resonant frequencies are in the range of 50Hz to 250Hz. IED simulants are lower frequency than mine simulants. This should be expected since they have larger physical dimensions. The on-off velocity ratios are much larger when using the speaker source than the HFWS.

Table 6: Ground surface vibrations for various buried objects at Eglin, FL.

			Vertical velocity on/off ratio	
Object	Name (depth in inches)	Resonant freq. (Hz)	Speaker at 2m offset	HFWS at 10m offset
1	M19 (0)	115	13	1
2	M19 (2)	118	17	3
3	M19 (4)	110	11	201
4	TM46 (0)	167	196	5
5	TM46 (2)	115	33	22
6	TM46 (4)	110	8	1
7	TM46 (6)	113	16	1
8	VS1.6 (0)	151	21	1
9	VS1.6 (2)	104	7	2
10	VS1.6 (4)	118	8	2
11	VS1.6 (6)	112	7	7
12	Jug (2)	62	39	3
13	Jug (4)	71	29	7
14	Jug (6)	80	19	5
15	Jug (8)	84	45	2
16	Can (2)	72	312	5
17	Can (4)	78	91	5
18	Can (6)	83	94	13
19	Can (8)	87	23	5
20	Plastic box (1)	52	436	5

The frequency response of a suite objects buried at different depths and with different soil types at the Oxford, MS location are presented in Table 7. The excitation source is a loudspeaker. A 5-gallon gasoline jug has optimum frequency responses over a range of 50-100Hz associated with ground type or depth. This is a significant range that could be problematic with a single frequency source. The VS2.2 simulants have higher optimum frequencies within the range of 108-160Hz depending on ground type and depth. Again, this could be problematic when using a single frequency source. The limestone gravel lane consistently shows higher contrast ratios as well as larger variations than the other soils. This is because the off object velocity is significantly lower than for the other ground types. The majority of objects exhibit a reduction in on-off contrast ratio with burial depth. In general, the contrast ratios are greater than 10 for objects buried less than 2 inches and greater than 5 for depths of six inches..

Table 7: Optimum frequency and relative ground surface vibration levels for various objects when excited using a loudspeaker

Speaker source at 2m offset		Resonant frequency (Hz) / vertical on/off ratio		
Object	Location (Oxford, MS)	Object depth		
		1"	2"	6"
Empty Jug	Limestone	100/219	55/21	107/96
	Clay road	64/117	77/100	150/5
	Grass	80/26	55/843	85/9
Jug + Kitty litter (KL)	Limestone	55/123	95/51	87/61
	Clay road	50/58	100/32	108/2
	Grass	80/26	66/37	86/3
Jug + KL + Vegetable oil (VO)	Limestone	56/141	56/250	95/52
	Clay road	77/47	77/260	124/18
	Grass	55/38	55/154	85/6
TM-46	Limestone	130/938	138/455	150/80
	Clay road	130/74	120/48	110/6
	Grass	113/13	124/10	78/10
VS2.2	Limestone	160/31	125/586	160/69
	Clay road	160/21	133/29	135/3
	Grass	116/28	108/14	113/4
5.56mm Steel box (empty)	Limestone	103/162	107/183	123/56
	Clay road	124/90	145/34	140/3
	Grass	100/56	100/24	104/6
7.62mm steel box (empty)	Limestone	73/117	120/286	116/24
	Clay road	115/108	125/26	135/3
	Grass	107/74	124/17	130/5
7.62mm wood crate (empty)	Limestone	76/195	76/93	100/38
	Clay road	98/249	115/84	121/6
	Grass	78/106	77/45	80/8

The response of a suite objects buried at different depths and with different soil types at the Oxford, MS, location excited using the HFWS are presented in Table 8. The magnitudes of the on-off velocity are significantly lower when compared to the loudspeaker excitation. The difference between sources is less at the deeper six-inch depth. The very large contrast ratios seen for the limestone lane using the loudspeaker are not observed with the HFWS. This is because the off object velocity is produced by the seismic wave and not a function of the a/s transfer function.

Table 8: Relative ground surface vibration levels for various objects when excited using the HFWS at a preselected frequency.

HFWS source at 10m offset		Resonant frequency (Hz) / vertical on/off ratio		
Object	Location (Oxford, MS)	Object depth		
		1"	2"	6"
Empty Jug	Limestone	100/15	55/3	107/12
	Clay road	64/6	77/5	150/2
	Grass	80/9	55/10	85/5
Jug + Kitty litter (KL)	Limestone	55/17	95/5	87/16
	Clay road	50/8	100/6	108/4
	Grass	80/7	66/3	86/4
Jug + KL + Vegetable oil (VO)	Limestone	56/25	56/19	95/8
	Clay road	77/6	77/8	124/11
	Grass	55/11	55/13	85/4
TM-46	Limestone	130/26	138/15	150/8
	Clay road	130/8	120/9	110/3
	Grass	113/6	124/4	78/118
VS2.2	Limestone	160/5	125/34	160/5
	Clay road	160/4	133/6	135/2
	Grass	116/11	108/16	113/3
5.56mm Steel box (empty)	Limestone	103/20	107/23	123/4
	Clay road	124/23	145/5	140/5
	Grass	100/12	100/11	104/4
7.62mm steel box (empty)	Limestone	73/6	120/5	116/4
	Clay road	115/8	125/16	135/2
	Grass	107/21	124/8	130/2
7.62mm wood crate (empty)	Limestone	76/11	76/17	100/10
	Clay road	98/14	115/7	121/3
	Grass	78/11	77/10	80/2

13.3 Acoustic and seismic excitation versus range

Changes in ground surface vibration velocity as a function of range from the source were investigated. Both the loudspeaker and HFWS were located at 10m, 20m, 25m 28m, and 40m from the buried object. The amplitude of the ground surface vibration velocity was measured using the array of geophones (small circular symbols). The on and off surface velocity was measured using accelerometers and converted to velocity. The acoustic pressure was measured using a microphone (see Figure 134 for more details).

A photograph of a VS2.2 mine surrogate being buried at 1” in the limestone gravel lane (hard soil) is shown in Figure 139.

Figure 139: VS2.2 mine surrogate being buried at 1".

The vertical velocity versus range for a VS2.2 buried at 1" in the limestone gravel lane is shown in Figure 140. The data is for a frequency of 160Hz. The background seismic levels are shown by the small black dashes. The seismic background velocity is on the order of 10^{-6} mm/s, and slightly higher for the HFWS ($5x10^{-6}$mm/s) because the hydraulic pump was running during background noise measurements for the HFWS. The HFWS produces larger ground vibrations (0.5mm/s) than the loudspeaker (10^{-1} mm/s). The actual magnitudes are not a representation of maximum capability because the loudspeaker was not at its maximum output. The vibration levels of the HFWS decay fast with range due the attenuation of the seismic surface wave in the ground. The decay with range (slope) becomes less for distances beyond about 25m. At this range it is postulated that the acoustic noise produced by the HFWS is responsible for the ground excitation. In other words, the HFWS is acting as a speaker. The ground vibration levels are still an order of magnitude larger than the loudspeaker but, as shown in the table on the right, the HFWS is producing 10dB more SPL than the loudspeaker.

The response of the VS2.2 simulants is labeled using the large symbols and documented in the tables on the right. The contrast ratio is much larger using the loudspeaker at all ranges. The contrast ratios with the HFWS are still significant except at 23m offset. It is postulated that this may be interference of the response from the acoustic wave and the seismic wave. This requires further investigation.

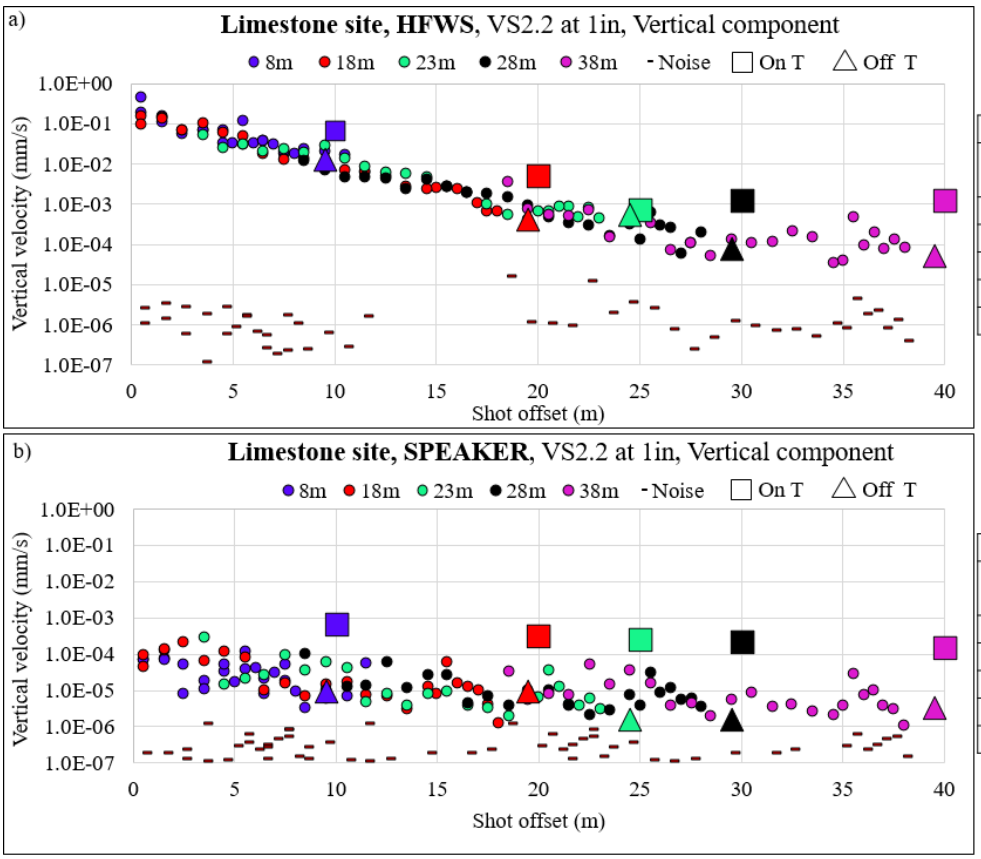

Res. Frequency	160 Hz
Shot loc.	SPL (dB)	On/off Ratio
8m	138	5
18m	129	12
23m	128	1
28m	125	16
38m	125	23

Res. Frequency	160 Hz
Shot loc.	SPL (dB)	On/off Ratio
8m	118	75
18m	111	33
23m	109	158
28m	108	137
38m	105	42

Figure 140: Vertical component of the ground surface velocity versus range for VS2.2 simulant buried at 1" in the limestone gravel lane, a) HFWS source b) Speaker source.

A representative IED type surrogate, which has low frequency responses, is a 5-gallon plastic jug filled with kitty litter and vegetable oil (Jug+KL+VO). A photograph of this surrogate being buried at 1” in the grass field (soft soil) is shown in

Figure 141. The following data presented in Figure 142 is for the limestone gravel lane (hard soil).

Figure 141: IED type object being buried in grass field soil.

Except for the shot location at 38m offset, the HFWS stimulates a good on-off ratio ranging from 5 to 25. Compared to the VS2.2 buried in the same depth and soil type, the jug+KL+VO has a better on-off ratio at near offset for the HFWS. For the speaker source, except for shot location 8m with an on/off ratio of 141, the on/off ratio for the jug+KL+VO ranges from 10 to 63. Speaker source for the mine surrogate gives an overall better on-off ratio compared to the IED type surrogates.

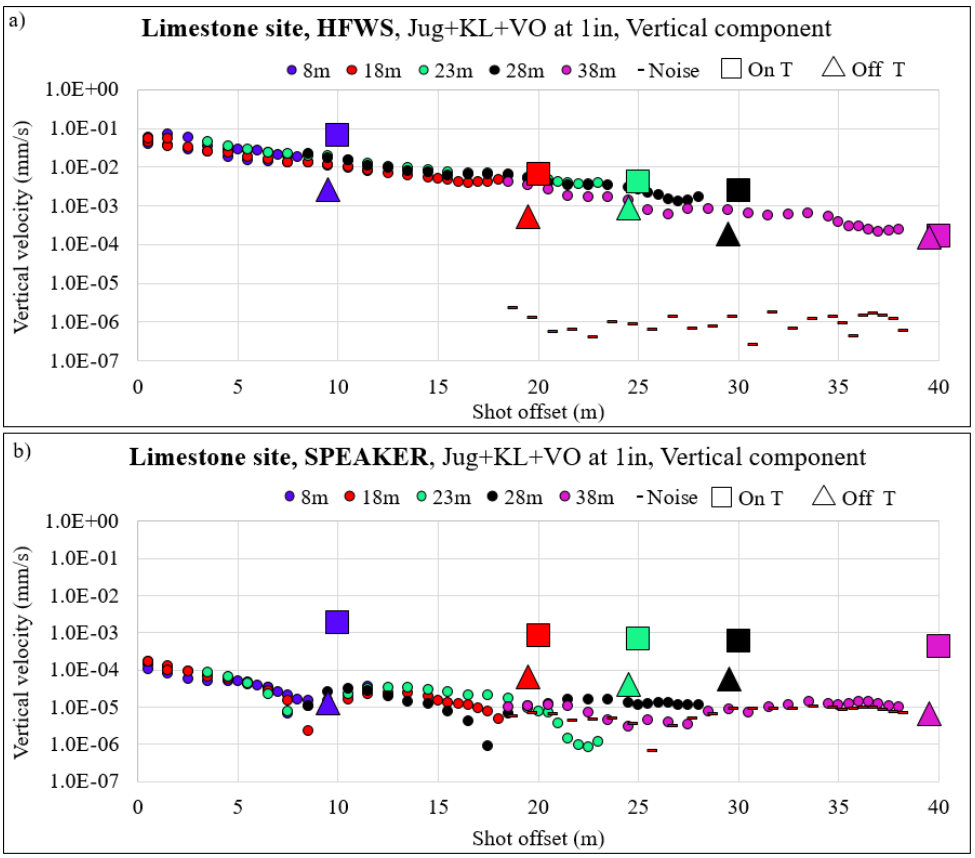

Res. Frequency		56 Hz
Shot loc.	SPL (dB)	On/off Ratio
8m	119	25
18m	111	12
23m	104	5
28m	103	13
38m	103	1

Res. Frequency		56 Hz
Shot loc.	SPL (dB)	On/off Ratio
8m	113	141
18m	104	13
23m	102	18
28m	99	10
38m	104	63

Figure 142: Vertical component of the ground surface velocity versus range for for Jug+KL+VO IED simulant buried at 1" in the limestone gravel lane, a) HFWS source b) Speaker source.

13.4 Dependence on soil type

The dependence on ground type was studied by burying various objects in three different grounds. The follow example is for a VS2.2 buried at a depth of 1". For the grass field (Figure 143a), the on-off ratio for the HFWS ranges from 3 to 13. This range is not significantly different from the same surrogate buried in the limestone lane with an on-off ratio ranging from 5 to 23 (Figure 140). For the speaker source, the on-off ratio ranges from 12 to 15 for the grass field (Figure 143b). This range is significantly lower than for the limestone lane (33 to 158). The overall vertical vibration levels are slightly higher in the grass site (soft soil) for both the HFWS and speaker source. For each shot location, there is less variability in the vertical velocity of the geophones for the grass field compared to the limestone lane. This could be an artifact of geophone coupling.

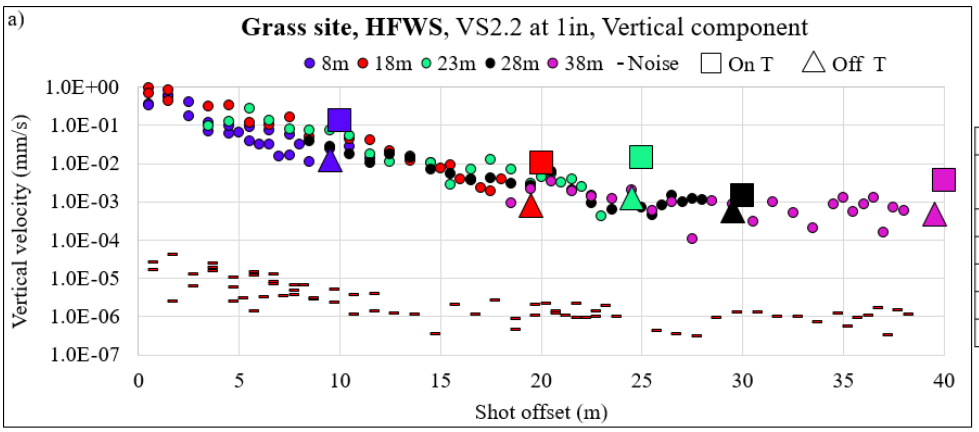

Res. Frequency		116 Hz
Shot loc.	SPL (dB)	On/off Ratio
8m	130	11
18m	124	13
23m	122	11
28m	120	3
38m	119	8

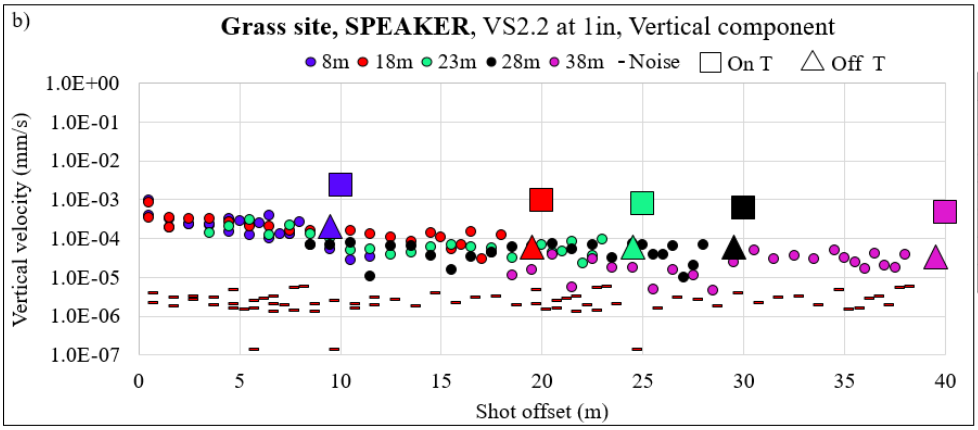

Res. Frequency		116 Hz
Shot loc.	SPL (dB)	On/off Ratio
8m	115	12
18m	110	15
23m	107	13
28m	106	10
38m	103	14

Figure 143: Vertical velocity versus range for VS2.2 buried at 1" depth in the grass field (soft soil), a) HFWS source b) Speaker source.

For the clay road (Figure 144a), the on-off velocity ratio using the HFWS, ranges from 4 to 13. This range is not significantly different from limestone lane (hard soil) or grass field (soft soil). For the speaker source, the clay road (Figure 144b), produces on-off ratio in the range of 12 to 79. This range is significantly lower compared to the limestone lane (33 to 158) and slightly better than grass field (12 to 15). The overall vertical vibration levels are slightly higher on the clay road site (medium hard soil) for both the HFWS and speaker source.

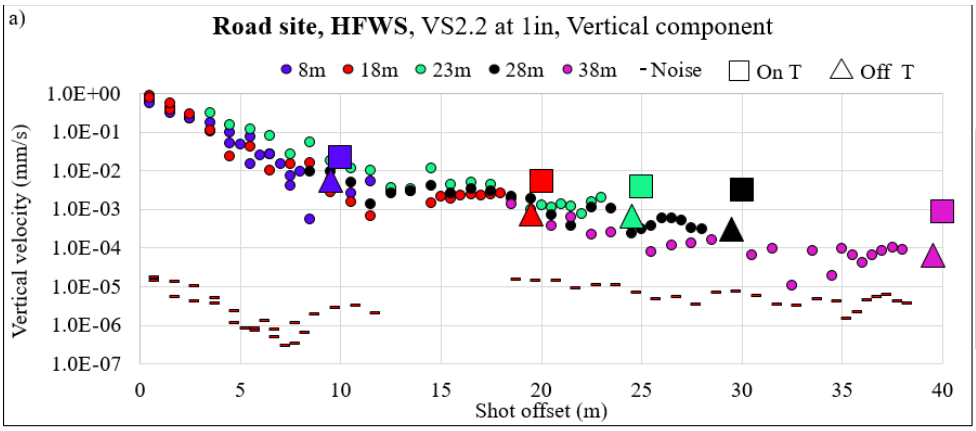

Res. Frequency		160 Hz
Shot loc.	SPL (dB)	On/off Ratio
8m	132	4
18m	128	7
23m	124	6
28m	123	10
38m	121	13

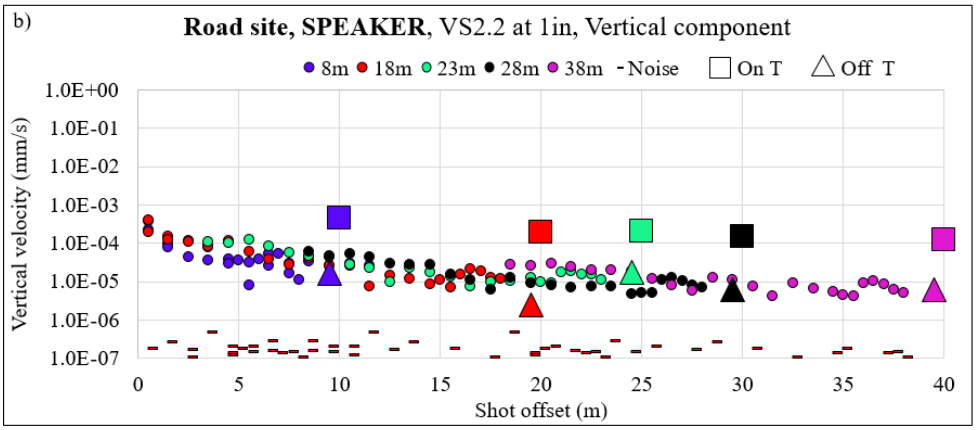

Res. Frequency		160 Hz
Shot loc.	SPL (dB)	On/off Ratio
8m	115	26
18m	109	79
23m	108	12
28m	106	24
38m	105	20

Figure 144: Vertical velocity versus range for VS2.2 buried at 1" depth in the clay road (medium hard soil), a) HFWS source b) Speaker source.

13.5 Inline vibration (V_x) response of buried objects

The inline vibration results for a VS2.2 are shown in Figure 145. The inline velocity levels are well above the background levels for both the HFWS and speaker source. The inline velocity levels are larger than the velocity normal to the ground surface for both the HFWS and speaker. This was an unexpected result. Although the inline velocity (Vx) levels are larger, the on-off ratio for both the HFWS and speaker source are low regardless of range.

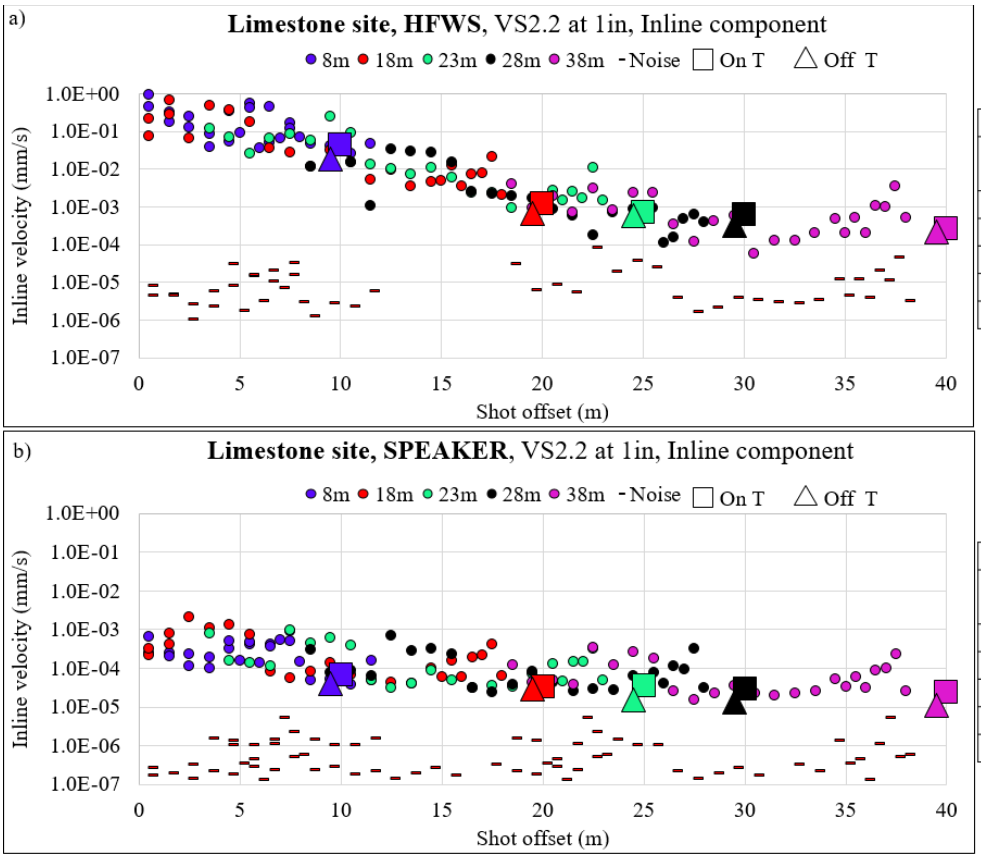

Res. Frequency	160 Hz
Shot loc.	SPL (dB)	On/off Ratio
8m	138	2
18m	129	2
23m	128	1
28m	125	2
38m	125	1

Res. Frequency	160 Hz
Shot loc.	SPL (dB)	On/off Ratio
8m	118	2
18m	111	1
23m	109	2
28m	108	2
38m	105	2

Figure 145: Inline velocity versus range for a VS2.2 buried at 1" in the limestone lane, a) HFWS source b) Speaker source.

14 Conclusions

The Laser Multi-Beam Differential Interferometric Sensor (LMBDIS) provides measurement of vibration fields of objects with interferometric sensitivity, while having low sensitivity to the motion of the sensor itself. The LMBDIS is capable of vibration imaging of ground for acoustic detection of buried objects from a moving vehicle with laser beams looking forward.

The LMBDIS integrated on the electric vehicle allows vibration imaging of the ground in two modes of operation: scanning mode, when laser beams sweep the ground from a stationary vehicle by using a scanning mirror; and in a moving mode, when the laser beams scan the ground due to the vehicle motion.

Performance of the LMBDIS integrated on the electric vehicle in a scanning and a moving modes has been investigated under laboratory conditions.

Field experiments on acoustic detection of buried objects using the LMBDIS mounted on the electric vehicle have been completed at a military test site. The measurements were conducted for 10 m and 20 m distance in both the moving and the scanning modes. A loudspeaker and the wheeled shaker have been used for ground vibration excitation. Buried objects have been measured in the moving mode at speeds of vehicle ranging from 0.4 m/s (0.9 mph) to 4.5 m/s (10 mph) and in the scanning mode at speeds of beams ranging from 0.2 m/s

(0.45 mph) to 2 m/s (4.4 mph). Detection of a buried object at standoff distance 40 m has been demonstrated in the scanning mode.

The experiments demonstrated detection of a buried object from a moving vehicle at a speed of up to 4.5 m/s (10 mph) for 10 m distance and 2.14 m/s (4.8 mph) for 20 m distance.

Acoustic and contact mechanical sources cause different deformations of the ground surface. However, both types of sources produce vibrations that are both in-plane and normal to the ground surface. The propagation of the seismic surface wave (phase velocity and attenuation) depend on the type of ground. The propagation of the acoustic wave generated by the loudspeaker does not depend on ground type. However, the coupling of acoustic energy into ground surface vibrations, the acoustic to seismic transfer function, is dependent on soil type. Both types of sources produce significant in-plane deformation. This was somewhat unexpected and requires further research. For the ground types investigated in this study, both sources produce vibrations levels above the LMBDIS noise floor at ranges beyond 20m.

The ground surface deformation relative to adjacent grounds associated with buried objects indicates that the loudspeaker produces a better contrast than the HFWS. However, in many cases either source would produce sufficient contrast for detection. Hard grounds produce larger on/off contrasts due to the lower off object values. No clear dependence on depth was observed. It appears that variability associated with the burial process may be too large to determine this dependence. The contrast in the in-plane deformation is very small which could be problematic when measuring at grazing incidence.

15 References

1. J.M. Sabatier and N. Xiang, "An Investigation of Acoustic-to-Seismic Coupling to Detect Buried Antitank Landmines", *IEEE Transactions on Geoscience and Remote Sensing*, 39(6), 1146-1154 (2001).
2. N. Xiang and J.M. Sabatier, "An Experimental Study on Antipersonnel Landmine Detection using Acoustic-to-Seismic Coupling", *J. Acoust. Soc. Am*., 113(3), 1333-1341 (2003).
3. N. Xiang and J.M. Sabatier, "Laser Doppler Vibrometer-Based Acoustic Landmine Detection Using the Fast M-Sequence Transform", *IEEE Geoscience and Remote Sensing Letters*, 1, 292-294 (2004).
4. V. Aranchuk, A.Lal, C. Hess, and J.M. Sabatier, "Multi-beam laser Doppler vibrometer for landmine detection", *Optical Engine*ering, 45 (10), 104302 (2006)
5. Amit Lal, Slava Aranchuk, Valentina Doushkina, Ernesto Hurtado, Cecil Hess, Jim Kilpatrick, Drew L'Esperance, Nan Luo, Vladimir Markov, Jim Sabatier, Eddie Scott, "Advanced LDV instruments for buried landmine detection", *Proc. SPIE*, 6217, 621715 (2006).
6. Vyacheslav Aranchuk, Amit K. Lal, Hansheng Zhang, Cecil F. Hess, and James M. Sabatier, "Acoustic Sensor for Landmine Detection using a Continuously Scanning Multi-Beam LDV," *Proc. SPIE*, 5415, 61-69 (2004).
7. Vyacheslav Aranchuk, James M. Sabatier, Amit K. Lal, Cecil F. Hess, Richard. D. Burgett , and Michael O'Neill, "Multi-beam laser Doppler vibrometry for acoustic landmine detection using airborne and mechanically-coupled vibration," *Proc. SPIE*, 5794, 624-631 (2005)

8. James M. Sabatier, Richard Burgett, Vyacheslav Aranchuk ”High Frequency A/S Coupling for AP Buried Landmine Detection using Laser Doppler Vibrometers”. *Proc. SPIE*, 5415, 35-41, (2004).
9. A.K.Lal, H.Zhang, V. Aranchuk, E. Hurtado, C. F. Hess, R. D. Burgett, J. M. Sabatier. ”Multiple-beam LDV system for buried landmine detection”. *Proc. SPIE*, 5089, 579-590, (2003).
10. Amit K. Lal, Cecil F Hess, Hansheng Zhang, Ernesto Hurtado, Vyacheslav Aranchuk, Vladimir B. Markov, and William T. Mayo.”Whole-field laser vibrometer for buried landmine detection”. *Proc. SPIE*, 4742, 640-648, (2002).
11. J.M. Sabatier and V. Aranchuk, “Multiple Beam laser Doppler Vibrometry for landmine detection,” *Proc. 14th Coherent Laser Radar Conference*, Snowmass, Colorado, July 8-13, (2007).
12. E. M. Rosen, K. D. Sherbondy, and J. M. Sabatier, “Performance assessment of a blind test using the University of Mississippi’s Acoustic/Seismic laser Doppler Vibrometer (LDV) mine detection apparatus at A. P. Hill”, *Proc. SPIE*, 4037, p. 656-666, (2000).
13. James M. Sabatier, Vyacheslav Aranchuk, W. C. Kirkpatrick Alberts II, “Rapid high-spatial-resolution imaging of buried landmines using ESPI,” *Proc. SPIE*, 5415, 14-20 (2004)
14. Cary L. Cloud, *Optical methods of engineering analysis*, Cambridge University press, (1995).
15. James Sabatier, Vyacheslav Aranchuk " Digital shearography as a ground vibration sensor" , Proc. of the Military Sensing Symposium on Battlespace Acoustic and Seismic Sensing, Magnetic and Electric Field Sensors, (2009).
16. L. Yang, W. Steichen, G. Kupfer, P. Mackel, F. Vossing, Vibration analysis by means of digital shearography, *Optics and Lasers in Engineering*, 30, 199-212. (1998).
17. Wolfgang Steinchen, Lianxiang Yang, *Digital Shearography*, SPIE Press, (2003).
18. Vyacheslav Aranchuk, Amit K. Lal, Cecil F. Hess, James Davis Trolinger, Eddie Scott, "Pulsed spatial phase-shifting digital shearography based on a micropolarizer camera," *Opt. Eng.* **57**(2), 024109 (2018).
19. Vyacheslav Aranchuk, "Laser Multi-Beam Differential Interferometric Sensor", final report on grant number ONR N00014-13-1-0868, December (2014).
20. Vyacheslav Aranchuk, Craig Hickey, "Field Testing of Brassboard Laser Multi-Beam Differential Interferometric Sensor", final report on grant number ONR N00014-15-1-2660, December (2017).
21. V. Aranchuk, I. Aranchuk, B. Carpenter, C. Hickey, D. Kleinert, H. Buchanan, and J.D. Heffington, "Laser multi beam differential interferometric sensor for acoustic detection of buried objects", *Proc. SPIE*, 10628, detection and Sensing of Mines, Explosive Objects, and Obscured targets XXIII, 1062804 (2018).
22. Warren J. Smith, *Modern Optical Engineering*, McGraw Hill, (2008).
23. L. Cohen, *Time Frequency Analysis*, Prentice-Hall, (1995).
24. Julius S. Bendat and Allan G. Piersol, *Engineering Applications of Correlation and Spectral Analysis*, John Wiley & Sons, (1980).